The Effects of Implanted Hydrogen and Helium on Cavity Formation in Self-Ion Irrdiated Nickel

Daniel Bernard Bullen

May 1984

UWFDM-563

Ph.D. thesis.

FUSION TECHNOLOGY INSTITUTE

UNIVERSITY OF WISCONSIN

MADISON WISCONSIN

The Effects of Implanted Hydrogen and Helium on Cavity Formation in Self-Ion Irrdiated Nickel

Daniel Bernard Bullen

Fusion Technology Institute
University of Wisconsin
1500 Engineering Drive
Madison, WI 53706

http://fti.neep.wisc.edu

May 1984

UWFDM-563

Ph.D. thesis.

THE EFFECTS OF IMPLANTED HYDROGEN AND HELIUM ON CAVITY FORMATION IN SELF-ION IRRADIATED NICKEL

BY

DANIEL BERNARD BULLEN

A thesis submitted in partial fulfillment
of the requirements for the degree of

DOCTOR OF PHILOSOPHY
(Nuclear Engineering)

at the

UNIVERSITY OF WISCONSIN-MADISON

1984

THE EFFECTS OF IMPLANTED HYDROGEN AND HELIUM ON CAVITY FORMATION IN SELF-ION IRRADIATED NICKEL

Daniel Bernard Bullen

Under the supervision of Professor Gerald L. Kulcinski

Interstitial gas atoms, such as hydrogen and helium, introduced into the lattice of a metal in a fusion reactor environment via (n,p) and (n,α) reactions or by permeation and diffusion, can act as nucleation sites for cavity formation. Electrostatic accelerators are used to simulate fusion neutron displacement damage and interstitial gas atom effects in preinjection and co-implantation irradiation studies. In this investigation, specimens of high purity nickel were preinjected with hydrogen or helium at 25°C and subsequently irradiated with nickel ions under various conditions. Irradiated samples were prepared for transmission electron microscopy analysis using a cross section technique which allowed evaluation of depth dependent microstructural evolution.

An increase in swelling with increasing injected hydrogen concentration was noted for samples preinjected with hydrogen fluences of 3 x 10^{18} H_3^+/m^2 to 3 x 10^{19} H_3^+/m^2 (100-1000 appm injected and approximately 1-10 appm retained) and subsequently irradiated with nickel ions to a fluence of 2.5 x 10^{20} ions/m^2 at 525°C and 625°C. A dramatic decrease in mean void diameter was noted at 525°C for a preinjection fluence of 3 x 10^{18} H_3^+/m^2. A similar decrease was noted at 625°C for a preinjection fluence of 3 x 10^{19} H_3^+/m^2.

Two methods of helium preinjection were employed. Variable injection energy (200-700 keV) was used to produce uniform helium concentration from the surface of the sample to a depth of 1.25 μm. A monoenergetic preinjection was also used to produce a band of helium concentrated at a depth of 1.25 μm. All helium preinjected samples showed some suppression of swelling due to enhanced cavity nucleation.

Irradiations were also completed at 450°C, 425°C and 400°C to investigate the effect of injected self-interstitials. A suppression of swelling was noted at the end-of-range due to the effect of injected self-interstitials on void nucleation. These observations agree quite well with current models which calculate nucleation rates for these irradiation conditions.

Void formation was noted at depths up to 3.0 μm which was 15-20% beyond the calculated end-of-range of the irradiating ion. This was consistent with the results of previous studies. Comparison of the present work to previous self-ion irradiation studies in Ni suggests a noticeable damage rate effect on swelling rate when the damage is introduced slower than 10^{-3} dpa/sec. There was no clearly observable injected self-interstitial effect at 525°C.

APPROVED:

4/9/84
Date

Professor Gerald L. Kulcinski
Nuclear Engineering Department

ACKNOWLEDGEMENTS

The completion of a major experimental research project requires the cooperation and assistance of a number of people. I wish to express my appreciation to the following people for their guidance and help during the course of this study.

The encouragement and guidance of Professor Gerald L. Kulcinski, my major professor, were greatly appreciated. I also wish to express my thanks to Professor W.G. Wolfer for many enlightening discussions. The support of Professor R.A. Dodd and the guidance of Professor Wilkes, during the early years of this work, were appreciated.

The design and construction of the 700 kV Accelerator Facility required a great deal of effort from a number of people. The advice of Dr. J.H. Billen during this phase was exceptionally helpful. Dr. Billen's assistance with the heavy-ion irradiations was also invaluable. Technical assistance from R.C. Walsh, who machined a number of parts for the experimental equipment, and M.L. Connery, who provided essential electrical work was also greatly appreciated.

My association with fellow graduate students in the Radiation Damage Group has been a most rewarding experience. For their assistance in all phases of my career as a graduate student I wish to thank Dr. R.W. Knoll, Dr. S.K. McLaurin, Dr. R.H. Zee, Dr. H. Attaya, Dr. A. Hassanein, Dr. T. McCarville, R. Lewis, C.A. O'Donnell, R.L.

Jackson, R.L. Sindelar, D.L. Plumton, S.J. Zinkle, C.D. Croessmann, L.E. Seitzman, J.J. Kai, D.H. Plantz, L.M. Wang, and D.J. Pertzborn.

I would like to acknowledge the assistance of Dr. A. West and Mr. R. Casper for their help with the microscopy. I would also like to thank the University of Wisconsin Nuclear Physics group for their cooperation during the tandem irradiations.

I am grateful to Ms. E.A. Brown who typed this thesis. I also wish to thank Mr. D. Bruggink and Ms. H.A. Fack for their assistance in the preparation of the graphics.

Finally, I would like to express my most sincere thanks to my wife, Elizabeth, without whose love, support and constant encouragement the completion of this work would not have been possible and to whom I dedicate this thesis.

This work was supported by the United States Department of Energy.

TABLE OF CONTENTS

LIST OF FIGURES

PAGE

LIST OF TABLES

CHAPTER I

INTRODUCTION

The development of materials for utilization in irradiation environments, such as those present in fusion reactors, poses great problems for the reactor design engineer. Such environments produce high energy neutrons which cause damage to crystalline metals by the production of displacement cascades. A fusion environment will also introduce a large amount of interstitial gas into any first wall material by transmutation reactions such as (n,p) and (n,α), as well as by diffusion of fuel (D,T) and ash (He) atoms into the material. The effect of these factors on microstructural and mechanical properties of fusion materials has been to topic of recent meetings and symposia.[1-5] It is evident that these radiation effects on materials will probably dictate the useful lifetime of fusion reactors.

A. Accelerator Simulation Studies

The primary reaction in proposed operational fusion power reactors is the D-T reaction given by

$$ {}^{2}_{1}D + {}^{3}_{1}T \rightarrow {}^{4}_{2}He\ (3.52\ MeV) + {}^{1}_{0}n\ (14.08\ MeV)\ . \qquad (I\text{-}1) $$

This reaction produces neutrons with energies of 14.08 MeV which will cause a majority of the microstructural damage in the reactor first wall. Since only one source of 14 MeV neutrons for materials research currently exists (RTNS-II)[6], simulation studies using

electrostatic accelerators have long been employed to model the effects of neutron irradiation environments.[7-10] Accelerators may also be used to model the effects of transmutational gas evolution by utilizing dual-ion irradiation[8-15] or by pre-injection of light ions.[11-15] These simulation studies can be compared to the available 14 MeV and fission neutron irradiation data[14] to help predict microstructural evolution in fusion reactor materials.

The use of accelerators for simulation studies is not without shortcomings, however. Accelerators can create displacement damage only within a very small volume of material, usually a few μm below the incident surface. Also, the high damage rates required to model long term irradiation conditions in a reasonable time duration alter the temperature dependence of the development of the microstructure as predicted by Bullough and Perrin.[12] Recent work by Garner[17] addressed the effects of injected interstitials, gas effects and dose rate effects which are other facets of ion irradiation which must be dealt with when comparisons between ion irradiations and neutron irradiations are undertaken. These factors must be taken into account when considering an accelerator simulation study as the one proposed here.

B. Motivation for This Work

This work was undertaken to investigate the effects of interstitial gas atoms on cavity formation in an irradiation environment. The 700 kV Accelerator Facility[18] at the University of Wisconsin was designed and constructed specifically for the purpose of intro-

ducing interstitial gas atoms into samples prior to heavy-ion irradiation. The capabilities of this system allow the injection of either hydrogen or helium atoms. Nickel was selected for this study primarily because it is a pure material which reduces the analysis problems imposed by phase changes and allows for the effect of the gas injection to be more easily evaluated. Another reason for the selection of nickel centers around an innovative method of sample analysis which was originally developed by Whitley[19] for heavy-ion research. Spurling and Rhodes[20] developed a similar technique to study proton irradiated 316 stainless steel. The cross-section technique for TEM sample preparation used by Whitley provides depth dependent damage information in heavy-ion irradiated nickel. This allows for the study of dose and dose rate variations as well as the effects of injected self-interstitials and interstitial gas atoms.

The effects of helium, either preinjected or co-implanted during heavy-ion irradiations, has been studied in detail previously.[8-15] However, the depth dependent microstructure produced in a helium preinjected, heavy-ion irradiated sample is an area which has only recently been investigated.[21] The effect of interstitial hydrogen atoms on cavity formation was initially illustrated by Whitley.[19] However, no quantitative data on hydrogen-content effects in cavity formation has been presented. A more thorough investigation of hydrogen effects is presented in this study.

The role of hydrogen in cavity nucleation is a parameter which has been largely ignored primarily due to concern over the effects of

helium in a similar role. It has also been assumed that due to the high diffusivity of hydrogen in most candidate first wall materials,[22] the effect of hydrogen on the cavity nucleation process would be minimal. With the development of complex computer codes such as DIFFUSE[23] and other calculations which attempt to predict the tritium inventory in fusion reactor first walls, it has been shown by Look and Baskes[24] for Gas Driven Permeation (GDP) that the hydrogen isotope concentration at steady state in the first wall and structural material of an operating fusion reactor can range from 1 to 10 appm for a stainless steel first wall. Recent calculations by Kerst and Swansiger[25] and experiments by Causey et al.[26] indicate the importance of Plasma Driven Permeation (PDP) as a mechanism of hydrogen transport in first wall materials.

Gas Driven Permeation considers the two step process of H_2 dissociation at a surface followed by diffusion into the material. Plasma Driven Permeation bypasses the dissociation step and introduces hydrogen isotopes into the material in the form of charged particles from the plasma. Kerst[25] has shown that the activation energy for PDP is half that for GDP. Hence, when considering PDP it is necessary to double the hydrogen content of first wall materials to 2-20 appm.

The high diffusivity of hydrogen in nickel[22] poses questions pertaining to the amount of hydrogen which remains following preinjection. Recent studies by Wilson et al.,[27-29] which are described in detail in Chapter VI of this report, suggest that 1% of

the hydrogen injected into nickel at 25°C will be trapped. Hence the hydrogen preinjections in this study were completed at 25°C (maximizing hydrogen trapping) to fluences of 3×10^{18} H_3^+/m^2 to 3×10^{19} H_3^+/m^2. These fluences represent injected concentrations of 100 appm to 1000 appm. With 1% trapping, the concentration of retained hydrogen would be approximately 1 appm to 10 appm which is in the range of the steady state hydrogen concentration (2-20 appm) predicted above.

C. Objectives

The 700 kV Accelerator Facility and the Heavy Ion Irradiation Facility were employed in this study to produce radiation damage in pure nickel samples which contained various contents of injected gas. The cross-section technique was employed to evaluate irradiated samples and determine depth-dependent microstructural variations. Utilizing these techniques the objectives of this study were:

1. to expand previous results[19] obtained in heavy ion irradiations of nickel including effect of injected self-interstitials;
2. to quantify the effects of preinjected hydrogen as it relates to swelling, void number density and mean void diameter in self-ion irradiated nickel;
3. to study the role of preinjected helium on cavity formation in self-ion irradiated nickel;
4. to relate the results of this study to other works in order to better understand microstructural evolution in an irradiation environment.

References for Chapter I

1. First Topical Meeting on Fusion Reactor Materials, Miami Beach, FL, Jan. 29-31, 1979, J. Nucl. Matl. 85&86 (1979).

2. Second Topical Meeting on Fusion Reactor Materials, Seattle, WA, Aug. 9-12, 1981, J. Nucl. Matl. 103 (1981).

3. Third Topical Meeting on Fusion Reactor Materials, Albuquerque, NM, Sept., 1983, to be published in J. Nucl. Matl.

4. Fifth International Conference on Plasma Surface Interactions in Controlled Fusion Devices, Gatlinburg, TN, May 3-7, 1982, J. Nucl. Matl. 111&112 (1982).

5. Symposium on Radiation Damage Analysis for Fusion Reactors, St. Louis, MO, Oct. 25-28, 1982, J. Nucl. Matl. 117 (1983).

6. G.L. Kulcinski, Fusion Reactor Design Concepts, International Atomic Energy Agency, IAEA-TC-145/37 (1978) 573-599.

7. G.L. Kulcinski, J.J. Laidler, and D.G. Doran, Radiation Effects 7 (1971) 195-202.

8. H.E. Kissinger, J.L. Brimhall, E.P. Simonen, and L.A. Charlot, Battelle Report PNL-2495, UC-25 (1978).

9. F.V. Nolfi, Jr., A. Taylor, and G.S. Grabowski, IEEE Transactions on Nuclear Science NS-26 No.1 , (Feb 1979) 1257-1265.

10. J.L. Brimhall, IEEE Transactions on Nuclear Science NS-28, No. 2, (April 1981) 1308-1311.

11. S.C. Agarwal, G. Ayrault, D.I. Potter, A. Taylor, and F.V. Nolfi, Jr., J. Nucl. Matl. 85&86 (1979) 653-657.

12. N.H. Packan, from Second Topical Meeting on Fusion Reactor Materials, Aug. 9-12, 1981, Seattle, WA, J. of Nucl. Matl. 103&104 (1981) 1029.

13. N.H. Packan and K. Farrell, J. Nucl. Matl. 85&86 (1979) 677-681.

14. N.H. Packan, K. Farrell, and J.O. Stiegler, J. Nucl. Matl. 78 (1978) 143-155.

15. J.A. Spitznagel, F.W. Wiffen, and F.V. Nolfi, J. Nucl. Matl. 85&86 (1979) 629-646.

16. R. Bullough and R.C. Perrin, Irradiation Effects on Structural Alloys in Nuclear Reactor Applications, ASTM STP 484, p. 317 (1970).

17. F.A. Garner, J. Nucl. Matl. 117 (1983) 117-197.

18. R.L. Sindelar and D.B. Bullen, University of Wisconsin Fusion Engineering Program Report UWFDM-501 (April 1983).

19. J.B. Whitley, Ph.D. Thesis, University of Wisconsin, Madison, Wisconsin, 1978.

20. R.A. Spurling and C.G. Rhodes, J. Nucl. Matl. 44 (1972) 341.

21. K. Farrell, N.H. Packan and J.T. Houston, Rad. Effects 62 (1982) 39-52.

22. S.A. Steward, "A Review of Hydrogen Isotope Permeability Through Materials," Report UCRL-53441, Lawrence Livermore National Laboratory, Aug. 15, 1983.

23. M.I. Baskes, Sandia National Laboratory Livermore Report SAND80-8201 (1980).

24. G.W. Look and M.I. Baskes, J. Nucl. Matl. 85&86 (1979) 995-999.

25. R.A. Kerst and W.A. Swansiger, to be published in J. Nucl. Matl.

26. R.A. Causey, R.A. Kerst and B.E. Mills, to be published in J. Nucl. Matl.

27. K.L. Wilson and A.E. Pontau, J. Nucl. Matl. 85&86 (1979) 989-993.

28. K.L. Wilson, A.E. Pontau, L.G. Haggmark, M.I. Baskes, J. Bohdansky and J. Roth, J. Nucl. Matl. 103&104 (1981) 493-498.

29. K.L. Wilson and M.I. Baskes, J. Nucl. Matl. 111&112 (1982) 622-627.

CHAPTER II

THEORY OF IRRADIATION INDUCED CAVITY FORMATION

A. Point-Defect Production

High energy irradiation of crystalline solids such as metals causes displacement of atoms from normal lattice sites which results in the formation of vacancies and interstitials in the form of Frenkel pairs. For particle irradiations (i.e., electrons, neutrons, light ions or heavy ions) the number and spatial distribution of these Frenkel pairs depends very strongly on the energy of the particle as well as the type of particle. High energy electron irradiations cause the formation of a few (1-2) isolated point defect pairs, while high energy neutrons or heavy ions can cause the formation of a displacement cascade.

The displacement cascade is initiated when a lattice atom is given a quantity of energy during an elastic collision with a fast neutron which is much greater than the energy required to displace the atom from its lattice site. This atom, which is called a primary knock-on atom (PKA), becomes immediately ionized and dissipates its energy in the form of electronic interactions with lattice atoms, which cause no further displacements, and by elastic displacement collisions with other lattice atoms in a cascading effect. Due to the very high collision cross section for these knock-on atoms, the PKA dissipates energy in a very small region. This causes a large

number of Frenkel pairs to be produced resulting in localized areas of vacancy and interstitial supersaturation.

Displacement cascades are produced during the ion irradiations conducted in this study. However, due to the limited range of a charged particle in metal (as compared to a neutron), the spatial distribution of displacement cascades is compressed. The cross section for elastic nuclear collisions increases with decreasing energy and therefore, the number of PKA's produced by an incident ion increases near the end of range of the irradiating ion. The number of Frenkel pairs produced at the end of range may be factors of 5 to 10 greater than those produced at the surface.

The mass of the incident ion is extremely important in determining the amount of energy imparted to the PKA. As noted in Olander,[1] the energy transferred (T) between two particles in a binary collision is given by

$$T = \frac{1}{2} \Lambda E(1 - \cos \theta) \qquad \text{(II-1)}$$

where E is the kinetic energy of the incident ion, θ is the scattering angle in the center-of-mass coordinate system and Λ is given as

$$\Lambda = \frac{4 M_1 M_2}{(M_1 + M_2)^2} \qquad \text{(II-2)}$$

M_1 is the mass of the incident ion and M_2 is the mass of the recoil atom. Since the mass of the incident ion in this study ranges from

that for hydrogen ($^{1}_{1}H^{+}$) and helium ($^{4}_{2}He^{+}$) to nickel ($^{59}_{28}Ni^{2+}$), it is evident that accurate indication of the damage produced in the irradiated material may not be determined by merely knowing the fluence of incident ions. Therefore, the unit "displacement per atom (dpa)" is introduced in the next section to provide a basis for comparison between different irradiation experiments.

A.1. Calculation of Displacement Damage (DPA)

The basic unit of radiation damage, the displacement per atom, is defined as the average number of times a lattice atom has been forced from its original lattice site to an interstitial site during an irradiation. Calculation of the damage produced during an irradiation with mono-energetic ions includes: (a) the determination of the energy losses due to electronic interactions and nuclear collisions as a function of depth, x, from the incident surface, and (b) the calculation of the number of displacements produced at x using a suitable model. Lindhard, Scharff and Schoitt (LSS), as well as others[2-8] have developed the most widely used and accepted model for determining energy loss of an ion slowing down in an amorphous solid. The LSS theory, which assumes total separability for electronic and nuclear scattering energy loss mechanisms, is based on the nuclear-stopping cross section calculated from the Thomas-Fermi atomic model. This theory is applicable to many target-projectile combinations over a wide energy range.

A screened-coulomb potential, involving only one screening parameter, a, is utilized by LSS[3] for scattering interaction calcu-

lations where

$$a = 0.8853\, a_o (Z_1^{2/3} + Z_2^{2/3})^{-1/2} \quad . \tag{II-3}$$

Z_1 is the projectile atomic number, Z_2 is the target atomic number, and a_o is the Bohr radius. LSS now introduces the following dimensionless groups for the case of ions colliding with atoms at rest. The reduced energy is given by

$$\varepsilon = E \frac{aM_2}{Z_1 Z_2 e^2 (M_1 + M_2)} \tag{II-4}$$

and the reduced range is given by

$$\rho = 4\pi a^2 RNM_2 \frac{M_1}{(M_1 + M_2)^2} \tag{II-5}$$

where E is the projectile energy, R is the range, N is the atomic density, and M_1 and M_2 are the projectile and target mass, respectively. The scattering by the screened coulomb potential is obtained during the extrapolated perturbation method for classical scattering. Lindhard then obtains a universal differential scattering cross section

$$d\sigma = \pi a^2 \frac{dt}{2t^{3/2}} f(t^{1/2}) \tag{II-6}$$

where $t^{1/2} = \varepsilon \sin(\theta/2)$ and θ is the scattering angle in the center-

of-mass coordinate system. Assuming elastic collisions, Lindhard finds $\sin^2(\theta/2) = T/T_m$ where T and T_m are the energy transferred to the PKA and the maximum energy of the PKA possible from conservation of momentum, respectively. Lindhard et al.[3] have numerically calculated the function $f(t^{1/2})$ for a Thomas-Fermi potential. Winterbon et al.[5] obtain an analytical approximation for $f(t^{1/2})$ which is given by

$$f(t^{1/2}) = 1.309\ t^{1/6}\ [1 + (2.618\ t^{2/3})^{2/3}]^{-3/2}\ . \qquad \text{(II-7)}$$

Employing Eqs. II-4 and II-5 a dimensionless form of the nuclear stopping cross section is given by

$$\left(\frac{d\varepsilon}{d\rho}\right)_n = \int_0^{\varepsilon} \frac{dx\ f(x)}{\varepsilon} \qquad \text{(II-8)}$$

where $x = t^{1/2}$. It should be noted that the above treatment is only valid for energies large enough that the collision interaction can be described by the Thomas-Fermi potential. This condition is usually met when $\varepsilon > 0.01$.[2]

LSS theory assumes the electronic stopping is proportional to ion velocity,[6-8] which in the reduced form looks like

$$\left(\frac{d\varepsilon}{d\rho}\right)_e = k\sqrt{\varepsilon} \qquad \text{(II-9)}$$

where k is a constant which varies slowly with Z_1 and Z_2 (usually

$0.1 < k < 0.2$). For nickel ions incident on nickel, $k = 0.162$. Equation II-9 is valid for energies less than $25\ Z_1^{4/3}A_1$ (keV) which implies that for Ni on Ni, the ion energies must be less than 123 MeV. Experimental evidence indicates that Eq. II-9 may overestimate the electronic stopping for heavy ion irradiations of nickel. Cross section techniques employed by Whitley[9,11] and Narayan[10] to study the depth distribution of damage in self-ion irradiated nickel specimens show that the damage peak calculated using the electronic stopping proposed by LSS is approximately 15-20% too near the incident surface. These experimental damage profiles are compared to calculated damage energy versus depth curves using the Manning-Mueller[12] computer code E-DEP-1.

Brice[13] proposes a more intricate three-parameter formula for the inelastic energy loss function S(E) given by

$$S(E) = N(Z_1 + Z_2)S_e(u)f(u) \qquad \text{(II-10)}$$

where

$$S_e(u) = A\{u^{1/2}[\frac{30u^2 + 53u + 21}{3(1 + u)^2}] + (10u + 1)\ \arctan(u^{1/2})\} \qquad \text{(II-11)}$$

and

$$f(u) = [1 + (4Z^2a'^2u)^{n/2}]^{-1} \qquad \text{(II-12)}$$

A is a constant with value $A = 1.2192 \times 10^{-15}$ eV-cm^2/atom. The

dimensionless variable u is related to the energy E through

$$u = \frac{E}{(Z^2 M_1 E_1)} \qquad \text{(II-13)}$$

where E_1 = 100 keV, Z, a' and n are adjustable parameters determined by fitting Eq. II-10 to experimental stopping power values, and are tabulated by Brice[13] for various incident and target ions. Comparison of Brice calculation to nickel ion irradiations[9] still indicates about a 6% discrepancy in projected range.

The total stopping cross section is merely the sum of Eqs. II-8 and II-9, which is used to determine the average ion path length ρ given by

$$\rho = \int_0^{\varepsilon} d\varepsilon \left[\left(\frac{d\varepsilon}{d\rho}\right)_n + \left(\frac{d\varepsilon}{d\rho}\right)_e \right]^{-1} \quad . \qquad \text{(II-14)}$$

Using this path length, the range-energy relationships for most ion-target combinations may be calculated.

The displacement rate as a function of depth into the material may now be determined providing the total energy loss through nuclear elastic collisions is known. A simple relationship relating the average energy dissipated by the incident ion, E(x), to the energy loss through nuclear elastic collision is proposed by Lindhard et al.[4] and has the form

$$S_D(x) = \frac{E(x)}{1 + kg(\varepsilon)} \qquad \text{(II-15)}$$

where $g(\varepsilon)$ is a function such that $g(\varepsilon)$ approaches zero as ε approaches zero and $g(\varepsilon)$ approaches ε for large ε ($\varepsilon > 100$). Robinson[15] obtains a numerical approximation of the form

$$g(\varepsilon) = 3.4008\ \varepsilon^{1/6} + 0.40244\ \varepsilon^{3/4} + \varepsilon \quad . \qquad \text{(II-16)}$$

The number of displacements per atom (dpa) may now be calculated using a modified Kinchen-Pease model proposed by Torrens and Robinson[15] yielding the equation

$$\text{dpa} = \frac{J}{N} \frac{\beta S_D(x)}{2E_d} \qquad \text{(II-17)}$$

where J is the ion fluence and N is the atomic density of the target. The factor β is the displacement efficiency which depends on the form of the interatomic potential assumed in the model. Computer studies by Torrens and Robinson[15] of displacement cascades in cubic material indicate that $\beta \simeq 0.8$. More recent work by Guinan and Kinney[34] suggests that for heavy ion irradiation a displacement efficiency of 0.25-0.30 is more correct. However, to avoid confusion when comparisons are made to previous self-ion irradiated nickel studies, this author will continue to use $\beta = 0.80$. The displacement energy (E_d) represents the amount of energy which must be transferred to a lattice atom to remove it from its lattice site. This displacement energy is strongly dependent on the crystallographic direction in which the atom is displaced. In nickel, the threshold displacement

energy as a function of crystallographic orientation has been tabulated by Mitchell, Das and Kenik.[16] The displacement energies are 31 eV for the <100> orientation, 23 eV for the <110> orientation and 28 eV for the <111> orientation. Considering 6 <100>, 12 <110>, and 8 <111> orientations for a single crystal and computing a simple weighted average, one obtains an average displacement energy of about 26 eV. This value is similar to values used for previous work on nickel.[9,10]

The Brice code[17] has been employed in this study to determine the displacement damage and deposited ion distribution as a function of depth from the incident surface. Results of these calculations for H → Ni, He → Ni and Ni → Ni beams used in this study are shown in Figs. II-1, II-2, and II-3, respectively. Note that Brice calculations for hydrogen irradiations of nickel use an incident hydrogen ion energy of 233 keV. This is due to the fact that the predominant beam produced by the 700 kV accelerator ion source is H_3^+ since the source was intially tuned to produce He^+ ions. Hence, the energy of an incident H^+ ion upon dissociation at the surface of the nickel at impact is 700/3 or 233 keV.

A.2. Spatial Considerations of Damage

A knowledge of the dpa level alone is not an accurate indication of the radiation damage caused by a displacement cascade. The long term damage effects are not necessarily dependent on the number of point defects formed, but rather the number of point defects which remain in the lattice after annealing of the displacement cascade.

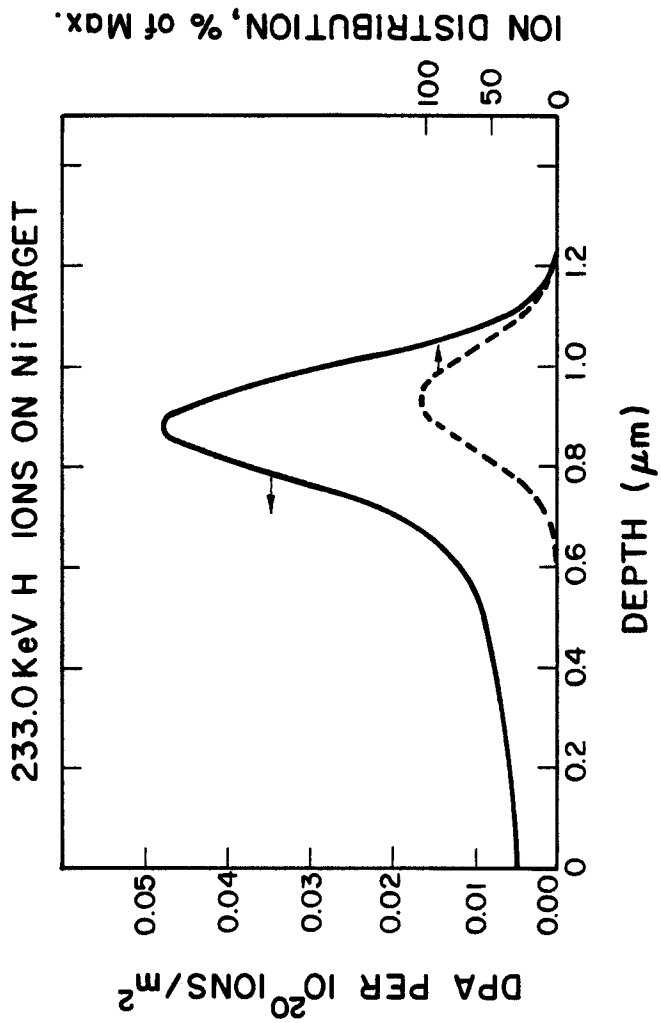

Fig. 11-1. Displacement damage vs. depth for 233 keV H^+ ions incident on Ni as calculated using the Brice[17] code. The calculations were completed by Croessmann and Attaya.[18]

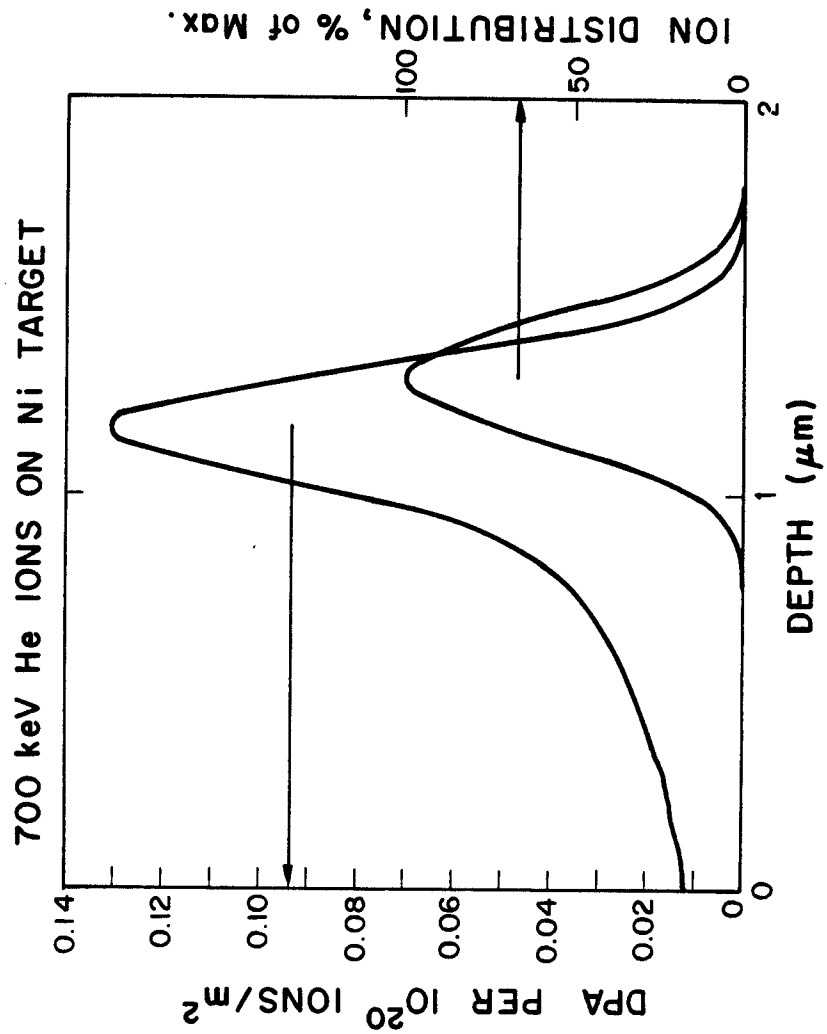

Fig. II-2. Displacement damage vs. depth for 700 keV He^+ ions incident on Ni as calculated using the Brice[17] code. The calculations were completed by Croessmann and Attaya.[18]

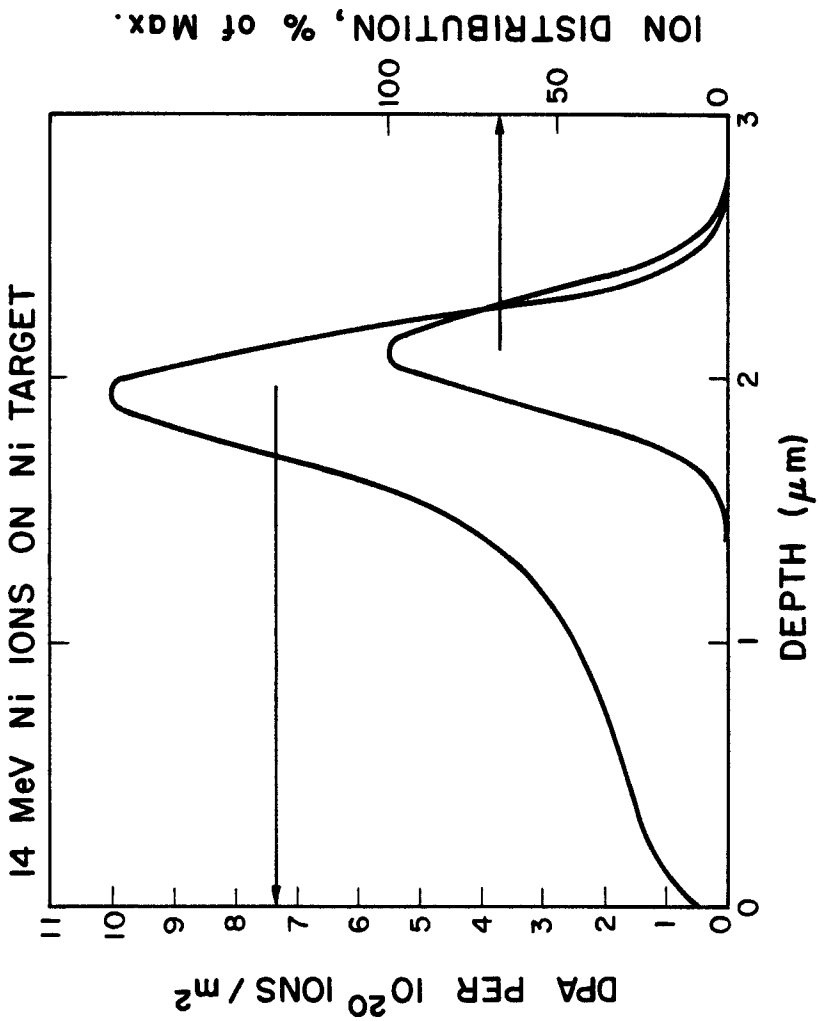

Fig. II-3. Displacement damage vs. depth for 14 MeV Ni ions incident on Ni as calculated using the Brice(17) code. The calculations were completed by Croessmann and Attaya.(18)

The survivability of point defects is thus highly dependent on the spatial distribution of the damage events.

The time scale of the formation and annealing of a damage cascade is much too short (~ 10^{-6} sec) to allow for experimental observation. Hence, most data on the behavior of the point defects in a cascade has been obtained from computer simulation studies.[1] These studies indicate the formation of a vacancy rich core surrounded by an interstitial rich shell during the cascade event. This unstable configuration exists for approximately 10^{-13} sec, at which time a 10^{-8} to 10^{-10} sec anneal occurs and a majority of the point defects recombine. The defects which remain may condense into clusters or migrate to sinks within the lattice. The defect clusters which form may act as nucleation sites for secondary defects such as dislocation loops or voids as described in the following section. Computer simulation studies such as those completed by Doran[19] utilizing a Monte Carlo method indicate that fewer than 20% of the defects produced in a 20 keV cascade at 525°C survive the anneal. Of these defects only 7% were monovacancies while the remaining 13% were immobile clusters.

B. Cavity Nucleation

The high concentrations of point defects produced in an irradiation environment are mobile at sufficiently high temperatures ($T > 0.3\ T_m$) and can thus escape recombination within the displacement cascade and diffuse throughout the matrix. An equilibrium condition is quickly reached during a steady state irradiation as the rate of production of vacancies and interstitials is balanced by the rate of

loss due to recombination in the matrix and absorption at sinks (e.g., dislocations, defect clusters, free surfaces, and grain boundaries). This concentration of point defects in the matrix during irradiation is considerably greater than the thermal equilibrium concentrations $C_{i,v}^{eq}$ and thus the material is supersaturated by an amount

$$S_{i,v} = \frac{C_{i,v}}{C_{i,v}^{eq}} \qquad \text{(II-18)}$$

where C_i and C_i^{eq} represent the concentration of interstitials and the thermal equilibrium concentration of interstitials and C_v and C_v^{eq} represent the concentration of vacancies and the thermal equilibrium concentration of vacancies, respectively.

The precipitation of clusters of point defects from the supersaturation present during irradiation can take a number of forms. The excess vacancies can condense into a two-dimensional vacancy loop and the excess interstitials can form interstitial loops, both of which leave the macroscopic volume of the material unchanged. However, the excess vacancies can also condense or nucleate three-dimensional cavities or voids and swelling of the material occurs. The implications of void formation on the structural reliability of metals in an irradiation environment has prompted intense interest in the mechanism of void formation.

The evolution of voids or cavities in a material was initially considered as a sequential process of nucleation and growth, even

though in an irradiation environment nucleation and growth can occur simultaneously. This sequential modeling was initially employed since there existed a similarity to classical nucleation theory which allowed the reduction of a large system of equations to a much simpler analytic expression. It was evident however, that classical nucleation theory could not be used to completely describe void nucleation due to the nature of the irradiation process. Since a defect cluster, such as a void or vacancy loop, grows with the addition of a vacancy or the emission of an interstitial (not likely), or shrinks with the addition of an interstitial or the emission of a vacancy, classical nucleation theory needed modification. Other reasons for modification of classical nucleation theory as it relates to irradiation microstructure formation included the fact that irradiation induced defect structures form from continuously created defects while precipitates in classical nucleation form from a fixed population. For these reasons Katz and Wiedersich[20] and Russell[21] developed theories of homogeneous nucleation of voids in the absence of gas or impurity atoms, which are described below.

Stable vacancy cluster nucleation requires that the following conditions be satisfied:

a. A vacancy supersaturation must exist.

b. The vacancies must be highly mobile.

c. A net flux of vacancies must flow to the cluster, or the cluster must be biased for vacancy rather than interstitital absorption.

The first two conditions are usually met when the temperature of the

metal during irradiation is between 0.3 T_m and 0.6 T_m (T_m = absolute melting temperature) and there is not a high defect trap concentration. The microstructure of the material determines whether or not the third condition is met.

Russell[22] proposed a number of possible mechanisms by which nucleation may occur. They include:

a. Homogeneous nucleation of vacancies and interstitials only.
b. Heterogeneous nucleation on immobile gas atoms or gas atom clusters.
c. Nucleation with simultaneous mobile gas atom, vacancy and interstitial precipitation.
d. Collapse of vacancy rich displacement cascade cores into vacancy clusters.
e. Nucleation in the presence of surface active impurities.

Treatment of these possible mechanisms with classical nucleation theory involves the assumption that the concentration of all clusters be kept at a constant level while the rate of flow between clusters of neighboring sizes is calculated. Including only reactions between clusters of neighboring size, nucleation then proceeds along a one-dimensional path. Hence, the net flux between clusters containing n and (n + 1) vacancies is given by

$$J_n = \beta_v(n)\rho(n) - \alpha_v(n + 1)\rho(n + 1) - \beta_i(n + 1)\rho(n + 1) \quad \text{(II-19)}$$

where $\rho(n)$ and $\rho(n + 1)$ are the number of clusters containing n and

$(n + 1)$ vacancies respectively. $\beta_v(n)$ is the vacancy arrival rate for a cluster of size n, $\beta_i(n + 1)$ is the interstitial arrival rate for a cluster of size $(n + 1)$, and $\alpha_v(n + 1)$ is the vacancy emission rate for a cluster of size $(n + 1)$. Due to the extremely low probability of occurrence, the interstitial emission rate is assumed to be zero.

The vacancy emission rate is determined using a constrained equilibrium assumption ($\beta_i(n) = 0$ for all n and $J_n = 0$) or assuming local thermodynamic equilibrium for the n-cluster and its surroundings. For these equivalent cases it can be shown[4]

$$C(n) = C_v^{eq} \exp\left[\frac{-\gamma s(n)}{kT}\right] \qquad \text{(II-20)}$$

where C_v^{eq} is the thermal equilibrium vacancy concentration, γ is the surface energy, and s(n) is the surface area of a cluster containing n vacancies. Rearrangement of Eq. II-19 yields

$$\alpha_v(n + 1) = \beta_v(n) \frac{C_v^{eq}}{C_v} \exp\left\{\frac{\gamma[s(x + 1) - s(x)]}{kT}\right\} \qquad \text{(II-21)}$$

The constrained equilibrium conditions can be used to define the constrained cluster size distribution $C^o(n)$, which is derived from Eq. II-19 by setting J_n = const. This yields a recursive relationship for $C^o(n)$ given by

$$C^o(n + 1) = C^o(n)\left(\frac{\beta_v(n)}{\alpha_v(n + 1) + \beta_i(n + 1)}\right) \qquad \text{(II-22)}$$

An effective free energy, $\Delta G(n)$, may also be defined similar to classical nucleation theory such that

$$C^{o}(n) = C_{v}\exp\{\frac{-\Delta G(n)}{kT}\} \qquad \text{(II-23)}$$

$\Delta G(n)$ would represent the free energy of formation of a cluster of size n for conventional nucleation. However, due to the fact that void nucleation takes place in an irradiation environment, this free energy of formation is not so simply described and loses its physical significance, especially when considering transmutation impurities and insoluble gas atoms.

Using the constrained cluster distribution and assuming that the vacancy concentration is independent of nucleation rate and the concentration of very large clusters is nearly zero, the nucleation rate may be determined from Eq. II-19 to be

$$J = [\sum_{n=1}^{x}[\beta_{v}(n)C^{o}(n)]^{-1}]^{-1} \qquad \text{(II-24)}$$

where x is a large value such that J is not a function of x.

The calculation of the nucleation rate now requires the determination of the arrival rates of the vacancies and interstitials. Katz and Wiedersich[23] and Russell[22] calculate the arrival rates for type k defects to be of the form

$$\beta_{k}(n) = C_{k}D_{k}\frac{n^{2/3}}{a^{2}} \qquad \text{(II-25)}$$

where C_k and D_k are the concentration and diffusivity of the type k defect, a is the lattice constant and n is the cluster size. A more thorough investigation by Wolfer and Yoo[24] shows the absorption rates to be of the form

$$\beta_k(n) = 4\pi b n^{1/3} Z_k^o(n) D_k C_k \qquad \text{(II-26)}$$

where b is the Burgers vector and $Z_k^o(n)$ is a bias factor.

For a pure material, Wolfer and Yoo obtained two contributions to the bias factor. The first contribution, that due to the image interaction, assumes no surface tension and no gas pressure in the cavity and has the form

$$Z_k^{im} \cong 1 + \left[\frac{G\Omega}{kT} \frac{(1+\nu)}{36\pi(1-\nu)}\right]^{1/3} \left(\frac{v}{\Omega}\right)^{2/3} \frac{b}{r} \qquad \text{(II-27)}$$

where r is the cavity radius, ν is Poisson's ratio, G is the shear modulus, Ω is the atomic volume, and v is the relaxation volume of the point defect.

The second contribution to the bias factor is obtained when the surface tension, σ, and the gas pressure, p, are considered. The surface tension and pressure give rise to a radial stress component on the cavity surface of the form

$$\frac{2\sigma}{r} - p \qquad \text{(II-28)}$$

The bias factor resulting from this interaction between the shear strain field of the cavity and the point defect has the form

$$Z^s = 1 - \frac{3}{56}\frac{\alpha_k}{kT}\left(\frac{2\sigma/r - p}{G}\right)^2 \qquad \text{(II-29)}$$

where α_k is the polarizability for point defects of type k. The compound bias factor, including both the image interaction and shear strain field interaction, is given by the product of the two contributions

$$Z_k^o = Z_k^{im} Z_k^s \qquad \text{(II-30)}$$

The effect of soluble impurities, such as hydrogen, can substantially alter the nucleation rate. The effect of a surface active impurity on void nucleation was initially calculated by Russell[21,22] using a simple adsorption model which assigned a lower energy, E_b, to the adsorbed atoms giving a surface energy

$$\sigma(C_x) = \sigma(0) - n_s kT \ln\left(1 + C_x \exp\left(\frac{E_b}{kT}\right)\right) \qquad \text{(II-31)}$$

where $\sigma(C_x)$ and $\sigma(0)$ are the surface energies with and without adsorption, n_s is the number of possible surface sites per unit area and C_x is the matrix solute concentration. Wolfer[35] recently addressed the effect of chemisorbed hydrogen on void nucleation in nickel noting a reduction in surface energy of -0.2 J/m^2 at 500°C for

a hydrogen concentration of 10 appm. This reduction in surface energy enhances the nucleation rate.

C. Cavity Growth

The most widely used model for the growth of cavities in a supersaturation of point defects, such as found in an irradiation environment, is based on the formalism of chemical rate theory. This model describes physical processes which are discrete in time and space as occurring continuously and homogeneously throughout the material. For the case of cavity growth, the rate of change of point defect concentration or the growth of defect clusters is defined using conservation equations. Reaction rate coefficients are used to describe relevant physical processes. Current rate theory analysis of cavity growth in an irradiation environment, described in review articles by Brailsford and Bullough[25] and Mansur[26], have been used as a guide for the development of this section.

Application of chemical rate theory to cavity growth was first proposed by Harkness and Li[27] and was further developed by Brailsford and Bullough[28] and Wiedersich.[29] The rate equations proposed in these original works are of the form

$$\frac{\delta C_v}{\delta t} = \nabla \cdot \{D_v \nabla C_v + \frac{D_v C_v}{kT} \nabla U_v\} + G_v - RC_v C_i - K_v C_v \qquad \text{(II-32)}$$

$$\frac{\delta C_i}{\delta t} = \nabla \cdot \{D_i \nabla C_i + \frac{D_i C_i}{kT} \nabla U_i\} + G_i - RC_v C_i - K_i C_i \qquad \text{(II-33)}$$

where the spatial derivatives describe leakage and drift to a sink

such as a surface. The subscripts v and i denote vacancies and interstitials, D is the diffusion coefficient, K is the reaction rate constant describing loss to sinks, U is the interaction energy between point defects and discrete sinks, k is Boltzmann's constant, T is absolute temperature, G is the effective point defect generation rate per unit volume and t is the time. The recombination coefficient R equals $4\pi r_o(D_i + D_v)$ where r_o is the radius of the point defect recombination volume.

Since relaxation times for changes in the concentrations are much shorter than those for the evolution of sink strengths, the time derivatives may be dropped, yielding quasi-steady state concentrations with instantaneous sink strengths of the form[28]

$$C_v = \frac{[K_i K_v + R(G_i - G_v)]}{2RK_v} \left\{\left[1 + \frac{4RG_v K_i K_v}{[K_i K_v + R(G_i - G_v)]^2}\right]^{1/2} - 1\right\} \quad \text{(II-34)}$$

$$C_i = \frac{[K_i K_v + R(G_v - G_i)]}{2RK_i} \left\{\left[1 + \frac{4RG_v K_v K_i}{[K_i K_v + R(G_v - G_i)]^2}\right]^{1/2} - 1\right\} \quad \text{(II-35)}$$

These quasi-steady state concentrations are used to determine growth rates of defect clusters.

The growth rate of a void of radius r is determined by the net flux of vacancies per unit void area per unit time given by[27]

$$\frac{dr_v}{dt} = \frac{\Omega}{r_v} \{Z_v^v(r_v)D_v[C_v - C_v^e(r_v)] - Z_i^v(r_v)D_i C_i\} \quad \text{(II-36)}$$

where $C_v^e(r_v)$ is the thermal vacancy concentration at a void of radius r_v. $C_v^e(r_v)$ is given by

$$C_v^e(r_v) = C_v^e \exp\left[-\left(P_g - \frac{2\gamma}{r_v}\right)\frac{\Omega}{kT}\right] \qquad \text{(II-37)}$$

where C_v^e is the bulk thermal vacancy concentration, P_g is the internal gas pressure of the void, λ is the void surface tension, and Ω the atomic volume.

Substitution of Eqs. II-34 and II-35 into Eq. II-36 yields the defect cluster growth rates for voids. Many simplifications and predictions of limiting cases for the solution of the growth rate equation have been proposed and applied to allow numerical solutions.[26-29]

Once the void growth rate has been calculated, the swelling rate may be determined by substitution into

$$\frac{d}{dt}\left(\frac{\Delta V}{V}\right) = 4\pi \int r_v n(r_v,t) \frac{dr_v}{dt} dr_v \qquad \text{(II-38)}$$

where $\Delta V/V$ is the void volume fraction. This equation yields explicit analytic predictions for the dose dependence of swelling and allows for direct comparison of the chemical rate formalism to experimental data.

D. Gas Effects

Initial treatment of the effect of gas atoms on the nucleation and growth of cavities in an irradiation environment considered the

gas atoms contained in subcritical cavities to behave as an ideal gas. Recent investigations[30-32] have shown that at the pressures required to stabilize cavity embryos, the ideal gas law breaks down for all gases, even helium. Recent works by Parker and Russell[30] and Mansur and Coghlan[33] have selected another gas law, the modified Van der Waals equation of state. One reason for selection of this equation is that it allows for analytical solutions for the critical radius and critical number of gas atoms as can be seen in the following discussion.

Recalling Eqs. II-36 and II-37, which describe the growth rate of a cavity in an irradiation environment, one can employ a modified Van der Waals equation of state to describe P_g, the gas pressure in the cavity where:

$$P_g = \frac{n_g kT}{\frac{4}{3}\pi r_c^3 - n_g B} \qquad \text{(II-39)}$$

where as B approaches zero this equation becomes the ideal gas pressure. Glasgow and Wolfer[31] have determined the constant B as a function of temperature for helium. This has been evaluated by Mansur[33] as

$$B = 6.65 \times 10^{-27}\left[4.5 \times 10^{-4} + \frac{5.42}{1890 + T}\right] . \qquad \text{(II-40)}$$

The growth rate of a cavity containing a fixed number of gas atoms may now be determined from Eq. II-36 utilizing Eqs. II-37 and

II-39 along with defect concentrations described by Mansur.[33] When the vacancy emission rate due to thermal effects equals the radiation induced growth rate, $dr_c/dt = 0$, and Eq. II-36 yields

$$r_c = \frac{2\gamma}{P_g + \frac{kT}{\Omega} \ln \left[(1 - Z)(C_v/C_v^o) + Z\right]} . \qquad \text{(II-41)}$$

Applying the restrictions that the only point defect loss processes are mutual recombination, cavities and dislocations with dislocations the dominant of the two sinks and using the definition

$$f = \frac{kT}{\Omega} \ln \left[\frac{(1 - Z)C_v}{C_v^o} + Z\right] . \qquad \text{(II-42)}$$

Mansur rewrites Eq. II-41 as

$$g(r_c) = r_c^4 - \frac{2\gamma}{f} r_c^3 + \frac{3n_g(kT - Bf)}{4\pi f} r_c - \frac{3\gamma n_g B}{2\pi f} = 0 \qquad \text{(II-43)}$$

which has four roots. Two of these roots represent the stable radius r_c^s and the critical radius r_c^c. The stable radius represents the size to which small overpressurized cavities grow by absorbing vacancies. The critical radius is the size as above which cavities grow due to the defect bias.

A special case exists when the critical radius and the stable radius are equal. This occurs when $g = dg/dr_c = 0$. By differentiating Eq. II-43, setting it equal to zero, solving for n_g and substituting back into Eq. II-43 yields,

$$r_c^2 + \left[\frac{8\gamma B}{3(kT - Bf)} - \frac{4\gamma}{3f}\right] r_c - \frac{4\gamma^2 B}{f(kT - Bf)} = 0 \ . \qquad \text{(II-44)}$$

The roots of Eq. II-44 give a minimum critical radius r_c^{c*}

$$r_c^{c*} = \frac{2\gamma}{3f}\left\{\left[\frac{kT - 3Bf}{kT - Bf}\right](1 \pm \sqrt{1 + n})\right\} \qquad \text{(II-45)}$$

where

$$n = \frac{\left(16B/f(kT - Bf)\right)}{\left((8B/3)/(kT - Bf) - (4/3f)\right)^2} \ . \qquad \text{(II-46)}$$

The critical number of gas atoms is found using Eqs. II-45 and II-46 and $dg/dr_c = 0$ as

$$n_g^* = \frac{8\pi r_c^{c*}}{3(kT - Bf)}\left(3\gamma - 2fr_c^{c*}\right) \ . \qquad \text{(II-47)}$$

As before, as B approaches zero, this solution approaches the ideal gas solution.

The above results can now be used as a benchmark for helium (or other gas) inventories of irradiated material in hopes of obtaining better agreement between calculated and experimentally observed cavity growth in irradiated materials.

References for Chapter II

1. D.R. Olander, Fundamental Aspects of Nuclear Reactor Fuel Elements, Ch. 17, ERDA Technical Information Center Document, TID-26711-P1, 1976.

2. J. Lindhard, V. Nielsen, and M. Scharff, Mat. Fys. Medd. Dan. Vid. Selsk. 63, No. 10 (1968).

3. J. Lindhard, M. Scharff, and H.E. Schoitt, Mat. Fys. Medd. Dan. Vid. Selsk. 33, No. 14 (1963).

4. J. Lindhard, V. Nielsen, M. Scharff, and P.V. Thomsen, Mat. Fys. Med. Dan. Vid. Selsk. 33, No. 10 (1963).

5. K.B. Winterbon, P. Sigmund, and J.B. Sanders, Mat. Fys. Medd. Dan. Vid. Selsk. 37, No. 14 (1970).

6. J. Lindhard and M. Scharff, Mat. Fys. Medd. Dan. vid. Selsk. 27, No. 15 (1953).

7. N. Bohr and J. Lindhard, Mat. Fys. Medd. Dan. Vid. Selsk. 28, No. 7 (1954).

8. J. Lindhard and M. Scharff, Phys. Rev. 124, No. 1, (Oct. 1, 1961) 128-130.

9. J.B. Whitley, P. Wilkes and G.L. Kulcinski, UWFDM-159, June 1976.

10. J. Narayan and O.S. Oen, J. Nucl. Mat. 66 (1977) 158-162.

11. J.B. Whitley, Ph.D. Thesis, University of Wisconsin, Madison, Wisconsin (1978).

12. I. Manning and G.P. Mueller, Computer Physics Comm. 7, 85-94.

13. D.K. Brice, Phys. Rev. A6 (1972) 1791.

14. D.K. Brice, Ion Implantation Range and Energy Depositon Distributions, Vol. 1, IFI/Plenum, New York, (1975).

15. M.T. Robinson, Nuclear Fusion Reactors, British Nuclear Energy Society, London, p. 364 (1970).

16. T.E. Mitchell, G. Das, and E.A. Kenik, Fundamental Aspects of Radiation Damage in Metals, pp. 73-79, CONF-751006-P1, Gatlinburg, TN, October 6-10, 1975.

17. D.K. Brice, SAND-7500622, Sandia Laboratories, Albuquerque, NM, July 1977.

18. C.D. Croessmann and H. Attaya, private communication.

19. D.G. Doran, Rad. Effects 2 (1970) 249.

20. J.L Katz and H. Wiedersich, J. Chem. Phys. 55, No. 3, (1971) 1414-1425.

21. K.C. Russell, Acta Met. 19 (1971) 753-758.

22. K.C. Russell, Acta Met. 26 (1978) 1615-1629.

23. J.L. Katz and H. Wiedersich, J. Nucl. Mat. 46 (1973) 41-45.

24. W.G. Wolfer and M.H. Yoo, ORNL/TM-5398, May 1976.

25. A.D. Brailsford and R. Bullough, J. Nucl. Mat. 69&70 (1978) 434-450.

26. L.K. Mansur, "Void Swelling in Metals and Alloys Under Irradiation: An Assessment of the Theory," Oak Ridge National Laboratory (1978).

27. S.D. Harkness and C.Y Li, Met. Trans. 2 (1971) 1457-1470.

28. A.D. Brailsford and R. Bullough, J. Nucl. Mat. 44 (1972) 121.

29. H. Wiedersich, Rad. Eff. 12 (1972) 111-125.

30. C.A. Parker and K.C. Russell, Scripta Met. 15 (1981) 643-647.

31. B.B. Glasgow and W.G. Wolfer, DAFS Quarterly Progress Report, Feb. 1983, DOE/ER-0046/12, pp. 117-140.

32. J.R. Townsend, J. Nucl. Mat. 108&109 (1982) 544-549.

33. L.K. Mansur and W.A. Coghlan, J. Nucl. Mat. 119 (1983) 1-25.

34. M.W. Guinan and J.H. Kinney, J. Nucl. Mat. 108&109 (1982) 95-103.

35. W.G. Wolfer, presented at the Third Topical Meeting on Fusion Reactor Materials, Albuquerque, NM, Sept. 19-23, 1983, to be published in J. Nucl. Matl.

CHAPTER III

REVIEW OF PREVIOUS EXPERIMENTS

Early experiments attempting to determine the effect of radiation on metals centered on pure materials in hopes of gaining an understanding of basic processes without dealing with complex microstructures or phase changes. Therefore, there exists in the literature a great number of studies on pure metals such as copper, nickel, aluminum, iron, vanadium, etc. The methods of irradiation include fast and thermal neutron, heavy and light ion, and electrons. This chapter consists of three sections with associated tables devoted to the irradiation of pure nickel with ions, electrons and neutrons.

A. Heavy Ion Irradiations of Pure Nickel

Numerous heavy ion irradiations of nickel[1-24,40] have been completed during the past decade. A majority have used nickel ions[1-4,7,8,10-13,16-18,21-24] as the source of damage, while others have used protons,[5,9] helium,[14] selinium,[6,11] carbon,[15,19,20] aluminum[21-23] and copper.[21,22] The effect of interstitial gas atoms on cavity nucleation has been studied using simultaneous helium irradiation,[4,10] helium pre-injection,[4,7,9-11,14-16,18,40] and hydrogen introduced during specimen preparation.[21-23] A summary of the experiments reviewed for this report is given in Table III-1.

One of the interesting recent studies in nickel centers around the effect of non-steady state irradiation conditions. Brimhall et al.[1] conducted a study of the effect of pulsed and steady state

TABLE III-1: HEAVY ION IRRADIATIONS OF HIGH PURITY NICKEL

Nickel Purity	Gas Content (appm)	Ion	Dose Rate $x10^{-3}$ (sec^{-1})	Dose (dpa)	Temp. (°C)	Nv x 10^{20} (m^{-3})	$\bar{d}$ (nm)	Swelling ΔV/V%	Ref.
High	0	5 MeV Ni	5	2	500	4.3-4.8	43-44	1.8-2.1	1
High	0	5 MeV Ni	5	2	500	3.8	43	1.6	1
High	0	5 MeV Ni	5	10	500	1.4-5.5	45-64	1.9-4.8	1
High	0	5 MeV Ni	5	10	500	2.7-5.9	36-60	1.5-3.0	1
High	0	5 MeV Ni	5	12	500	1.7-3.2	46-63	1.7-2.2	1
High	0	5 MeV Ni	5	10	500	2.3-8	45-56	2.1-3.8	1
High	0	5 MeV Ni	5	10	625	0.089-0.091	138-200	1.3-4.2	1
High	0	5 MeV Ni	5	12	625	0.05-0.17	178-210	2.4-5.3	1
High	0	5 MeV Ni	5	10	700	0.05-0.26	170-260	5.1-11	1
High	0	5 MeV Ni	5	12	700	0.03	270	3.3	1
0.99995	0	2.8 MeV Ni	70	13	325	0	0	0	2
0.99995	0	2.8 MeV Ni	70	13	375	0	0	0	2
0.99995	0	2.8 MeV Ni	70	13	425	0	0	0	2
0.99995	0	2.8 MeV Ni	70	13	475	0	0	0	2
0.99995	0	2.8 MeV Ni	70	13	525	76	10	0.48	2
0.99995	0	2.8 MeV Ni	70	13	575	69	13	0.90	2
0.99995	0	2.8 MeV Ni	70	13	625	18	22.5	1.20	2
0.99995	0	2.8 MeV Ni	70	13	675	0.3	72.5	0.62	2
0.99995	0	2.8 MeV Ni	70	13	725	0.14	80	0.40	2

Table III-1. Continued

Nickel Purity	Gas (appm)	Comment	Ion	Dose Rate $x10^{-3}$ (sec^{-1})	Dose (dpa)	Temp. (°C)	Nv x 10^{20} (m^{-3})	$\bar{d}$ (nm)	Swelling ΔV/V%	Ref.
0.99995	0		2.8 MeV Ni	70	4	575	110	7.5	0.28	3
0.99995	0		2.8 MeV Ni	70	13	575	69	13.0	0.90	3
0.99995	0		2.8 MeV Ni	70	40	575	55	15.0	1.23	3
0.99995	0		2.8 MeV Ni	70	130	575	6.6	38.0	2.16	3
0.9999	100	(He)	5 MeV Ni	5	1.0	625	50-90	8.5-12.5	0.3-0.5	4
0.9999	16	(He)	5 MeV Ni	5	0.35	625	3-10	12-24	0.12-0.28	4
0.9999	100	(He)	5 MeV Ni	5	1.0	525	50-90	6.0	0.05-0.1	4
0.9999	16	(He)	5 MeV Ni	5	0.35	525	20	8.0-15.0	0.05-0.4	4
0.9999	6	(He)	5 MeV Ni	5	1.2	575	60	10.0	0.5	4
0.9999	10	(He)	5 MeV Ni	5	1.1	575	2	21.0	0.1	4
0.9999	67	(He)	5 MeV Ni	5	2.0	575	8	19.0	0.3	4
0.999	0		6-11 MeV Se	30	2.0	525	17	8.0	0.1	6
0.999	0		6-11 MeV Se	30	2.3	525	27	12.0	0.24	6
0.999	0		6-11 MeV Se	30	12	525	36	21.0	1.7	6
0.999	0		6-11 MeV Se	30	47	525	40	27.0	4.1	6
0.999	0		6-11 MeV Se	30	95	525	76	22.0	4.2	6
0.999	0		6-11 MeV Se	30	400	525	140	18.0	4.4	6
0.9999	15		5 MeV Ni	20	140	625	19	46.5	12	7
0.9994	0		4 MeV H	0.006	1	450	6	25.0	---	5

Table III-1. Continued

Nickel Purity	Gas Content (appm)	Ion	Dose Rate $x10^{-3}$ (sec^{-1})	Dose (dpa)	Temp. (°C)	Nv x 10^{20} (m^{-3})	$\bar{d}$ (nm)	Swelling ΔV/V%	Ref.
0.999	0	6-11 MeV Se	30	0.47	525	3	9.0	0.0012	6
0.99995	0	5 MeV Ni	10	10	185	0	dense loops		8
0.99995	0	5 MeV Ni	10	10	280	0	aligned loops		8
0.99995	0	5 MeV Ni	10	10	370	0	aligned loops		8
0.99995	0	5 MeV Ni	10	10	435	0	aligned loops		8
0.99997	0.3 (He)	1.4 MeV H	0.2	1	300	5	4.0	0.001	9
0.99997	0.3 (He)	1.4 MeV H	0.2	1	400	85	8.0	0.28	9
0.99997	0.3 (He)	1.4 MeV H	0.2	1	500	90	11.0	0.10	9
0.99997	7 (He)	1.4 MeV H	0.2	1	400	50	6.5	0.10	9
0.99997	28 (He)	1.4 MeV H	0.2	1	400	150	5.5	0.12	9
0.99995	0	4 MeV Ni	3	0.6	500	1.6	19.8	0.065	10
0.99995	0	4 MeV Ni	3	0.6	500	1.9	13.4	0.024	10
0.99995	0	4 MeV Ni	3	1	500	0.2	14.9	0.0032	10
0.99995	20 (He)	4 MeV Ni	3	1	500	27.0	13.7	0.36	10
0.99995	20 (He)	4 MeV Ni	3	1	500	5.0	7.4	0.011	10
0.99995	0	4 MeV Ni	3	0.6	550	3.4	18.1	0.10	10
0.99995	0	4 MeV Ni	3	0.6	550	0.3	25.9	0.033	10
0.99995	0	4 MeV Ni	3	1	550	High Loop Concentration			10
0.99995	0	4 MeV Ni	3	1	550	2.7	30.2	0.33	10

Table III-1. Continued

Nickel Purity	Gas Content (appm)	Ion	Dose Rate $x10^{-3}$ (sec^{-1})	Dose (dpa)	Temp. (°C)	Nv x 10^{20} (m^{-3})	$\bar{d}$ (nm)	Swelling ΔV/V%	Ref.
0.99995	0	4 MeV Ni	3	1	550	High Loop Concentration			10
0.99995	20 (He)	4 MeV Ni	3	1	550	5.5	22.0	0.30	10
0.99995	20 (He)	4 MeV Ni	3	1	550	2.8	26.2	0.26	10
0.99995	20 (He)	4 MeV Ni	3	1	550	9.9	20.4	0.44	10
0.99995	0	4 MeV Ni	3	0.6	600	0.4	46.3	0.22	10
0.99995	0	4 MeV Ni	3	0.6	600	0.8	40.7	0.30	10
0.99995	0	4 MeV Ni	3	0.6	600	0.2	57.6	0.24	10
0.99995	0	4 MeV Ni	3	1	600	2.3	33.8	0.46	10
0.99995	0	4 MeV Ni	3	1	600	3.8	33.2	0.66	10
0.99995	0	4 MeV Ni	3	0.9	600	7.1	22.4	0.42	10
0.99995	0	4 MeV Ni	3	0.9	600	Low Loop Concentration			10
0.99995	0	4 MeV Ni	3	0.9	600	Low Loop Concentration			10
0.99995	20 (He)	4 MeV Ni	3	1	600	2.1	42.1	0.75	10
0.99995	20 (He)	4 MeV Ni	3	1	600	21	15.6	0.42	10
0.99995	0	4 MeV Ni	3	0.6	650	0.16	60.5	0.18	10
0.99995	0	4 MeV Ni	3	0.6	650	0.17	47.2	0.094	10
0.99995	0	4 MeV Ni	3	1	650	0.51	56.7	0.48	10
0.99995	0	4 MeV Ni	3	1	650	0.10	78.1	0.25	10
0.99995	20 (He)	4 MeV Ni	3	1	650	0.64	48.3	0.37	10

Table III-1. Continued

Nickel Purity	Gas Content (appm)	Ion	Dose Rate $x10^{-3}$ (sec^{-1})	Dose (dpa)	Temp. (°C)	Nv x 10^{20} (m^{-3})	$\bar{d}$ (nm)	Swelling ΔV/V%	Ref.
0.99995	20 (He)	4 MeV Ni	3	1	650	Low Loop Concentration			10
0.99995	20 (He)	4 MeV Ni	3	1	650	12	17	0.33	10
0.99995	0	4 MeV Ni	3	0.6	700	0.0089	69	0.02	10
0.99995	0	4 MeV Ni	3	0.6	700	0.011	67	0.018	10
0.99995	20 (He)	4 MeV Ni	3	1	700	Low Loop Concentration			10
0.99995	20 (He)	4 MeV Ni	3	1	700	0.093	82	0.28	10
0.99995	20 (He)	4 MeV Ni	3	1	700	1.5	39	0.47	10
0.99995	3 (He)	5 MeV Ni	20	1	525	11	9.0	0.07	11
0.99995	3 (He)	5 MeV Ni	20	4.4	525	20	15.0	0.19	11
0.99995	3 (He)	5 MeV Ni	20	6.5	525	29	14.5	0.46	11
0.99995	3 (He)	5 MeV Ni	20	10	525	32	15.5	0.61	11
0.99995	3 (He)	5 MeV Ni	20	25	525	35	21.0	1.7	11
0.99995	3 (He)	5 MeV Ni	20	58	525	33	25.0	2.7	11
0.99995	3 (He)	6 MeV Ni	20	67	525	27	30.5	4.0	11
0.99995	3 (He)	5 MeV Ni	20	360	525	42	25.0	3.4	11
0.99995	3 (He)	5 MeV Ni	20	480	525	40	26.0	3.7	11
0.99995	0	6 MeV Ni	20	0.43	525	3.8	13.5	0.048	11
0.99995	0	6 MeV Ni	20	1.3	525	9.9	14.0	0.14	11
0.99995	0	6 MeV Ni	20	6	525	34	14.0	0.49	11

Table III-1. Continued

Nickel Purity	Gas Content (appm)	Ion	Dose Rate $x10^{-3}$ (sec^{-1})	Dose (dpa)	Temp. (°C)	Nv x 10^{20} (m^{-3})	$\bar{d}$ (nm)	Swelling $\Delta V/V\%$	Ref.
0.99995	0	6 MeV Ni	20	44	525	41	26.5	3.95	11
0.99995	0	11 MeV Se	20	0.47	525	3	9.0	0.012	11
0.99995	0	11 MeV Se	20	2	525	17	7.0	0.05	11
0.99995	0	11 MeV Se	20	2.3	525	27	12.0	0.24	11
0.99995	0	8 MeV Se	20	12	525	36	21.0	1.7	11
0.99995	0	8.8 MeV Se	20	47	525	40	27.0	4.1	11
0.99995	0	8.8 MeV Se	20	95	525	76	22.0	4.2	11
0.99995	0	6 MeV Se	20	400	525	140	18.0	4.4	11
0.99995	0	2.8 MeV Ni	0.7	13	300	0	0	0	12
0.99995	0	2.8 MeV Ni	0.7	13	350	0	0	0	12
0.99995	0	2.8 MeV Ni	0.7	13	400	0	0	0	12
0.99995	0	2.8 MeV Ni	0.7	13	425	61	8.0	0.20	12
0.99995	0	2.8 MeV Ni	0.7	13	450	16	20.0	0.73	12
0.99995	0	2.8 MeV Ni	0.7	13	500	7.7	29.0	1.1	12
0.99995	0	2.8 MeV Ni	0.7	13	550	8.3	36.5	2.4	12
0.99995	0	2.8 MeV Ni	0.7	13	550	9.3	30.0	1.6	12
0.99995	0	2.8 MeV Ni	0.7	13	600	0.66	58.5	0.73	12
0.99995	0	2.8 MeV Ni	0.7	13	600	1.3	51.5	0.98	12
0.99995	0	2.8 MeV Ni	70	13	625	0.07	32.0	0.015	12

Table III-1. Continued

Nickel Purity	Gas Content (appm)	Ion	Dose Rate $x10^{-3}$ (sec^{-1})	Dose (dpa)	Temp. (°C)	Nv x 10^{20} (m^{-3})	$\bar{d}$ (nm)	Swelling ΔV/V%	Ref.
0.99995	0	2.8 MeV Ni	70	13	375	0	0	0	12
0.99995	0	2.8 MeV Ni	70	13	425	0	0	0	12
0.99995	0	2.8 MeV Ni	70	13	475	0	0	0	12
0.99995	0	2.8 MeV Ni	70	13	525	76	10.0	0.48	12
0.99995	0	2.8 MeV Ni	70	13	575	69	13.0	0.90	12
0.99995	0	2.8 MeV Ni	70	13	625	18	22.5	1.2	12
0.99995	0	2.8 MeV Ni	70	13	675	0.3	72.5	0.62	12
0.99995	0	2.8 MeV Ni	70	13	725	0.14	80.00	0.40	12
0.99995	0	2.8 MeV Ni	40	0.8	625	10	12.5	0.13	13
0.99995	0	2.8 MeV Ni	40	2.5	625	7.0	23.0	0.5	13
0.99995	0	2.8 MeV Ni	40	8.1	625	18	22.5	1.2	13
0.99995	0	2.8 MeV Ni	40	25	625	2.7	55.0	2.6	13
0.99995	0	2.8 MeV Ni	40	8.1	550	8.3	36.5	2.4	13
0.99995	600 (He)	500 keV He	---	0.04	500	320	2.5	0.04	14
0.99995	3000 (He)	500 keV He	---	0.22	500	760	2.8	0.10	14
0.99995	15000 (He)	500 keV He	---	1.10	500	1750	3.0	0.22	14
0.99995	30000 (He)	500 keV He	---	2.20	500	2990	4.1	1.50	14
High	10 (He)	20 MeV C	---	1	250	18	---	0.2	15
High	10 (He)	20 MeV C	---	10	250	30	---	2.0	15

Table III-1. Continued

Nickel Purity	Gas Content (appm)	Ion	Dose Rate $x10^{-3}$ (sec^{-1})	Dose (dpa)	Temp. (°C)	Nv x 10^{20} (m^{-3})	$\bar{d}$ (nm)	Swelling ΔV/V%	Ref.
0.9999	10 (He)	46.5 MeV Ni	0.33	18	450	120	10	1.2	16
0.9999	10 (He)	46.5 MeV Ni	0.33	18	500	90	11	2.0	16
0.9999	10 (He)	46.5 MeV Ni	0.33	18	550	20	11	0.6	16
0.9999	10 (He)	46.5 MeV Ni	0.33	18	600	15	25	3.1	16
0.9999	10 (He)	46.5 MeV Ni	0.33	18	650	10	35	3.0	16
0.9999	10 (He)	46.5 MeV Ni	6.7	18	450	0	---	0	16
0.9999	10 (He)	46.5 MeV Ni	6.7	18	500	60	11	0.6	16
0.9999	10 (He)	46.5 MeV Ni	6.7	18	550	75	12	2.0	16
0.9999	10 (He)	46.5 MeV Ni	6.7	18	600	70	12	2.5	16
0.9999	10 (He)	46.5 MeV Ni	6.7	18	650	50	12	2.1	16
0.9999	10 (He)	46.5 MeV Ni	6.7	18	700	10	20	1.9	16
0.9999	0	2.8 MeV Ni	70	13	625	5	37.0	1.3	17
0.99995	1 (He)	5 MeV Ni	6	0.06	575	0.07	4.1	0.0025	18
0.99995	2 (He)	5 MeV Ni	6	0.16	575	0.02	9.3	0.008	18
0.99995	8 (He)	5 MeV Ni	6	0.27	575	0.17	8.2	0.054	18
0.99995	32 (He)	5 MeV Ni	6	2.2	575	0.08	18.9	0.32	18
0.99997	0	2.8 MeV Ni	2.5	2	525	8.0	18.0	0.50	19
0.99997	0	2.8 MeV Ni	2.5	5	525	13	26	1.5	19
0.99997	0	2.8 MeV Ni	2.5	10	525	10	30	2.0	19

Table III-1. Continued

Nickel Purity	Gas Content (appm)	Ion	Dose Rate $x10^{-3}$ (sec^{-1})	Dose (dpa)	Temp. (°C)	Nv x 10^{20} (m^{-3})	$\bar{d}$ (nm)	Swelling $\Delta V/V\%$	Ref.
0.99997	0	2.8 MeV Ni	2.5	30	525	15	32	3.5	19
0.99997	0	2.8 MeV Ni	2.5	47	525	10	41	4.6	19
0.99997	0	2.8 MeV Ni	2.5	60	525	4	60	6.0	19
0.99997	0	1 MeV C	2.5	8	475	21	28	2.9	19
0.99997	0	1 MeV C	2.5	8	525	6	52	4.0	19
0.99997	0	1 MeV C	2.5	8	575	3.2	66	3.4	19
0.99997	0	1 MeV C	2.5	8	625	2.0	73	3.1	19
0.99997	0	1 MeV C	2.5	8	700	1.0	90	3.9	19
0.99997	0	1 MeV C	2.5	1	525	12	14	0.3	19
0.99997	0	1 MeV C	2.5	5	525	15	32.5	2.5	19
0.99997	0	1 MeV C	2.5	10	525	12	45	5.3	19
0.99997	0	1 MeV C	2.5	20	525	7	71	12	19
0.99995	0	8.1 MeV Al	0.40	9.5	525	45	10	0.5	20
0.99995	0	8.1 MeV Al	0.4	2	525	15	33	3.2	20
0.99995	0	5 MeV C	0.5	12	525	35	21	2.5	20
0.99995	0	5 MeV C	0.5	6.5	525	45	12	0.5	20
0.99995	0	14 MeV Ni	1.6	15	525	20	30	2.0	20
0.99995	H	19 MeV Cu	1.5	10	525	40	---	---	21
0.99995	H	19 MeV Cu	1.5	5	525	32	---	---	21

Table III-1. Continued

Nickel Purity	Gas Content (appm)	Ion	Dose Rate $x10^{-3}$ (sec^{-1})	Dose (dpa)	Temp. (°C)	Nv x 10^{20} (m^{-3})	$\bar{d}$ (nm)	Swelling ΔV/V%	Ref.
0.99995	H	19 MeV Cu	1.5	3	525	20	---	---	21
0.99995	H	14 MeV Cu	1.5	15	525	15	25	2.5	21
0.99995	H	14 MeV Ni	1.5	15	525	20	30	3.0	21
0.99995	H	19 MeV Cu	1.5	5	525	32	---	---	22
0.99995	0	18 MeV Ni	1.5	4.3	525	0.3	140	4.5	22
0.99995	H	14 MeV Ni	1.5	2	525	45	12	0.5	23
0.99995	H	14 MeV Ni	1.5	5	525	28	15	0.5	23
0.99995	H	14 MeV Ni	1.5	10	525	35	18	1.0	23
0.99995	H	14 MeV Ni	1.5	20	525	40	20	2.0	23
0.99995	H	14 MeV Ni	1.5	40	525	52	22	3.5	23
0.99995	H	14 MeV Ni	1.5	75	525	30	24	3.0	23
0.99995	H	14 MeV Ni	1.5	140	525	25	22	2.0	23
0.99995	0	2.8 MeV Ni	40	8.1	675	23	30.8	4.1	24
0.99995	0	2.8 MeV Ni	40	8.1	625	42	23.7	3.3	24
0.99995	0	2.8 MeV Ni	40	8.1	525	19	61.0	2.7	24
0.9992	15 (He)	4 MeV Ni	6	25	594	28	24	---	40
0.9992	15 (He)	4 MeV Ni	6	25	594	28	24	---	40
0.9992	15 (He)	4 MeV Ni	6	25	594	28	24	---	40
0.99995	0	300 keV Ar	0.8	2.3	500	In-situ TEM Loop Growth			41

Table III-1. Continued

Nickel Purity	Gas Content (appm)	Ion	Dose Rate $x10^{-3}$ (sec^{-1})	Dose (dpa)	Temp. (°C)	Nv x 10^{20} (m^{-3})	$\bar{d}$ (nm)	Swelling ΔV/V%	Ref.
0.99995	0	400 keV Ar	0.86	0.1	400	In-situ TEM Loop Growth			41
Pure	0	80 keV He	In-situ Study		550	1-10 nm Bubbles		0.69	42
Pure	0	80 keV He	In-situ Study		750	1-10 nm Bubbles		7.0	42
0.99995	0	4 MeV Ni	3	1	600	0.12	48.9	0.08	52
0.99995	0	4 MeV Ni	3	50	600	0.53	144	9.0	52
0.99995	20	4 MeV Ni	3	1	600	2.5	34.7	0.55	52
0.99995	1000	4 MeV Ni	3	50	600	21	42.6	9.4	52
0.99995	20 p	4 MeV Ni	3	1	600	52	12.3	0.51	52
0.99995	1000 p	4 MeV Ni	3	50	600	100	9.2	0.4	52

p = preimplanted He

irradiation on cavity formation in pure nickel with no injected gas content. Brimhall has noted that samples subjected to a pulsed irradiation environment forms a pre-damage microstructure which contained a lower density of larger voids and produced swelling which was an order of magnitude larger than comparable steady state irradiations.

Sprague et al.[2,3,13] completed a temperature scan of void formation in nickel irradiated with 2.8 MeV Ni ions. Sprague noted a swelling peak at 625°C which is about half the melting temperature (0.52 T_m). Subsequent work by Sprague[13] to high doses (25 dpa) continued to show this peak in the swelling behavior versus temperature.

Brimhall et al.[4,8,18] has also reported results from other nickel irradiations. Early work completed by Brimhall indicated dense loop formation with loops becoming aligned at higher irradiation temperatures and doses of 10 dpa. More recent work investigated the effect of interstitial helium atoms on cavity formation. The comparison between pre-injected and simultaneously injected helium atoms during heavy ion irradiation with 5 MeV nickel ions indicates a greater swelling for pre-injected specimens over those which were simultaneously injected for similar doses. This is due to nucleation of cavity embryos with the pre-injection which allows growth to begin immediately upon heavy ion irradiation.

Kulcinski et al.[6,11] studied radiation damage produced in nickel with Se ion irradiations to very high doses (400-480 dpa) at a

high dose rate (3 x 10^{-2} dpa/sec) and a temperature of 525°C. Extremely high swelling (~ 4%) was observed in these irradiated samples. A FCC void lattice structure was noted in samples irradiated at 525°C with 6 MeV Se ions and with 6 MeV Ni ions to doses greater than 100 dpa.

The work of Whitley et al.[20-23] introduced a unique aspect to the study of radiation damage in metals. The cross section technique for TEM sample preparation used by Whitley, greatly enhanced the information which may be obtained from one sample. The irradiated specimen is studied in a plane parallel to the incident beam direction allowing the dose and dose rate dependencies of the microstructure formation to be evaluated. Whitley also studied the effect of irradiating ion (C, Al, Cu, Ni) and found little correlation between ion species and damage microstructure. The effect of interstitial hydrogen atoms is also addressed by Whitley. In samples in which hydrogen had been introduced during preparation, Whitley found copious void growth. While in samples which were thoroughly outgassed, the void formation was notably less.

The depth dependent microstructure in helium preimplanted/coimplanted nickel under self-ion irradiation has recently been studied by Farrell et al.[52] utilizing a cross-section technique similar to that employed by this study. The results of the preimplantation study show swelling suppression for cold injections. All helium implanted samples showed pronounced enhancement of cavity nucleation and decreases in cavity growth when compared to self-ion irradiated

nickel samples with no helium. The ion energies used in this study produce a range of helium and injected self-interstitial nickel ions which are approximately the same. This may pose problems when attempting to fully understand nucleation of cavities with respect to helium concentration and injected interstitial effects. This is further discussed in Chapter VI of this report.

It should be noted at this time that all of the studies of ion bombardment mentioned above, except those of Whitley, Fenske et al. and Farrell et al., were completed using standard backthinning techniques and observing ion damage microstructure produced at the damage peak. These studies, especially those completed in the temperature range from 400°C to 500°C could be influenced by the effect of injected interstitials on the suppression of nucleation. Since this study as well as those of Whitley, Fenske et al. and Farrell et al., used transverse sectioning techniques to study the ion damage in cross-section, the effect of injected interstitials should be addressed, as in Chapter VI of this study.

B. HVEM Studies in Pure Nickel

The stability of voids growing in a pure nickel sample during electron irradiation appears to depend upon the proximity of a local perturbation in the microstructure such as a dislocation. Studies by Norris[64-67] indicate that voids grew only near dislocations in nickel. Norris noted that should a dislocation climb away from a growing void, the void would stop growing and eventually begin shrinking. This is an indication that in an otherwise perfect

crystal, with an equal supersaturation of vacancies and interstitials, a void will preferentially attract interstitials. Norris also stated that should a crystal contain both defect types, voids and dislocations, the dislocation will have the stronger bias for interstitials. Urban[68,69] found that vacancy loops grow in the presence of straight edge dislocations which is another confirmation of the stronger bias of dislocations for interstitials. Harbottle[70] found that voids could only grow in the presence of a dislocation density of 10^9 cm^{-2}. The conclusion drawn from these experiments is that a dislocation has a stronger attraction for interstitials than a void and acts as the biased sink which facilitates void growth.

Ishino et al.,[41] and Stattler and Jesser[42] each recently completed studies of microstructural evolution in nickel utilizing in-situ irradiation facilities. Ishino studied the evolution of dislocation loops produced by irradiating nickel with 300-400 keV Ar ions and recording video tape images of the microstructure from the viewing screen of a 200 kV electron microscope. Ishino also studied metastable loop formation and dissolution and the effects of temperature on defect free zone formation near grain boundaries.

Stattler and Jesser[42] used a similar in-situ facility to observe helium bubble growth and dissolution. They irradiated nickel films with 80 keV helium ions producing bubbles of 1-10 nm in diameter. They noted differences in the variation of bubble diameter with respect to annealing temperature and the proximity of grain bound-

aries. They also observed an Ostwald ripening in bubbles produced by high temperature irradiation with a lower temperature anneal.

HVEM studies in general are not of great value when attempting to simulate displacement cascade events since only a very few point defects are produced per incident particle. These studies are also completed using very thin foils (~ 100-150 nm) which introduces the effect of the surface as a sink for point defects. However, to obtain allowing a real time evaluation of the damage produced, in-situ studies have the potential to greatly enhance the understanding of the dynamics of nucleation and the effects of gases and impurities on cavity formation.

C. Neutron Irradiations of Pure Nickel

Many of the early neutron irradiations of nickel were completed by Brimhall et al.[25-30] shortly after the first observation of voids in stainless steel. Brimhall[27] was the first to observe voids in nickel. Following this observation, numerous other neutron irradiation investigations of nickel were performed.[31-40] The results of these experiments are summarized in Table III-2. However, caution should be exercised in the comparison of these irradiations since the accepted means of reporting the amount of irradiation each sample encounters is the neutron fluence and not the number of displacements per atom. This may lead to a discrepancy in results if the energy spectrum of the neutron fluences to which identical specimens are exposed is not the same. Since the displacement cross

TABLE III-2. NEUTRON IRRADIATED NICKEL

Nickel Purity	Fluence (cm^{-2}) E > 0.1 MeV	Temp. (°C)	Nv x 10^{20} (m^{-3})	d (nm)	ΔV/V %	Comments	Ref.
0.99997	4 x 10^{19}	50	0	0	0		25
0.99997	1.2 x 10^{20}	260	200	6	0.21		25
0.99997	5.7 x 10^{19}	380	40	8.3	0.11		25
0.99997	5.7 x 10^{19}	500	8	16.5	0.16		25
0.99997	6.2 x 10^{19}	575	2.5	24.5	0.16		25
0.99997	5 x 10^{19}	380	40	8.3	0.11		26
0.99997	1.2 x 10^{20}	260	400	5.5	0.30		26
0.99997	5 x 10^{19}	380	40	10	0.20		27
0.99997	4 x 10^{19}	425	20	10	0.10		27
0.99997	5.2 x 10^{19}	640	0.8	27	0.07		28
0.99997	5.2 x 10^{19}	750	0.001	40	0.001		28
0.9999	5.5 x 10^{18}	285	0.7	5	0.00043		29
0.9999	1.3 x 10^{19}	285	1.5	7	0.0025		29
0.9999	2.4 x 10^{19}	285	3.6	10.5	0.2		29
0.9999	2.5 x 10^{19}	350	1.2	21	0.06	Nickel Purity Variation	30
0.99998	2.5 x 10^{19}	400	0.5	28	0.05		30
0.99998	2.5 x 10^{19}	450	0.4	34	0.07		30
0.99997	2.5 x 10^{19}	350	16	9.7	0.06	Nickel Purity Variation	30
0.99997	2.5 x 10^{19}	400	9	12	0.07		30

Table III-2. Continued

Nickel Purity	Fluence (cm^{-2}) E > 0.1 MeV	Temp. (°C)	Nv x 10^{20} (m^{-3})	d (nm)	ΔV/V %	Comments	Ref.
0.99997	2.5 x 10^{19}	450	5	13.2	0.06		30
0.9999	2.5 x 10^{19}	350	3.6	15.5	0.06	Nickel Purity Variation	30
0.9999	2.5 x 10^{19}	400	1.2	19.2	0.04		30
0.9999	2.5 x 10^{19}	450	0.9	25.4	0.06		30
0.99998	1.4 x 10^{20}	385	2.9	12.6	0.05	Cubic Voids	31
0.99998	1.4 x 10^{20}	410	3.2	13.3	0.07	Cubic Voids	31
0.99998	1.4 x 10^{20}	440	2	15.1	0.06		31
0.99998	1.4 x 10^{20}	470	3.2	16	0.08	Octahedral Voids	31
0.99998	1.4 x 10^{20}	525	2.4	---	---	Elongated Voids	31
0.99998	1.4 x 10^{20}	370	1.2	6	---	Cubic Voids	31
0.99998	1.4 x 10^{20}	370	2.9	10.3	---	Cubic Voids	31
0.99998	1.4 x 10^{20}	470	1	30	---	Cubic Voids	31
0.9995	2.3 x 10^{20}	300	40	9	0.18		32
0.9995	2.3 x 10^{20}	400	8.5	16	0.20		32
0.9995	2.3 x 10^{20}	500	5.8	20	0.23		32
0.9995	2.3 x 10^{20}	600	5	27	0.07		32
0.99995	5.4 x 10^{20}	300	11	9.3	0.044		33
0.99995	5.4 x 10^{20}	350	12	18.6	0.42		33
0.99995	6.3 x 10^{20}	400	3.4	29.3	0.44		33

Table III-2. Continued

Nickel Purity	Fluence (cm^{-2}) E > 0.1 MeV	Temp. (°C)	Nv x 10^{20} (m^{-3})	d (nm)	ΔV/V %	Comments	Ref.
0.99995	6.2 x 10^{20}	450	7.8	20.3	0.34		33
0.99995	6.2 x 10^{20}	500	2	26.5	0.197		33
0.99995	6.95 x 10^{21}	550	0.78	23.7	0.056		33
0.99995	6.9 x 10^{20}	750	0.044	32.2	0.007		33
0.99995	1.04 x 10^{21}	850	0.022	42.5	0.0086		33
0.9999	4 x 10^{18}	500	0.20	14.6	0.006	4 wt ppm Carbon	34
0.9999	4 x 10^{18}	500	0.15	14.8	0.005	16 wt ppm Carbon	34
0.9999	4 x 10^{18}	500	0.1	15.7	0.004	27 wt ppm Carbon	34
0.9999	4 x 10^{18}	500	0.01	20.0	0.001	84 wt ppm Carbon	34
0.9999	4 x 10^{18}	500	No Voids	---	---	600 wt ppm Carbon	34
0.9999	5.3 x 10^{19}	500	2.5	19.8	0.19	4 wt ppm Carbon	34
0.9999	5.3 x 10^{19}	500	1.8	20.5	0.15	16 wt ppm Carbon	34
0.9999	5.3 x 10^{19}	500	1.3	21.4	0.13	27 wt ppm Carbon	34
0.9999	5.3 x 10^{19}	500	0.6	24.7	0.09	84 wt ppm Carbon	34
0.9999	5.3 x 10^{19}	500	No Voids	---	---	600 wt ppm Carbon	34
0.99995	2 x 10^{17}	400	0	---	0		35
0.99995	5 x 10^{17}	400	0.1	---	0.0001	Cubic Voids	35
0.99995	1 x 10^{18}	400	0.2	---	0.001	Cubic Voids	35
0.99995	5 x 10^{18}	400	1.1	---	0.004		35

Table III-2. Continued

Nickel Purity	Fluence (cm^{-2}) E > 0.1 MeV	Temp. (°C)	Nv x 10^{20} (m^{-3})	d (nm)	ΔV/V %	Comments	Ref.
0.99995	1 x 10^{19}	400	2	---	0.02	Octahedral Voids	35
0.99995	1 x 10^{20}	400	20	---	0.3	Octahedral Voids	35
0.9998	1.4 x 10^{20}	385	---	11.0	---		36
0.9998	1 x 10^{21}	425	---	---	0.25	20% CW No Effect	37
0.9998	3.5 x 10^{21}	425	---	---	0.85	20% CW No Effect	37
0.996	1 x 10^{21}	425	---	---	0	20% CW No Effect	37
0.996	3.5 x 10^{21}	425	---	---	0.1	20% CW No Effect	37
0.99995	1.8 x 10^{20}	455	3.4	37.5	1.4		38
0.99995	3.8 x 10^{20}	565	---	---	2.0		39
0.99995	3.7 x 10^{20}	600	---	---	2.0		39
Pure	5.5 x 10^{21}	460	---	---	1.58		43
Pure	1.1 x 10^{22}	460	---	---	2.05		43
Pure	4.3 x 10^{22}	460	---	---	2.73		43
Pure	4.3 x 10^{22}	500	---	---	2.50		43
Pure	4.3 x 10^{22}	600	---	---	0.64		43

section is highly energy dependent, a variation in energy spectrum may lead to completely different results for the same fluence.

It must also be noted that knowledge of the neutron energy spectrum is essential in determining the transmutation rates for a material. The transmutation of $^{58}Ni(n,\gamma)^{59}Ni$ followed by a (n,α) reaction can introduce helium into a nickel specimen which is subjected to a thermal neutron flux since the transmutation reaction has a high thermal cross section. This interstitial helium may act to stabilize void embroyos or even form helium bubbles, greatly affecting the swelling behavior.

As noted in Table III-2, voids have been noted to form in neutron irradiated nickel over a wide temperature range (260°C to 850°C) when irradiated to a fluence of about 10^{18} n/cm^2 or greater. The shapes of the voids varied from cubic[31] at relatively low temperatures to elongated or octahedral voids[31] at high temperatures. The addition of carbon impurities (4-600 wppm) by Sorensen[34] appears to have the effect of decreasing the amount of swelling by an order of magnitude. This is most likely due to the trapping of point defects or disruption of the displacement cascade which enhances recombination as outlined in Chapter II of this report.

Differing results were reported by Adda[32] and Holmes[37] pertaining to the effect of cold work or pre-irradiation dislocation structure on swelling. Adda reported an increase in swelling with cold work, while Holmes noted no effect. Since these were early

studies with relatively low swelling rates it is easy to understand how results may be misinterpreted. Current models indicate that cold working provides an incubation period during which there is little swelling. When the incubation dose is reached swelling begins and increases linearly at a rate of 1% per dpa.[51]

References for Chapter III

1. J.L. Brimhall, L.A. Charlot and E.P. Simonen, J. Nucl. Mat. 103&104 (1981) 1147-1150.

2. J.A. Sprague, J.E. Westmoreland, F.A. Smidt, Jr., and P.R. Malmberg, J. Nucl. Mat. 54 (1974) 286-298.

3. J.A. Sprague, J.E. Westmoreland, F.A. Smidt, Jr., and P.R. Malmberg, Properties of Reactor Structural Alloys After Neutron or Particle Irradiation, ASTM STP 570 (1975) pp. 505-524.

4. J.L. Brimhall and E.P. Simonen, J. Nucl. Mat. 68 (1977) 235-243.

5. D.J. Mazey and J.A. Hudson, J. Nucl. Mat. 37 (1970) 13-17.

6. G.L. Kulcinski, J.L. Brimhall, and H.E. Kissinger, J. Nucl. Mat. 40 (1971) 166-174.

7. W.G. Johnston, J.H. Rosolowski, A.M. Turkalo, and L. Lauritzen, J. Nucl. Mat. 54 (1974) 24-40.

8. J.L. Brimhall, BNWL-1839, UC-25, July 1974, USAEC Report.

9. H.H. Neely and K. Herschbach, Rad. Effects 7 (1971) 187-194.

10. N.H. Packan, K. Farrell, and J.O. Steigler, J. Nucl. Mat. 78 (1978) 143-155.

11. G.L. Kulcinski, J. Brimhall, and H. Kissinger, Int. Conf. on Radiation Induced Voids in Metals, ed. Corbett and Ianniello, Albany, NY, 1971, CONF-710601, p. 449 (1972).

12. J.E. Westmoreland, J.A. Sprague, F.A. Smidt, and P.R. Malmberg, Rad. Effects 26 (1975) 1-16.

13. J.A. Sprague, F.A. Smidt, Jr., J.E. Westmoreland, and P.R. Malmberg, Proceedings of Symposium on Physics of Irradiation-Produced Voids, Harwell, England, 9-11 Sept. 1974, AERE-R-7934, p. 263 (1975).

14. G. Fenske, S.K. Das, M. Kaminsky, and G.H. Miley, J. Nucl. Mat. 85&86, (1979) 707-711.

15. J.A. Hudson, D.J. Mazey, and R.S. Nelson, BNES Conf. on Voids Formed by Irradiation of Reactor Materials, ed. Pugh, Loretto and Norris, Reading, U.K., 1971, p. 213 (1971).

16. F. Menzinger and F. Sacchetti, J. Nucl. Mat. 57 (1975) 193-197.

17. F.A. Smidt, Jr., and J.A. Sprague, NRL Memorandum Report 2998, Progress Report May-October 1974, p. 39 (1975).

18. J.L. Brimhall and E.P. Simonen, BNWL-01939, UC-20, p. 24 (April 1976).

19. T.D. Ryan, Ph.D. Thesis, University of Michigan, 1975.

20. J.B. Whitley, G.L. Kulcinski, H.V. Smith, and P. Wilkes, Effects of Radiation on Structural Materials, ASTM STP 683, J.A. Sprague and D. Kramer, eds., ASTM (1979) pp. 125-142.

21. J.B. Whitley, G.L. Kulcinski, P. Wilkes, and H.V. Smith, Jr., J. Nucl. Mat. 79 (1979) 159-169.

22. J.B. Whitley, G.L. Kulcinski, P. Wilkes, and J.H. Billen, J. Nucl. Mat. 85&86 (1979) 701-706.

23. J.B. Whitley, Ph.D. Thesis, University of Wisconsin-Madison, August 1978.

24. K.B. Roarty, J.A. Sprague, R.A. Johnson, and F.A. Smidt, Jr., J. Nucl. Mat. 97 (1981) 67-78.

25. J.L. Brimhall and B. Mastel, J. Nucl. Mat. 33 (1969) 186.

26. J.L. Brimhall and B. Mastel, J. Nucl. Mat. 29 (1969) 123.

27. J.L. Brimhall and B. Mastel, J. Nucl. Mat. 28 (1968) 115.

28. J.L. Brimhall and B. Mastel, Scripta Met. 4 (1970) 51.

29. J.L. Brimhall and H.E. Kissinger, Rad. Eff. 15 (1972) 259.

30. J.L. Brimhall, H.E. Kissinger, and G.L. Kulcinski, Radiation-Induced Voids in Metals, ed. Corbett and Ianniello, Albany, NY, 1971, CONF-710601 p. 338.

31. J.O. Steigler and E.E. Bloom, Rad Eff. 8 (1971) 33.

32. Y. Adda, Radiation-Induced Voids in Metals, ed. Corbett and Ianniello, Albany, NY, 1971, CONF-710601 p. 338.

33. N.H. Packan, K. Farrell, and J.O. Steigler, J. Nucl. Mat. 78 (1978) 143-155.

34. S.M. Sorenson and C.W. Chen, Fundamental Aspects of Radiation Damage in Metals, Gatlinburg, TN, (1975) CONF-751006 p. 1213-1220.

35. J.E. Harbottle and S.M. Dickerson, J. Nucl. Mat. 44 (1972) 313-317.

36. E.E. Bloom and J.O. Steigler, Am. Nucl. Soc. Trans. 12 (1969) 116.

37. J.J. Holmes, Am. Nucl. Soc. Trans. 12 (1969) 117.

38. F.A. Smidt, J.A. Reed, and J.A. Sprague, NRL Memorandum Report No. 3588, Sept. 1977.

39. C. Brown, Proceedings of Symposium on Physics of Irradiation Produced Voids, Harwell, England, Sept. 9-11, 1974, AERE-R-7934, p. 90 (1975).

40. C.W. Chen and R.W. Buttry, Rad. Eff. 56 (1981) 210-228.

41. S. Ishino, K. Fukuya, T. Muroga, N. Sekimura and H. Kawanishi, Presented at the Third Topical Meeting on Fusion Reactor Materials, Albuquerque, NM, Sept. 19-23, 1983, to be published in J. Nucl. Mat.

42. M.L. Stattler and W.A. Jesser, Presented at the Third Topical Meeting on Fusion Reactor Materials, Albuquerque, NM, Sept. 19-23, 1983, to be published in J. Nucl. Mat.

43. G. Silvestre, A. Silvent, C. Regnard, and G. Sainfort, J. Nucl. Mat. 57 (1975) 125-135.

44. D.I.R. Norris, Phil. Mag. 22 (1970) 1273.

45. D.I.R. Norris, Nature 227 (1970) 830.

46. D.I.R. Norris, Phil. Mag. 23 (1971) 135.

47. D.I.R. Norris, J. Nucl. Mat. 40 (1971) 66.

48. K. Urban, Phys. Stat. Sol. (a) 3 (1970) 167.

49. K. Urban and M. Willkens, Phys. Stat. Sol. (a) 6 (1971) 173.

50. J.E. Harbottle, Phil. Mag. 27 (1973) 147.

51. F.A. Garner, J. Nucl. Matl. 117 (1983) 177-197.

52. K. Farrell, N.H. Packan and J.T. Houston, Rad. Effects 62 (1982) 39-52.

CHAPTER IV

EXPERIMENTAL FACILITIES AND TECHNIQUES

A. Heavy Ion Irradiation Facility

The heavy ion irradiations in this study were carried out using 14 MeV nickel ions in the University of Wisconsin Heavy Ion Irradiation Facility. This facility, which has been successfully employed for several previous irradiation-effects studies,[1-6] is shown schematically in Fig. IV-1 and is described in detail elsewhere.[7] The facility consists of a tandem electrostatic accelerator (High Voltage Engineering Corporation, Model EN) with associated ion source, beam handling components, and target chamber.

A.1. The EN Tandem Accelerator and SNICS Source

The production of intense beams of heavy ions with a tandem accelerator requires an intense and reliable source of negative ions which are injected into the low-energy end of the accelerator. This facility uses a SNICS type negative ion source developed by Billen and Richards[8-10] to produce beams of Ni^- ions. The basic components of the source include a negatively biased cylindrical cathode (nickel), a helical tungsten ionizing filament, which is co-axial to the cathode, and a cesium reservoir. Cesium atoms are surface ionized on the hot tungsten filament and bombard the surface of the cathode sputtering nickel ions. Negative Ni^- ions form due to charge exchange with Cs atoms and are extracted through an exit aperture with energy equal to the sputter cathode potential (1.2 kV). These negative nickel ions then pass through a selecting magnet, are

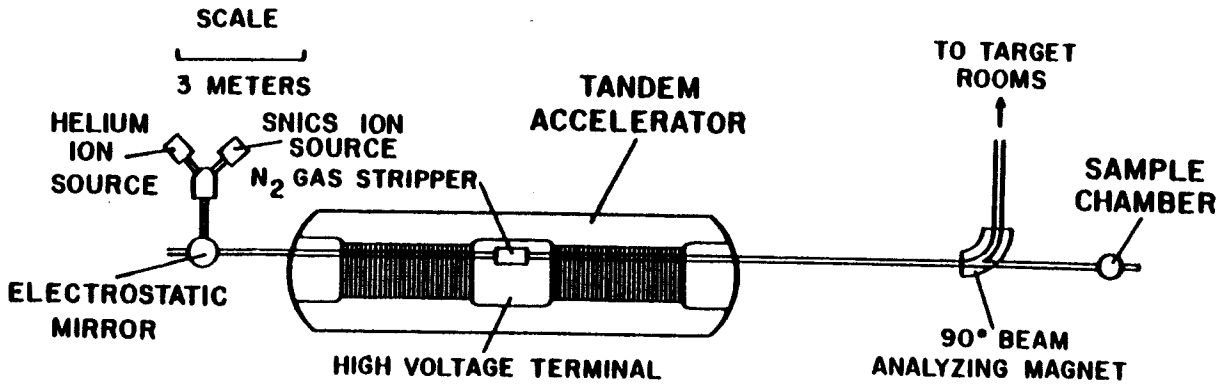

Fig. IV-1. Schematic of the University of Wisconsin Tandem Accelerator Facility.

deflected 90° by an electrostatic mirror, are focussed by a quadrupole triplet, and injected into the accelerator.

The high positive potential V of the high voltage terminal accelerates the negative ions. Collisions with N_2 gas molecules in the gas stripper, located within the high voltage terminal, convert the energetic negative ions into positive ions of charge nq, where n is an integer and q is the electronic charge. These positive particles are then accelerated through the high energy end of the tandem accelerator. Due to the highly random nature of the charged particle-gas interaction in the stripping process, the beam of positive ions exiting the accelerator has a mixture of charge states (i.e., several values of n). The energy acquired by a given charge state emerging from the accelerator is given by

$$E = qV(1 + n) \ . \qquad \text{(IV-1)}$$

The charge state selected for use in this study is the Ni^{3+} charge state (n = 3). With the dome potential of 3.5 MV the nickel ions obtain an energy of 14 MeV by passing through the accelerator. Charge state selection is accomplished using a quadrupole lens situated just outside the high energy end of the accelerator.

A.2. The Heavy Ion Target Chamber

The Heavy Ion Target Chamber and associated vacuum system, which were originally designed and built by Smith and Lott,[3,7] are shown in Fig. IV-2. The target section lies approximately 1/2° off the

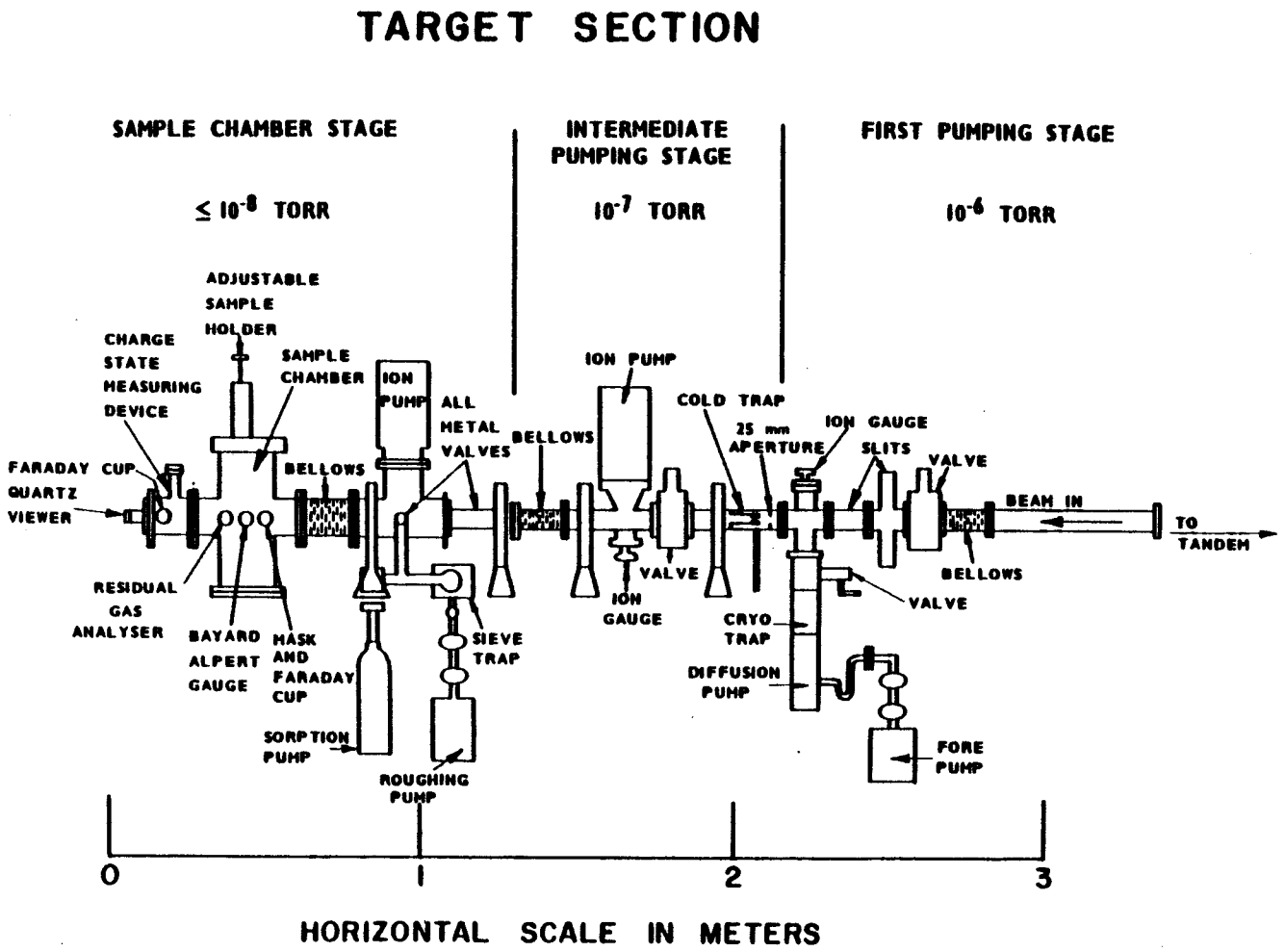

Fig. IV-2. Schematic of Heavy Ion Target Chamber showing the vacuum equipment associated with various pumping stages.

axis of the tandem accelerator to prevent low Z ions and neutral atoms from striking the target. Deflection of the heavy ion beam into the target section is accomplished by using the large analyzing magnet. Pumping for the target section is provided by a three-stage vacuum system. The first pumping stage incorporates a 200 ℓ/sec diffusion pump and typically operates in the 10^{-4} Pa (10^{-6} torr) range. The intermediate pumping stage, capable of achieving 10^{-5} Pa (10^{-7} torr), utilizes a 400 ℓ/sec titanium sublimator pump. The sample chamber stage is capable of reaching the 10^{-7} Pa (10^{-9} torr) region and is pumped by a large orbitron pump. The sample chamber is equipped with a Varian Model VGA-100 residual gas analyzer to allow the composition of residual gases in the vacuum system to be obtained.

Beam diagnostic devices mounted on the target section include Faraday cups and a gold foil with associated solid state detector. The Faraday cups are located at the entrance to the first pumping stage, directly before the specimen, and directly behind the charge state measuring device. The cups are called the entrance cup, mask cup, and exit cup, respectively. Mounted in conjunction with the mask cup is a 0.003 m (3 mm) mask aperture to explicitly define the beam striking the sample during irradiation and prevent incorrect beam current readings. During irradiation beam currents are typically 100 to 300 nA. The gold foil is inserted into the beam path scattering the charged particles 90° from the beam axis into a solid state detector to allow charge state analysis. The energy of the

particles is measured and converted into the initial particle energy using the Rutherford scattering formula. Energy spectra produced by this method show that with proper lens and magnet settings, over 95% of the total beam consists of Ni^{+3} ions. The remaining 5% of the beam consists of Ni^{+} ions which will strike the sample with an energy of 7 MeV. These ions will produce damage in a region closer to the surface of the sample and will result in a slight overestimation of the total damage produced.

The specimen holder assembly, described in great detail elsewhere,[6] consists of a carousel with eight individual sample holders. The carousel arrangement allows individual heating of samples during irradiation by thermal radiation from ohmically heated tantalum sheets. The specimen is mounted on the specimen holder with a chromel-alumel thermocouple in thermal contact with the specimen to allow constant temperature monitoring during irradiation. The range of operating temperatures for this sample holder-heater assembly is approximately 200-800°C.

B. 700 kV Accelerator Facility

The hydrogen and helium pre-injections were completed using the 700 kV Accelerator Facility shown in Fig. IV-3. This facility consists of a 700 KV electrostatic accelerator, beam focussing and analyzing equipment, vacuum system and a specimen holder-heater. A schematic of the accelerator facility, shown in Fig. IV-4, indicates the associated pumping and beam handling components of the system.

700 kV ACCELERATOR FACILITY

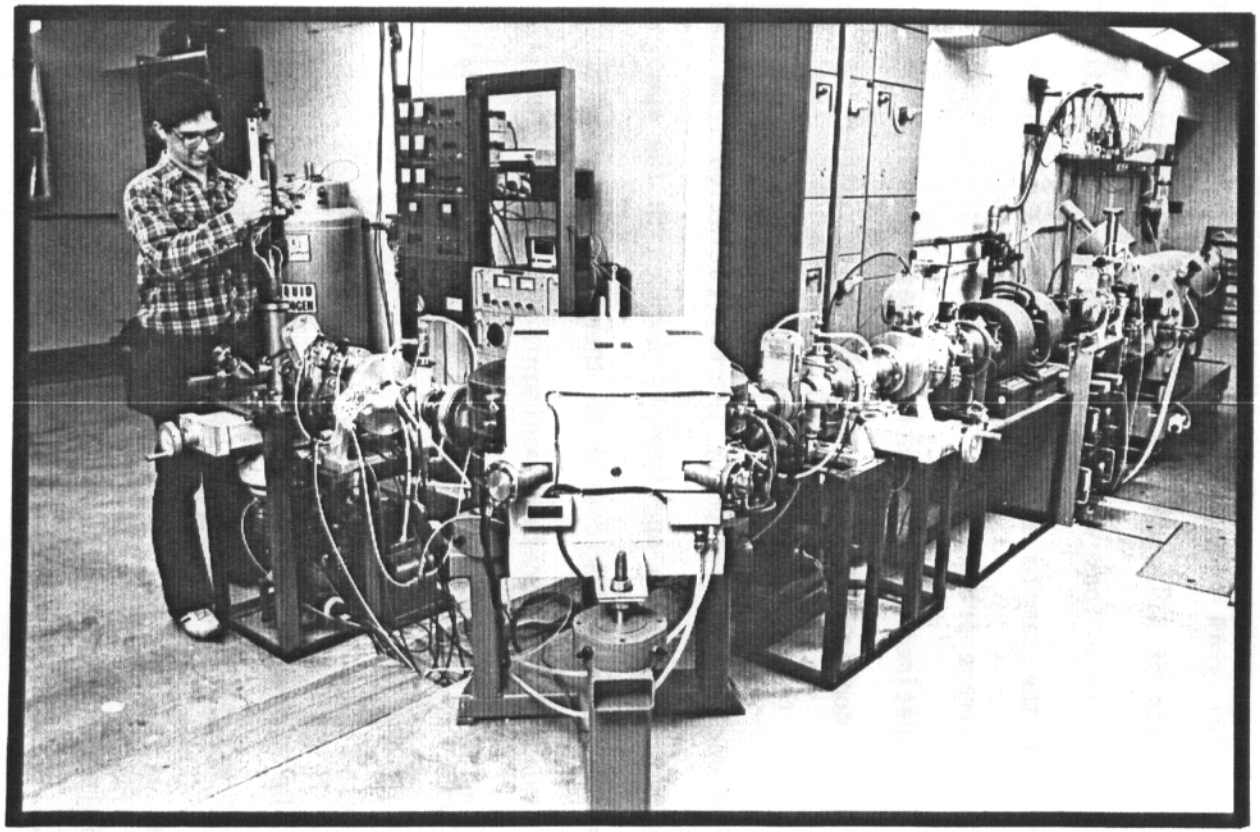

FIG. IV-3. 700 kV ACCELERATOR FACILITY CAPABLE OF PRODUCING UP TO 100 μA BEAMS OF He^+ AND H_3^+. NOTE STANDARD 1.78 M GRADUATE STUDENT FOR SCALE.

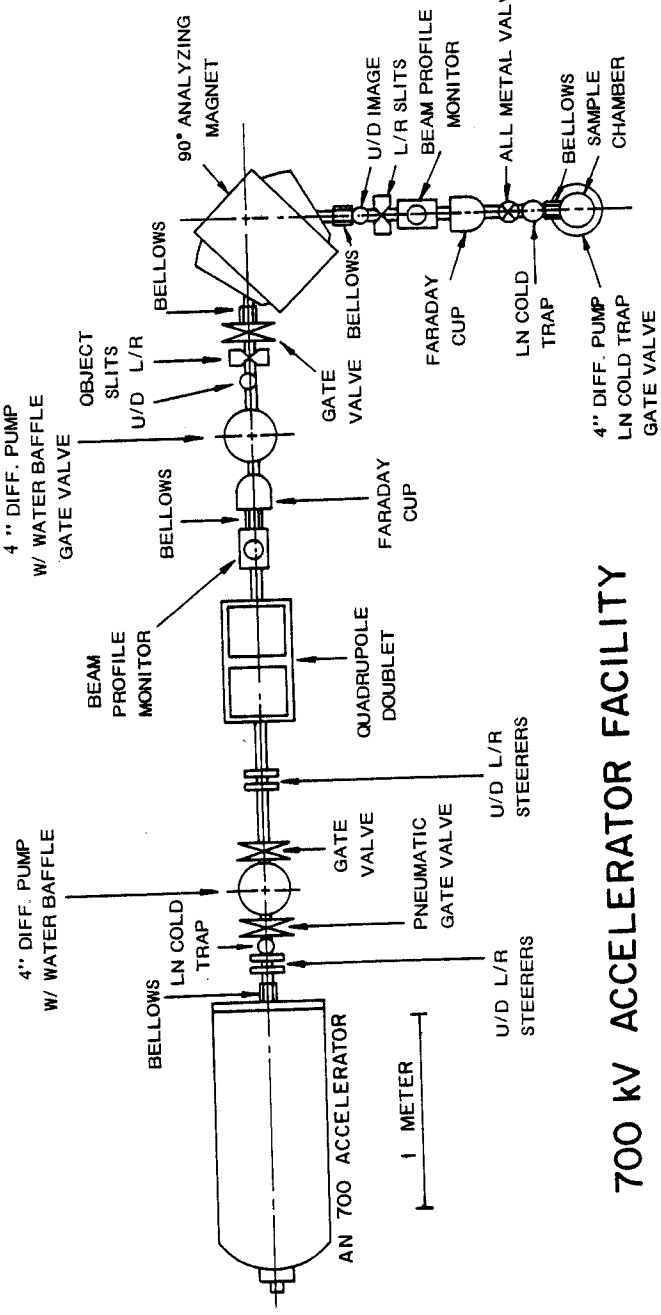

Fig. IV-4. Schematic of the 700 kV Accelerator Facility showing beam handling and vacuum components.

B.1. AN-700 Accelerator

The AN-700 accelerator manufactured by High Voltage Engineering Corporation operates at an accelerating potential ranging from 200 to 700 kilovolts. The accelerator column has an insulating length of 0.38 m (15 in) consisting of equipotential planes (electrically insulated from each other), voltage dividing resistors, conducting bars for maintaining control of voltage gradients across the column, and the charging belt. The high voltage terminal is an aluminum plate 0.38 m (15 in) in diameter. Mounted on the high voltage terminal are a permanent-magnet alternator pulley assembly, a belt charge collector screen, a radio frequency oscillator and power supplies for operating an r.f. source, two source gas supplies (H and He) and two remotely controlled gas leaks.

The two gas leaks consist of a palladium leak used to control the flow of hydrogen from the supply cylinder to the ion source and a thermo-mechanical leak to control the flow of helium. The palladium leak operates when power supplied to a heater warms the palladium making passage of hydrogen through the leak possible. Normal gas flow, under standard r.f. source operating conditions, is from 5 to 10 cc per hour. The thermo-mechanical leak, which operates on the principle of the differential expansion of elements to control the flow of gas with a ball valve, is used to regulate the flow of helium to the r.f. source.

The accelerator pressure vessel is a steel tank 0.55 meters (24 inches) in diameter and 1.6 meters (5.25 ft) long. The vessel is

pressurized to 345 kPa (50 psig) with pure sulfur hexaflouride (SF_6) as an insulating gas. Mounted on the tank are a generating voltmeter, a capacitive pickup assembly, and a motor-driven corona control assembly. Stabilization of the terminal voltage is achieved using a differential amplifier circuit. This system of electronics compares the current ratio of the left-right image slits and adjusts the grid bias of the voltage regulating tube on the corona assembly. This varies the amount of current passing through the corona points and hence stabilizes the terminal voltage. Measurements of voltage variation indicate control to within 1 kV at a terminal voltage of 700 kV.

The design and installation of the AN 700 light ion accelerator was a complicated and exacting process requiring that considerable time and effort be spent on the evaluation of equipment performance. The AN 700 electrostatic accelerator was delivered with no technical data pertaining to the phase space characteristics of the beams produced. The initial tests performed on the machine, including the acceptance tests, dealt mainly with the machine's accelerating potential, source operation and the magnitude of the beam currents produced. The machine has operated satisfactorily at 750 kV which is about 7% above the rated potential. The maximum beam currents produced are 110 μA of He^+ and 115 μA H^+ on a fully suppressed water-cooled target.

The beam currents and accelerating voltage are still not sufficient information to fully describe the beam characteristics. The

emittance of the beam must be known for transport calculations through beam handling components to be completed. The emittance is merely a measure of the position of a particle from the central axis of the beam tube and the angle the particle trajectory makes with the central axis. The units of emittance are: π mm mrad $MeV^{1/2}$. Actual emittance plots have elliptical contours, the shape of which indicate the divergent or convergent nature of the beam. An emittance measuring instrument designed and constructed by J.H. Billen,[11] was used to measure the phase space characteristics of the beams produced by the AN 700. A summary of the measurements is presented in Table IV-1. The smaller the emittance for the 90% contour, the easier the beam focusing and the greater the amount a beam transported to the sample. The measurements indicate that the emittance for the 90%

TABLE IV-1. SUMMARY OF AN 700 ACCELERATOR EMITTANCE CHARACTERISTICS

Dome Voltage (keV)	Ion	Beam Current (μA)	Emittance (90% Contour) (π mm mrad $MeV^{1/2}$)
700	H^+	5	2.62
500	H^+	4	2.81
200	H^+	4	6.32
700	He^+	5	3.92
500	He^+	8	4.19

contour decreases as the accelerating potential increases for both H^+ and He^+ beams. This is understandable since at higher accelerating voltages, space-charge problems are reduced.

B.2. Vacuum Equipment

Pumping for the accelerator system is provided by three Varian Model VHS-4 diffusion pumps. These pumps are located near the high energy end of the accelerator, just prior to the object slits of the 90° analyzing magnet, and directly below the sample chamber and will hereafter be referred to as the accelerator diffusion pump, magnet diffusion pump, and sample chamber diffusion pump, respectively.

The accelerator diffusion pump is equipped with an optically opaque water-cooled baffle to prevent diffusion pump oil from backstreaming into the beam tube. Pressure at the accelerator is monitored by a Penning Discharge Vacuum Gauge which is connected via a feedback circuit to the accelerator control panel. This feedback loop will automatically shut down the machine should the accelerator diffusion pump backing pressure exceed approximately 10^{-2} Pa (10^{-4} torr). Ultimate achievable pressure with this system is roughly 10^{-5} Pa (10^{-7} torr), with a nominal accelerator operating pressure of 10^{-3} Pa (10^{-5} torr). The ultimate pressure is monitored by a Bayard-Alpert ionization gauge controlled by an ionization gauge controller mounted in the target room.

The magnet diffusion pump is also equipped with an optically opaque water-cooled baffle for suppression of backstreaming. An aluminum solid-body slide valve is mounted just above the pump and

baffle to allow pump isolation should access to the beam line be required. Pressure near the magnet diffusion pump is monitored by a Bayard-Alpert ionization gauge mounted on the beam tube above the Faraday cup adjacent to the magnet diffusion pump. Ultimate pressure near the magnet is roughly 10^{-5} Pa (10^{-7} torr) with a nominal operating pressure of 10^{-4} Pa (10^{-6} torr).

The sample chamber diffusion pump, mounted directly beneath the sample holder, is equipped with a Varian Model NRC 316-4 Cryotrap. This liquid nitrogen trap suppresses diffusion pump oil backstreaming and subsequent sample contamination. Mounted directly above the cryotrap is another aluminum solid-body slide valve which allows the sample chamber diffusion pump to be isolated and facilitates quick sample changes. A Bayard-Alpert gauge monitors sample chamber pressure.

A pumping impedance is mounted in the beam line just prior to the sample chamber. It is cooled with liquid nitrogen to prevent diffusion pump oil from streaming down the beam line and contaminating the samples. It is constructed with all-metal seals, as is the sample chamber, and is routinely baked-out at approximately 120°C to improve operating vacuum conditions.

Four gate valves are mounted at various locations along the beam line to allow isolation of various beam tube sections. A pneumatic gate valve is mounted just outside of the machine and is actuated when a pressure rise occurs in the accelerator diffusion pump backing line. This backing pressure is monitored by a single set-point

thermocouple gauge controller which can activate relays to close the gate valve and turn off the accelerator diffusion pump when the set-point pressure is exceeded.

B.3. Beam Handling Components

There are three major beam handling components situated along the beam line, including up-down, left-right steerers, a quadrupole doublet and a 90° analyzing magnet. The steerers are an in-house design and construction, while the quadrupole doublet and analyzing magnet are manufactured by Magnion, Inc. and ANAC, Inc. respectively.

The two sets of steerers are mounted immediately outside the accelerator tank and one meter from the end of the accelerator and are capable of translating the beam within the beam line. Each set of steerers consists of two magnet coils with 2600 turns of number 22 magnet wire around a 0.0254 meter (1 inch) core. The pole pieces consist of Armco iron mounted between the coils having dimensions of 0.064 m x 0.064 m x 0.051 m (2-1/2 in x 2-1/2 in x 2 in). The power supply, capable of producing ±2 amps for each set of steers, is constructed from two Model 440C 50 Watt Operational Power Amplifiers and one Model 526 Power Supply purchased from OPAMP Labs, Inc.

The quadrupole doublet, mounted approximately 1.5 meters from the end of the machine, is a Magnion Model QD 200. The coils of the quadrupole have 100 turns and are capable of carrying 30 amps. Power is supplied by two Varian Model 6021 current regulated power supplies capable of producing from 0-30 amps each. Each set of coils is

water-cooled to dissipate the 900 watts produced at full power operation.

The 90° analyzing Magnet, loacted 6 meters from the end of the accelerator, is an ANAC Model 3938. It has a maximum mass-energy product of 3.4 (amu•MeV/Z^2) at 90° with a gap field of 1.2 Tesla and a bending radius of 0.224 meters (8.8 in). The magnet power supply is a Hewlett-Packard Model 6269B, which provides 50 amps with current regulation of 0.02%. A power control center is also included in the magnet system. The center includes a breaker box and an interlock trip to switch off the power supply if the magnet exceeds maximum operating temperature or if the cooling water flow drops below a minimum required level. Object and image slits are used in conjunction with the analyzing magnet. These slits, manufactured by HVEC, are water-cooled and capable of dissipating 100 watts each.

B.4. Beam Monitoring Components

Beam characteristics are monitored along the beam line by two beam profile monitors, two Faraday cups and beam current integration electronics associated with the specimen holder. The beam profile monitors are a National Electrostatics Corporation Model BPM-45. The monitor are located directly beyond the quadrupole doublet and directly after the image slits. Two Faraday cups are located along the beam line. The cups, mounted between the quadrupole and the magnet and between the magnet and the sample chamber, are pneumatically operated and electrically suppressed to give accurate beam current readings.

The beam current integration electronics include an Ortec Model 439 Digital Current Integrator, a Mechtronics Nuclear Model 420 Scaler and a Mechtronics Nuclear Model 419 Counter. These components are all NIM bin modules mounted in the control panel. The integrator can handle beam currents ranging from 10^{-9} ampere to 10^{-2} ampere while the scaler-counter records the integrated current at a rate of up to 100 MHz. The integration electronics is accurate to within 0.10% as shown by tests with a constant current power supply.

B.5. Sample Holder and Heater

The sample holder, shown schematically in Fig. IV-5, consists of a stainless steel holder upon which is mounted a specimen holder capable of accommodating three 3 mm discs and/or three 0.5 cm x 1.0 cm foils. The sample holder maintains electrical isolation of the sample while it masks the irradiated area to allow for accurate measurement of the current density. The holder is heated by electron bombardment from a biased filament at high potential. The isolated sample is radiatively heated with the temperature measured with thermocouples attached behind each sample position. The temperature range of operation of this sample holder is roughly 100°C to 600°C.

The heater power supply is an Alpha Scientific Model 3000 current regulated 0-10 amp supply. The sample holder is biased to -10 KV with a Universal Voltronics high voltage power supply.

C. Specimen Preparation and Analysis

An important aspect of this study is the application of sample preparation techniques to allow examination of the samples in cross

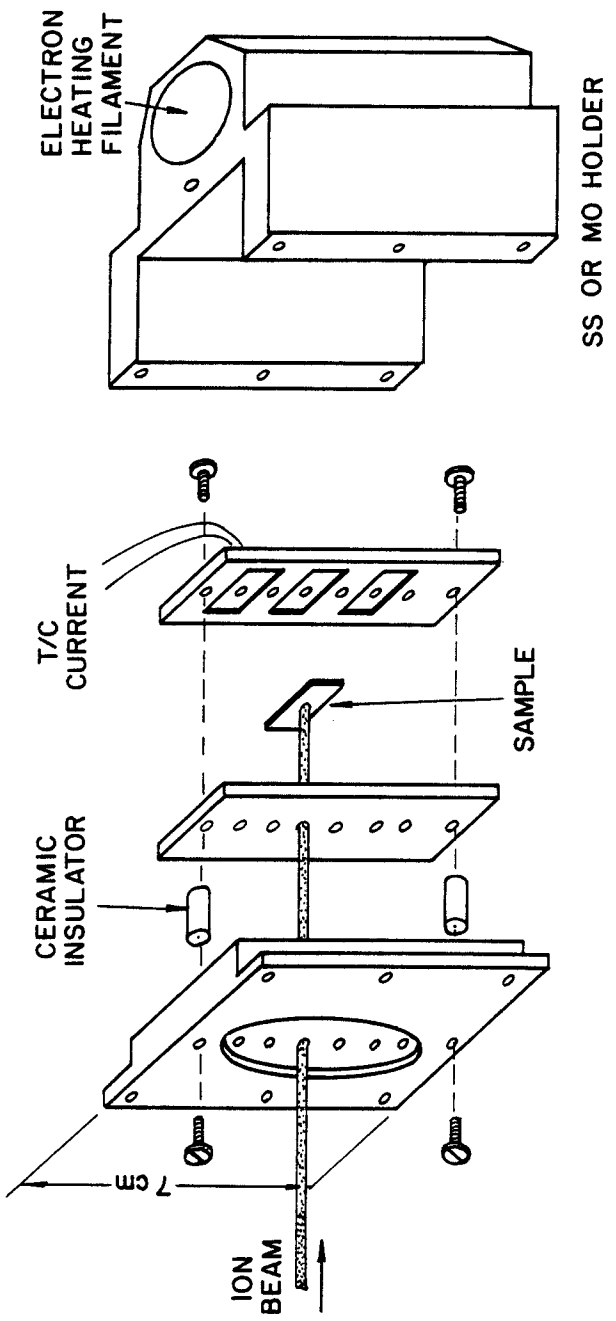

Fig. IV-5. Exploded view of sample holder for the 700 kV Accelerator Facility.

section. This technique, which has been used in previous studies,[2,6,12,13] allows a great deal more information to be obtained from each sample since both dose and dose rate are depth dependent. To accomplish this cross sectioning, great care must be taken in pre-irradiation and post-irradiation sample preparation.

C.1. Pre-Irradiation Specimen Preparation

Prior to irradiation the pure nickel foils, which are approximately 0.01 m x 0.005 m (1 cm x 0.5 cm), are annealed at 1000°C for one hour. The annealing is carried out in a vertical stainless steel tube through which high purity argon gas flows. The specimens are suspended at the center of the tube furnace in a stainless steel mesh cage into which are inserted two chromel-alumel thermocouples to monitor the annealing temperature.

It is extremely important that the surfaces of each specimen be clean to allow metal to be plated to them following irradiation. To insure good plating adherence, prior to irradiation each specimen is mechanically ground on abrasive paper (#240-#600) and mechanically polished in a vibratory metallographic polisher using a 0.3 μm alumina slurry. It should be noted that the samples are not electropolished prior to irradiation as has been done in previous studies.[2,6] This was done to prevent the introduction of interstitial gas atoms other than those implanted during the preinjection irradiations.

C.2. Post-Irradiation Specimen Preparation

The specimens, which are irradiated to the fluences indicated in Chapter V, are removed from the respective specimen holder, immediately immersed in alcohol and transported to the polishing facility. The specimens are then placed in a nickel electroplating solution where from 0.001 m to 0.0015 m (1-1.5 mm) of nickel is plated onto each side of the foil in the manner developed and described in detail by J.B. Whitley.[2] Upon completion of the plating the samples are removed from the solution, mounted in epoxy and sliced with a low speed diamond saw in a direction normal to the foil surface, as shown in Fig. IV-6. Standard 3 mm TEM discs are then removed from these slices and thinned for analysis using a twin-jet electropolishing unit.

C.3. Analysis

Once satisfactory electron microscopy samples have been obtained, the specimens are analyzed using a JEOL 120B transmission electron microscope. The depth distribution of the voids was determined by division of the micrographs into regions of uniform thickness parallel to the irradiated surface.

Quantitative analysis of the void number density required the determination of the foil thickness for each TEM foil. This was determined using stereo pair techniques where the image parallax was measured using a Hilgar Watts stereoviewer. The foil thickness t (in angstroms) was determined using the equation

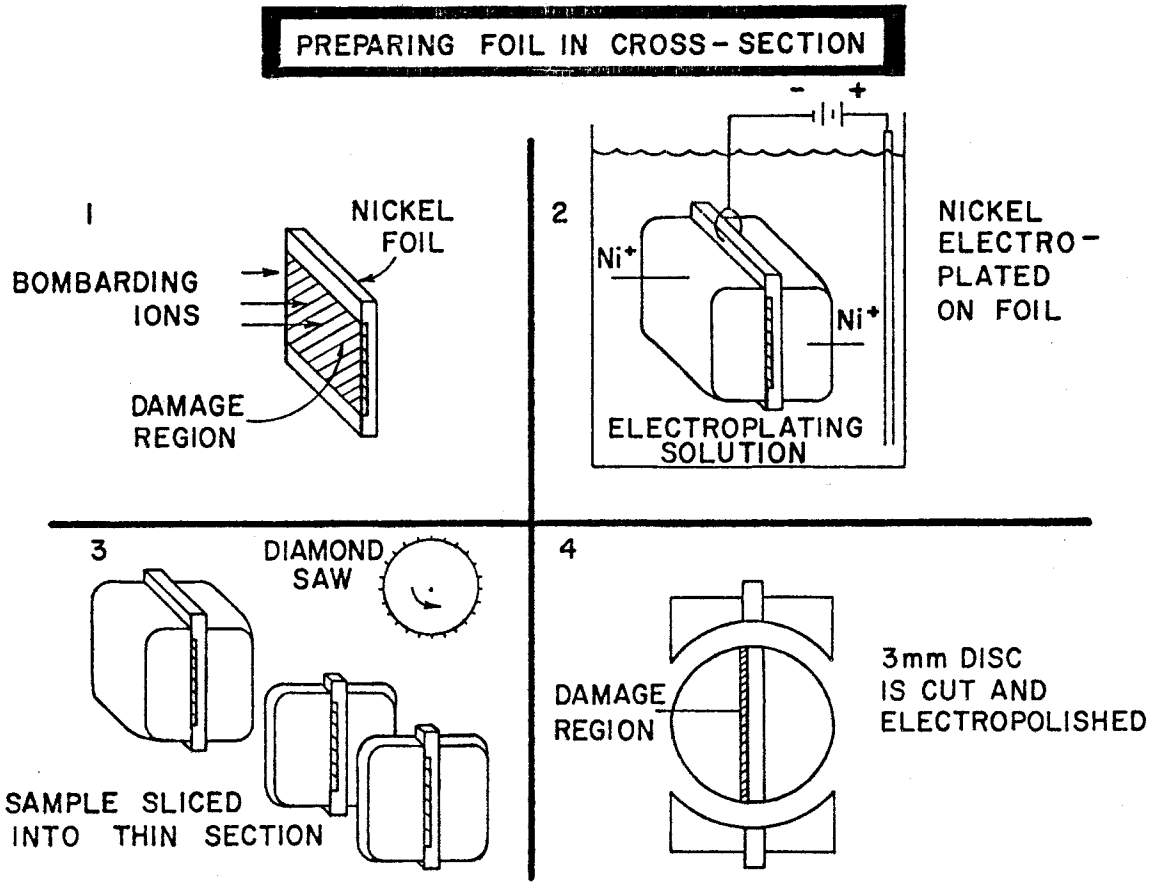

Fig. IV-6. Schematic of the preparation steps of a foil cross-sectioned for TEM analysis.

$$t = \frac{p \times 10^7}{2M \sin\left(\frac{\theta}{2}\right)} \qquad \text{(IV-2)}$$

where p was the image parallax in mm determined using features on opposite surfaces, M is the magnification of the analyzed print and θ is the total angle of tilt between the prints.

Void size was determined using a Zeiss particle counter and the data is reduced in a manner similar to Whitley,[2] Knoll,[6] and Ryan.[14] The average void size $\bar{d}$ was given by

$$\bar{d} = \frac{1}{N} \sum n_i' \, d_i \qquad \text{(IV-3)}$$

where n_i' is the corrected void count for each class which accounts for the intersection of voids with the foil surface, and $N = \sum n_i'$. The standard deviation of the void size distribution was determined using

$$\sigma = \left\{\frac{1}{N} \sum n_i \, (d_i - \bar{d})^2\right\}^{1/2} . \qquad \text{(IV-4)}$$

The swelling was calculated using

$$\frac{\Delta V}{V'} = \frac{\pi}{6} \frac{1}{V'} \sum n_i' \, d_i^3 \qquad \text{(IV-5)}$$

where V' was the foil volume analyzed.

C.4. Error Analysis

The interpretation of any experimental results requires an understanding of the magnitude of possible errors encountered during data acquisition. For this study, attempts to minimize errors included consistency in sample heat treatment, pre-irradiation preparation, handling, storage, irradiation temperature and irradiation fluence. The irradiation flux in this experiment varied by about a factor of two for different irradiations. This variation is considered in the dose rate analysis discussed in Chapter VI.

The limiting factor in the determination of microstructural data with transmission electron microscopy techniques is the calculation of sample thickness. In an attempt to minimize error in this experiment the foil thickness was determined at 2 or 3 depths from the surface for each sample with this thickness variation incorporated into the void number density calculations. The relative error for foil thickness determination was 30-40%. Coupling this error with the probable error of 5-10% in measuring mean void diameters gave an error in the calculated swelling which was about 50%. Hence, when interpreting the data from the figures presented in Chapter V, an error of 50% was assumed for all swelling data. Errors of 40% and 10% were assumed for void number density and mean void diameter data, respectively.

References for Chapter IV

1. W.J. Weber, Ph.D. Thesis, University of Wisconsin, Madison, Wisconsin, 1977.

2. J.B. Whitley, Ph.D. Thesis, University of Wisconsin, Madison, Wisconsin, 1978.

3. R.G. Lott, Ph.D. Thesis, University of Wisconsin, Madison, Wisconsin, 1979.

4. K.Y. Liou, Ph.D. Thesis, University of Wisconsin, Madison, Wisconsin, 1979.

5. R.H.C. Zee, Ph.D. Thesis, University of Wisconsin, Madison, Wisconsin, 1981.

6. R.W. Knoll, Ph.D. Thesis, University of Wisconsin, Madison, Wisconsin, 1981.

7. H.V. Smith and R.G. Lott, Nucl. Inst. Methods 143, 125-132 (1977).

8. J.H. Billen and H.T. Richards, Proc. of Symp. of Northeastern Accelerator Personnel, CONF-781051, Oak Ridge National Laboratory, Oak Ridge, TN, p. 137, Oct. 1978.

9. J.H. Billen, "A Radio Frequency He^- Source and a Source of Negative Ions by Cesium Sputtering," IEEE Trans. Nuclear Science, (1981).

10. J.H. Billen, "Enhanced Axial Erosion of the Sputter Cathode in SNICS," Proc. of the 3rd International Conference of Electrostatic Accelerator Technology, CONF 81-CH1639-4, Oak Ridge, TN, p. 238, April 13-16, 1981.

11. J.H. Billen, Rev. Sci. Instrum. 46 No. 1, (Jan. 1975) 33-40.

12. G. Fenske, S.K. Das, and M. Kaminsky, J. of Nucl. Matl. 103&104 (1981) 1231.

13. G. Fenske, S.K. Das, M. Kaminsky, and G.H. Miley, J. of Nucl. Matl. 85, 707-711 (1979).

14. T.D. Ryan, Ph.D. Thesis, University of Michigan, Ann Arbor, Michigan, p. 64 (1975).

CHAPTER V

RESULTS

During the course of this study, numerous samples of high purity nickel were irradiated with hydrogen or helium ions and/or 14 MeV nickel ions under various conditions and analyzed using the cross-section technique. Since interstitial gas atoms are introduced into the samples prior to nickel ion irradiation, it is necessary to understand the impurities present in the irradiated nickel. Table V-1 gives an impurity analysis prior to pre-irradiation annealing for the MARZ grade nickel (< 0.005% total impurities) irradiated in this study. A summary of the samples and irradiation conditions of this study is presented in Table V-2. This chapter consists of four sections each dealing with different aspects of the irradiated samples. The first sections deals with samples which were not pre-injected with interstitial gas atoms with the 700 kV Accelerator Facility. (Some of the samples were electropolished prior to nickel ion irradiation.) The irradiation temperature was varied to allow for the study of the effects of injected self-interstitials. The second section of this chapter presents results from samples pre-injected with various fluences of hydrogen ions at room temperature and irradiated with 14 MeV nickel ions at 525°C and 625°C. The third section gives the results of samples preinjected with various concentrations and energies of helium ions and subsequently irradiated with nickel ions. A discussion of the results obtained by preinjection

TABLE V-1. MARZ GRADE NICKEL IMPURITY ANALYSIS*

Impurity Element	Content (wt-ppm)
O	< 10
C	10
H	< 10
N	10
Fe	20
Cu	3
Ge	6
All others	< 5

*Before pre-irradiation anneal at 1000°C for 1 hour.

will be presented in Chapter VI and related to the results of the nickel ion irradiated samples which were preinjected. The final section of this chapter contains a brief summary of the results presented including the swelling at 1 μm, peak swelling, line dislocation density and loop density for each sample.

A. Injected Interstitial Effects

Initial irradiations conducted in this study did not include gas atom preinjection since the 700 kV Accelerator Facility was not yet completed. Samples were prepared in a manner similar to Whitley[1] which introduced interstitial hydrogen via a pre-irradiation electropolish. Whitley completed an irradiation at 400°C and noted a large variation in the irradiated microstructure as a function of depth.

TABLE V-2. SAMPLES AND IRRADIATION CONDITIONS

Sample Designation	Irrad. Temp. (°C)	Gas Content (appm)	Fluence (ions/m^2) x 10^{20}	Dose at 1 μm (dpa)	Dose Rate (dpa/sec) x 10^{-4}	Preinject Energy (keV)	Preinject Fluence x $10^{18}/m^2$
No Preinjection							
T-20-00-03	450	Polished	0.5	1	9	0	0
T-20-00-05	425	Polished	0.5	1	9	0	0
T-20-00-14	525	Polished	5.0	13	12	0	0
T-20-00-25	525	No gas	2.5	7	22	0	0
T-20-00-26	400	No gas	5.0	13	21	0	0
H Preinjection							
T-20-100H-18	625	100 H	5.0	13	8	200-700	3
T-20-1000H-27	625	1000 H	2.5	7	11	200-700	30
T-20-500H-28	625	500 H	2.5	7	10	200-700	15
T-20-100H-29	625	100 H	2.5	7	12	200-700	3
T-20-1000H-30	525	1000 H	2.5	7	12	200-700	30
T-20-500H-31	525	500 H	2.5	7	12	200-700	15
T-20-100H-32	525	100 H	2.5	7	12	200-700	3
T-20-100H-33	525	100 H	1.7	4	9	200-700	3
T-20-100H-34	525	100 H	10.0	27	11	200-700	3
He Preinjection							
T-20-100-09	625	100 He	1.0	3	14	200-700	12
T-20-600-10	625	600 He	1.0	3	14	200-700	68
T-20-100-11	525	100 He	1.0	3	14	200-700	13
T-20-100-12	525	100 He	2.5	7	16	200-700	13
T-20-650-20	525	650 He	5.0	13	20	700	20
T-20-65-21	525	65 He	2.5	7	22	700	2
T-20-650-22	525	650 He	10.0	27	21	700	21
T-20-3250-23	525	3250 He	2.5	7	21	700	103
Preinjection Study							
A-20-1000-1	25	1000 He	---	---	---	200-700	115
A-20-1000H-4	25	1000 H	---	---	---	200-700	30
A-20-100-8	25	1000 He	---	---	---	200-700	114
A-20-1000H-12	25	1000 H	---	---	---	200-700	30
A-20-10000-15	25	10000 He	---	---	---	200-700	955

Whitley found voids near the surface, ordered loops at the peak damage region and voids at the end of range.

The present study completed irradiations at 450°C, 425°C and 400°C to further investigate this variation in microstructure which Whitley attributed to dose rate effects. Suppression of void formation was also noted in nickel irradiated at 450°C (Fig. V-1). This sample received a pre-irradiation electropolish and was irradiated to a nickel ion fluence of 5×10^{19} ions/m^2 producing a damage level of about 7 dpa at the peak damage region. The effect of the injected self-interstitials which have a range of approximately 2 μm is shown dramatically in Fig. V-2. Note the dramatic decrease in void number density and hence swelling at a depth of 2 μm.

Another example of void suppression is shown in Fig. V-3. This is a micrograph of a nickel sample which had the same pre-irradiation electropolish and was irradiated with nickel ions at 425°C to a fluence of 5×10^{19} ions/m^2. Note the slight broadening in the region of void suppression which is shown more quantitatively in Fig. V-4. The void number density is increased while the swelling is reduced in comparison to Fig. V-2 illustrating the temperature dependence of cavity nucleation. This sample was analyzed by R.L. Sindelar.[2]

A final example of suppressed void formation is shown in Fig. V-5. This micrograph shows a nickel sample which was not electropolished prior to irradiation with nickel ions at 400°C to a fluence of 5×10^{20} ions/m^2. This represents a damage level of about 13 dpa at 1 μm and 53 dpa at the peak damage region. Note the ordered loop

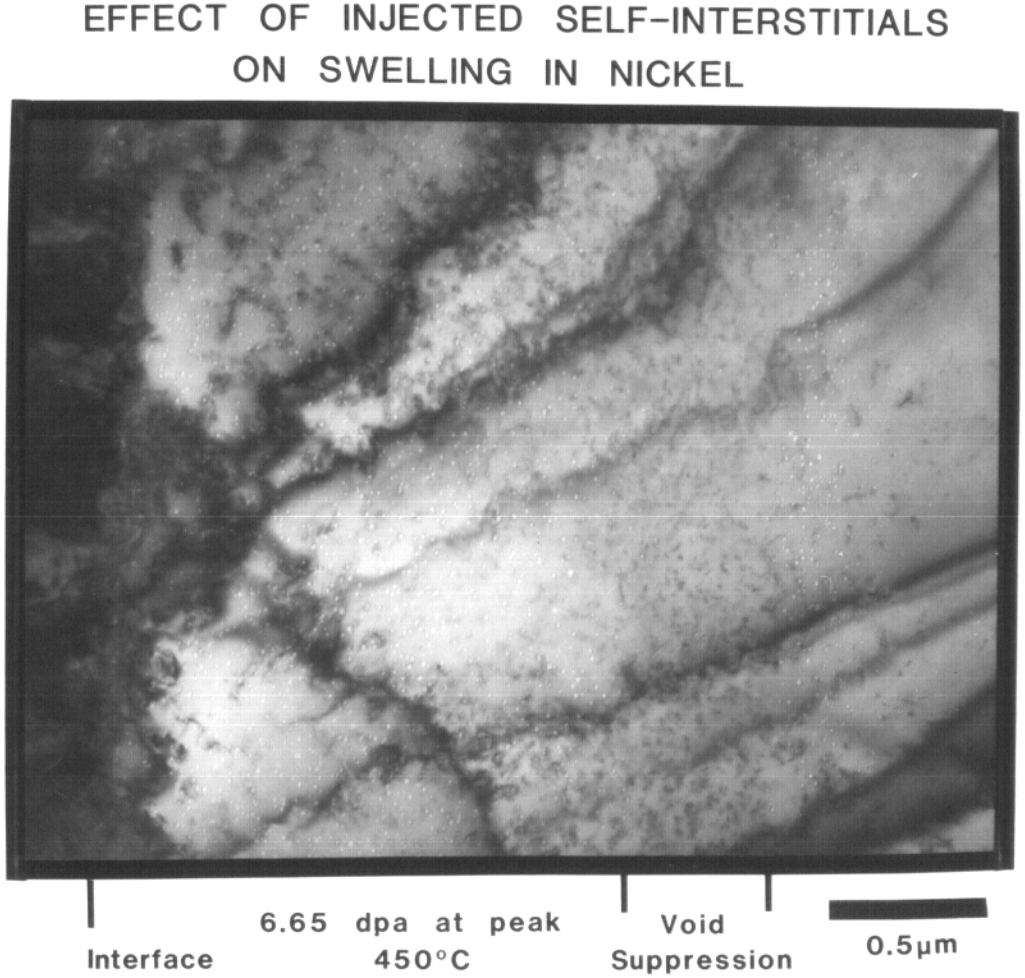

FIG. V-1. VOID SUPPRESSION BY INJECTED SELF-INTERSTITIALS IN NICKEL AFTER IRRADIATION AT 450°C TO A FLUENCE OF 5×10^{19} IONS/M^2.

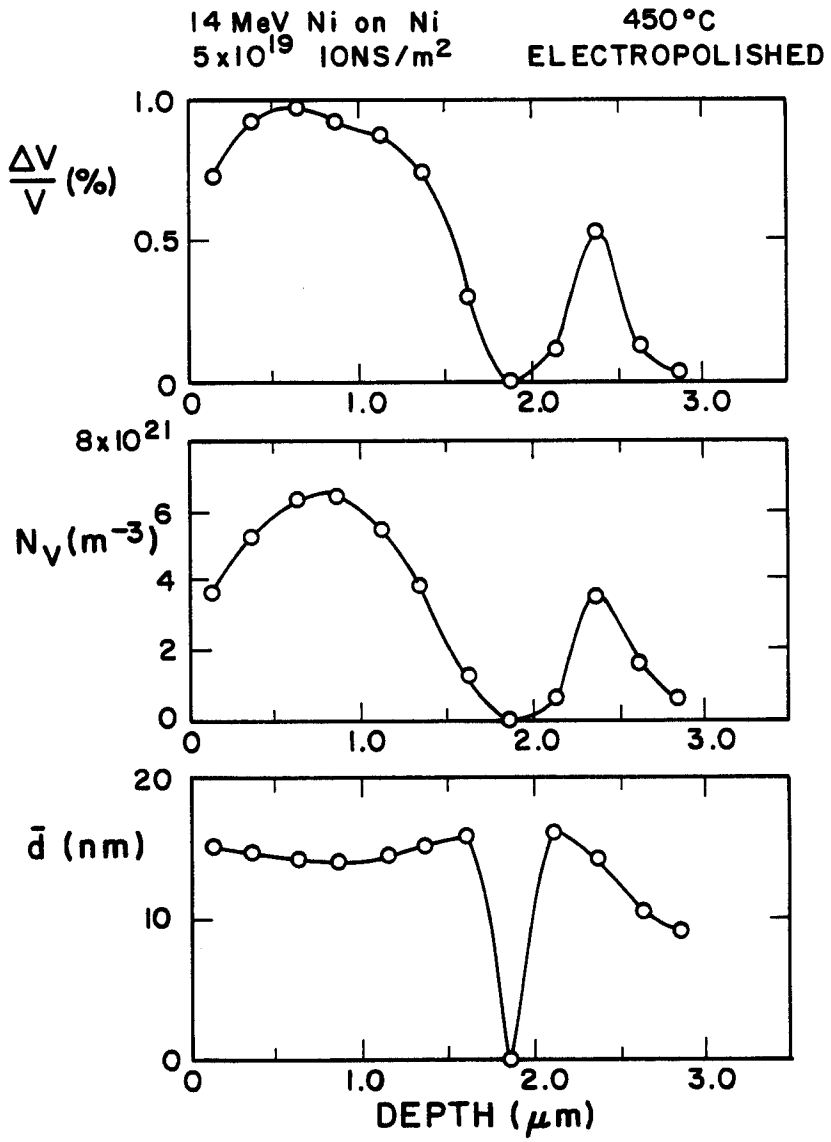

Fig. V-2. Swelling, void number density and mean void diameter vs. depth in nickel irradiated at 450°C to a fluence of 5 x 10^{19} ions/m^2.

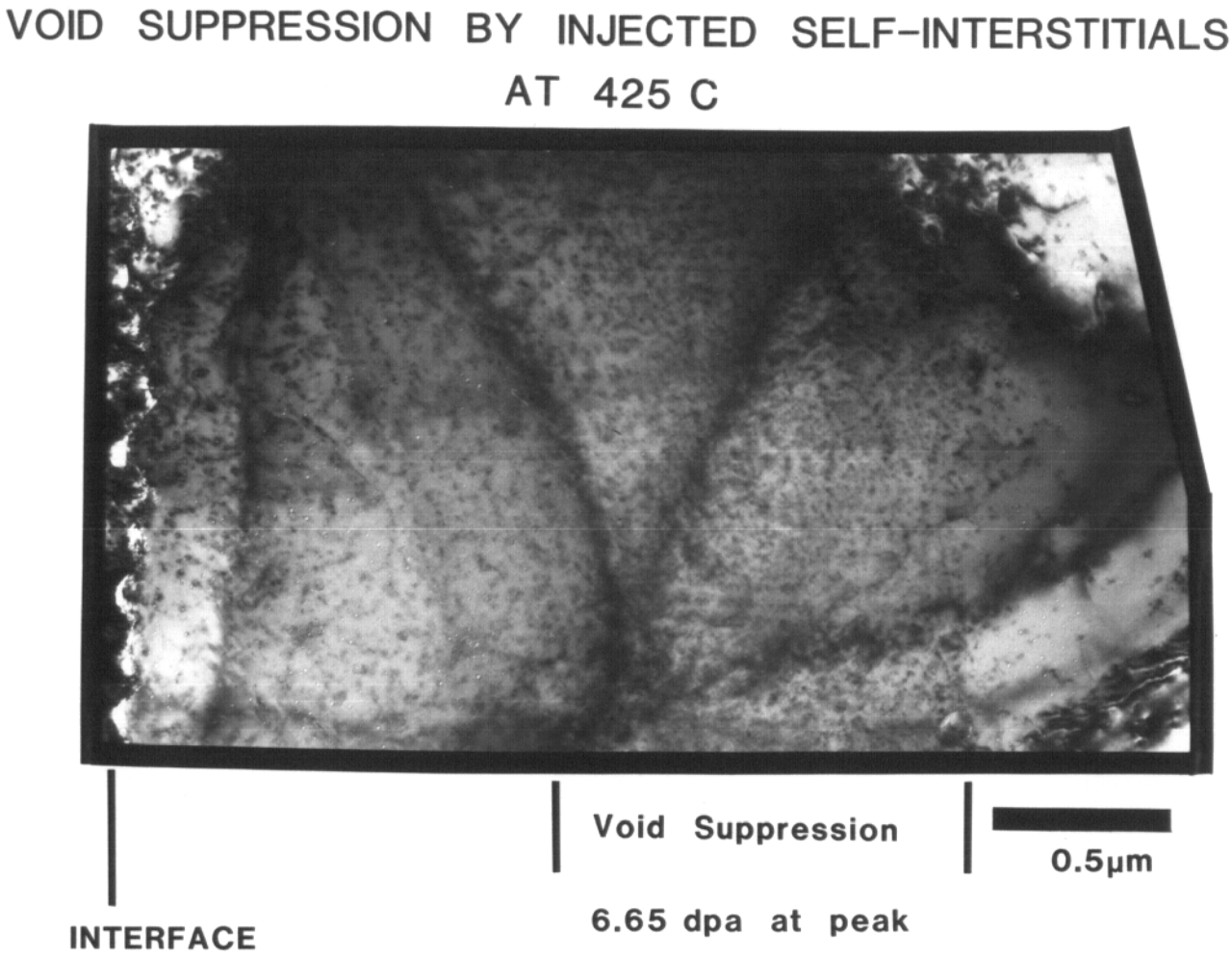

FIG. V-3. ENHANCED VOID SUPPRESSION IN SELF-ION IRRADIATED NICKEL AT 425°C WITH A FLUENCE OF 5×10^{19} IONS/M^2.

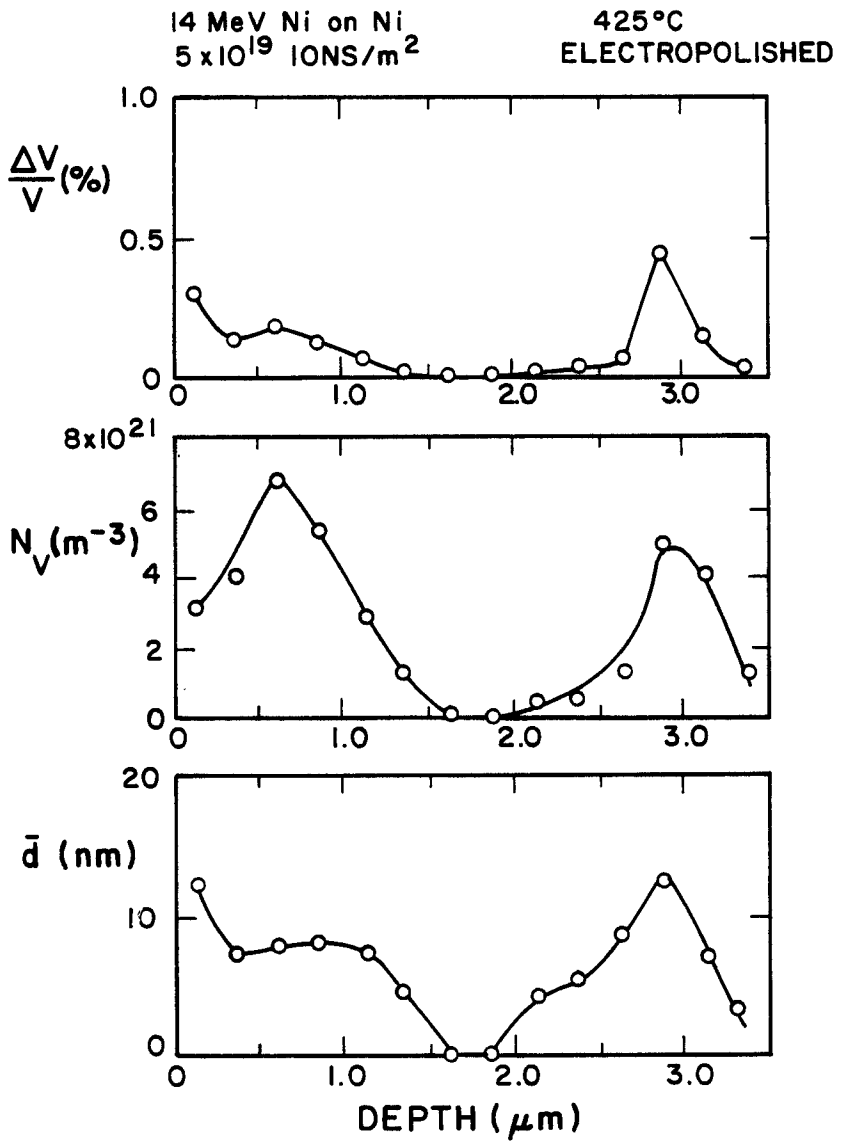

Fig. V-4. Swelling, void number density and mean void diameter vs. depth in nickel irradiated at 425°C to a fluence of 5 x 10^{19} ions/m^2 as obtained by Sindelar.(2)

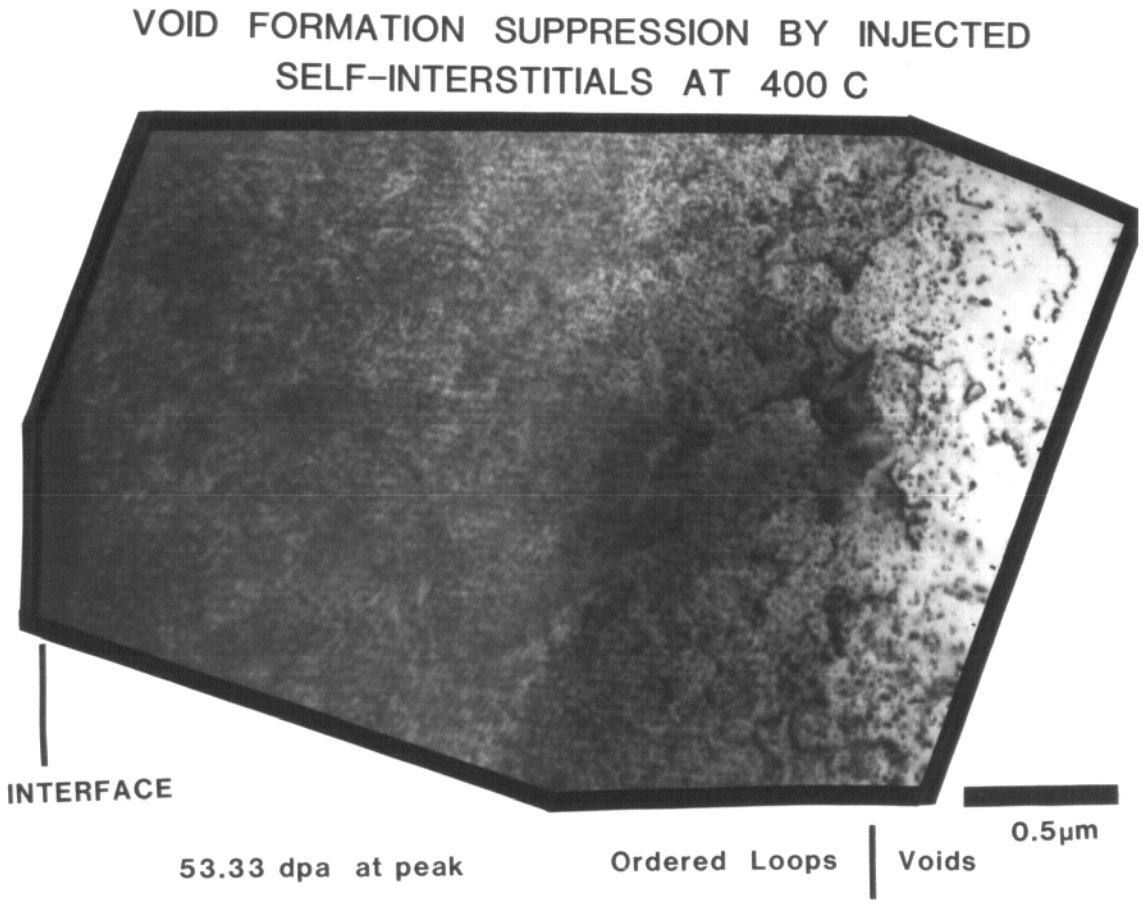

FIG. V-5. VOID SUPPRESSION AND ORDERED LOOP FORMATION IN NICKEL IRRADIATED AT 400°C WITH 14 MeV NICKEL IONS TO A FLUENCE OF 5×10^{20} IONS/M^2.

formation throughout the damage region and the void formation at the end of range. The ordered loops are spaced approximately 35 nm apart. The mean void diameter is 14.7 nm and the number density is 2.1×10^{21} m^{-3} as shown in Fig. V-6. This produces a swelling of 0.32% at the end of range which is slightly more than the swelling at the end of range for the previous 425°C sample.

Irradiations completed at temperatures of 525°C or greater show little effect of injected interstitials on nucleation. This can be seen in Fig. V-7 which shows a nickel specimen which received a pre-irradiation electropolish and was then irradiated with nickel ions to a fluence of 5×10^{20} ions/m^2 at a temperature of 525°C. In contrast to the void suppression shown in the previous micrographs, this sample shows a peak in the void number density near the peak damage region as indicated in Fig. V-8. There is also a marked variation in the void size as a function of depth. There are large voids near the surface of the foil and at the end of range, with smaller voids near the peak damage region. These are similar to the results seen by Whitley for an irradiation with similar conditions.

A final example of self-ion irradiated nickel with no gas introduced by preinjection or pre-irradiation electropolish is shown in Fig. V-9. This sample was annealed at 1000°C for 1 hour in an argon atmosphere (as were all irradiated samples), mechanically polished and then irradiated with 14 MeV nickel ions at 525°C to a fluence of 2.5×10^{20} ions/m^2. Note the low number density and associated low swelling produced in this sample as shown in Fig. V-10. Also note

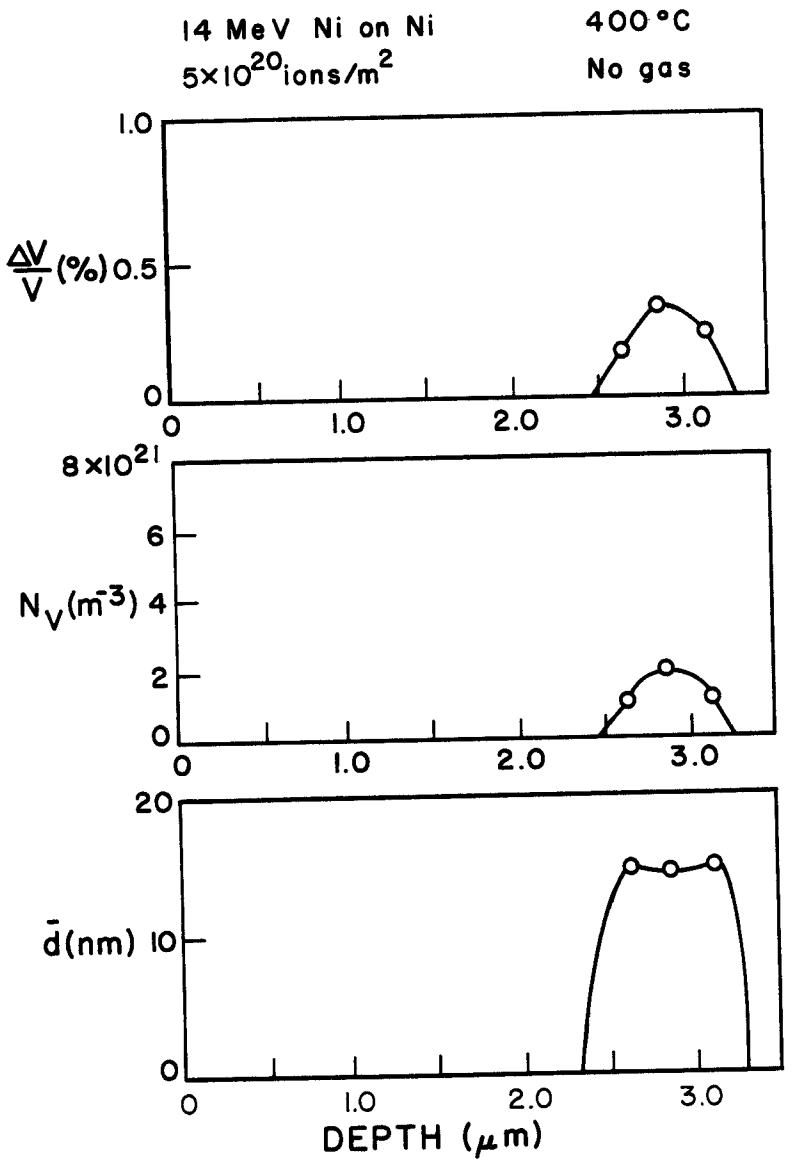

Fig. V-6. Swelling, void number density and mean void diameter vs. depth in nickel irradiated at 400°C to a fluence of 5 x 10^{20} ions/m^2.

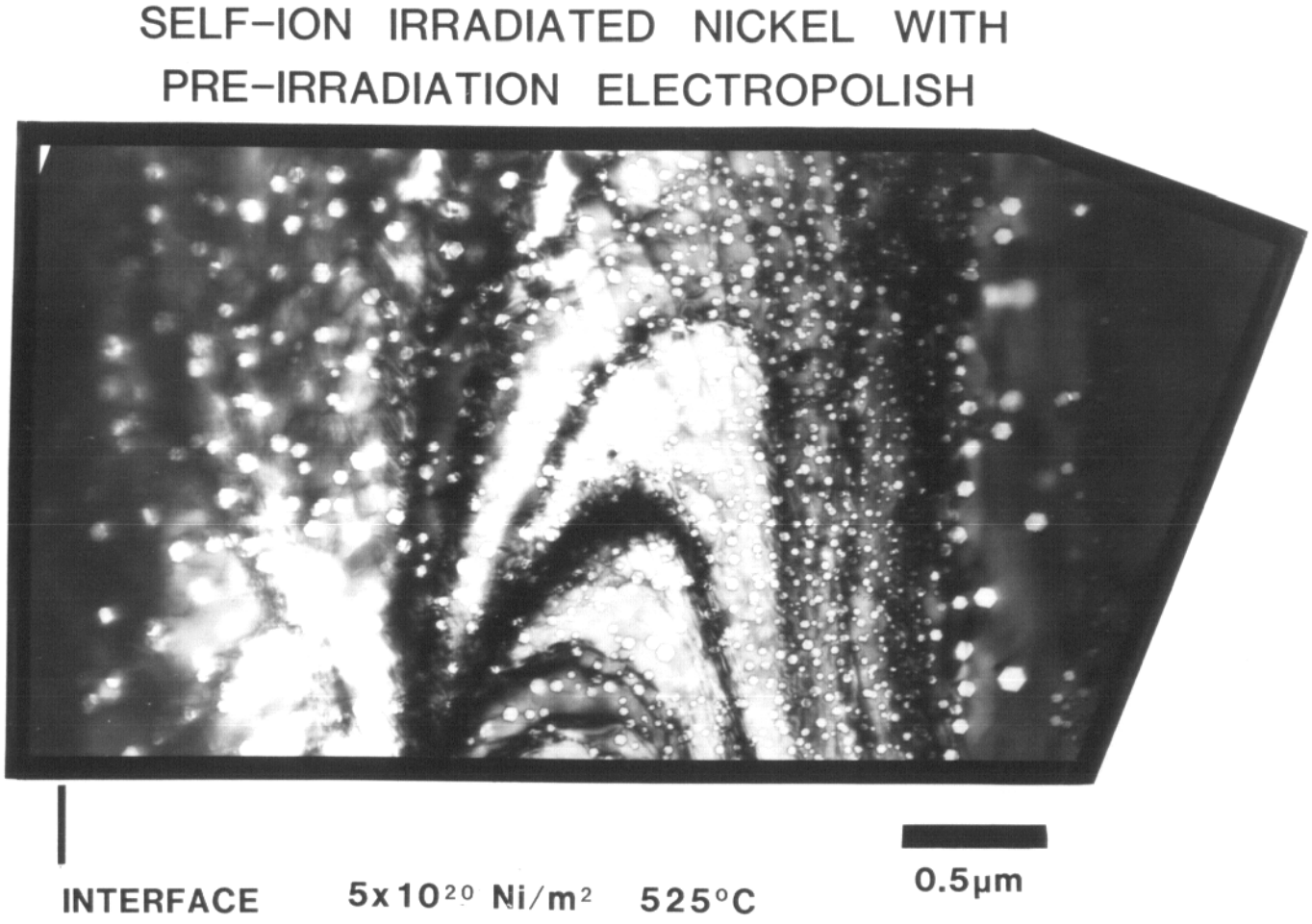

FIG. V-7. DEPTH DEPENDENT MICROSTRUCTURE IN ELECTROPOLISHED NICKEL IRRADIATED WITH 14 MEV NICKEL IONS AT 525°C TO A FLUENCE OF 5×10^{20}.

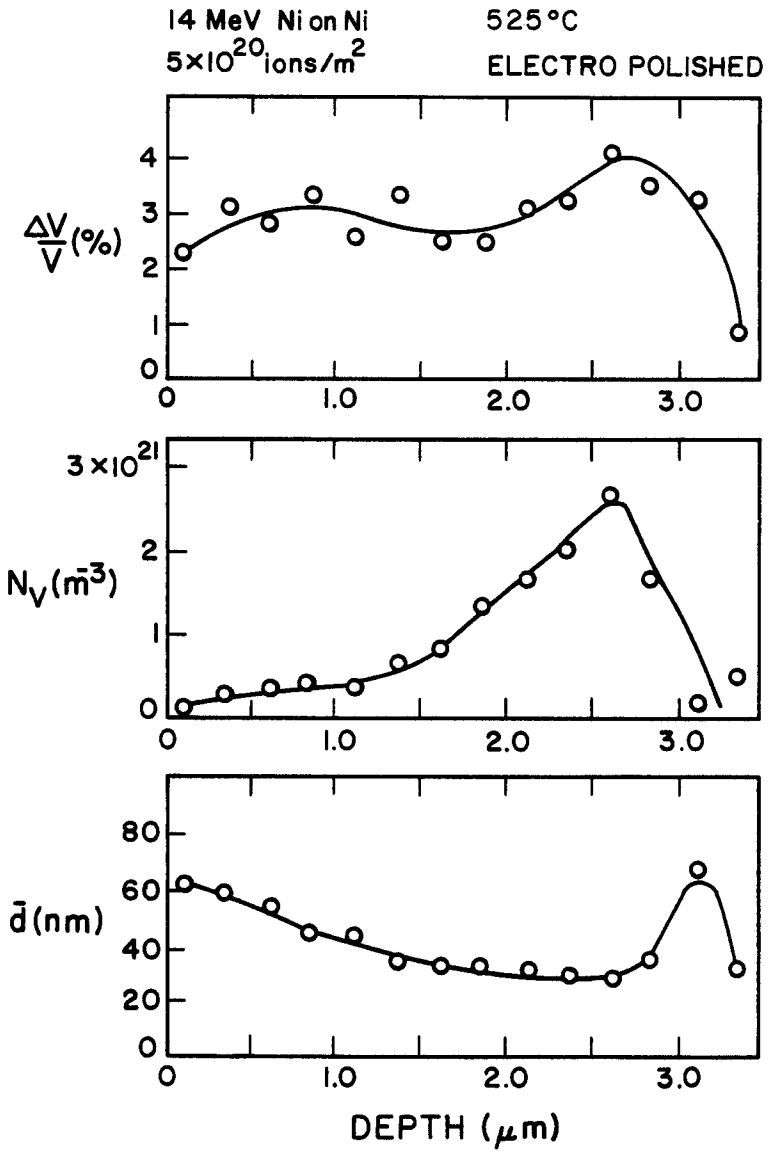

Fig. V-8. Swelling, void number density and mean void diameter vs. depth in nickel irradiated at 525°C to a fluence of 5 x 10^{19} ions/m^2.

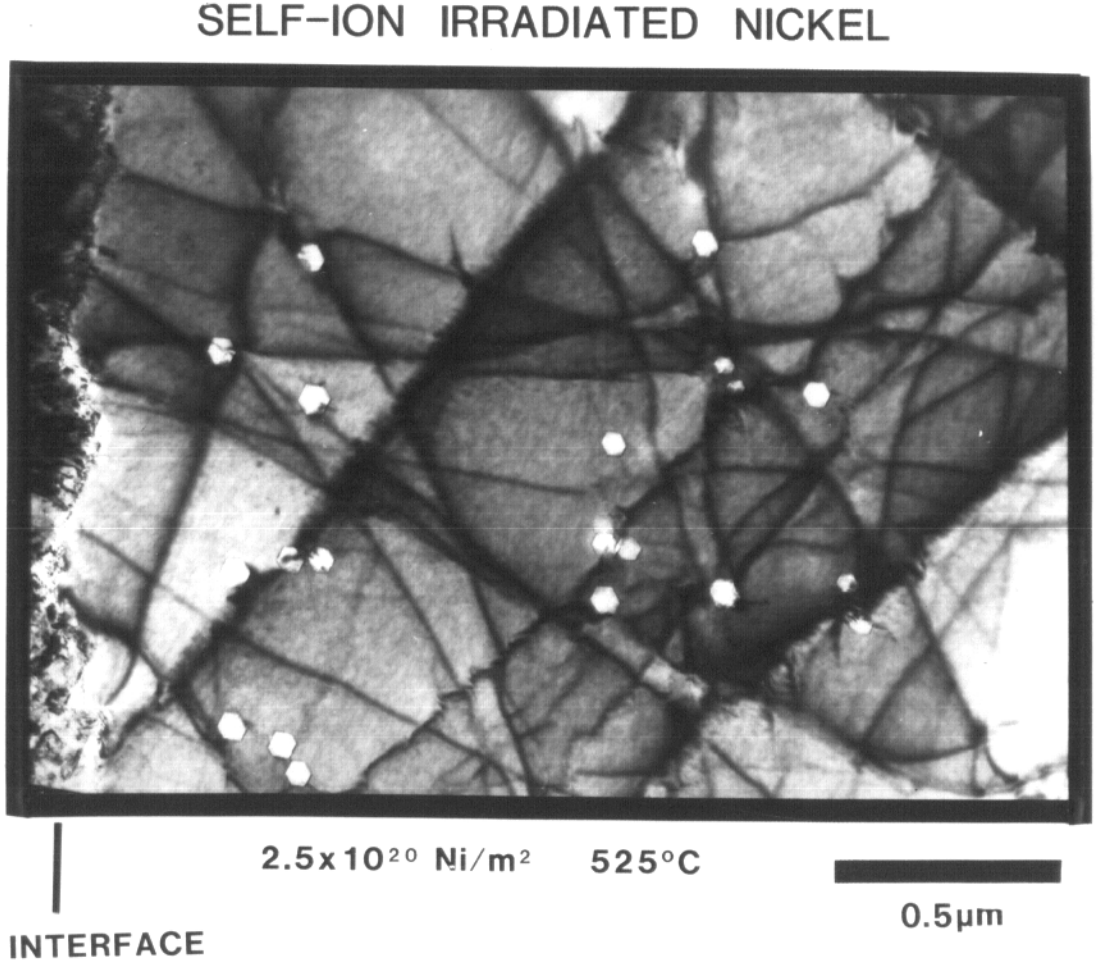

FIG. V-9. VOID MICROSTRUCTURE IN NICKEL AFTER SELF-ION IRRADIATION TO A FLUENCE OF 2.5 x 10^{20} IONS/M^2 WITH NO PREINJECTED GAS.

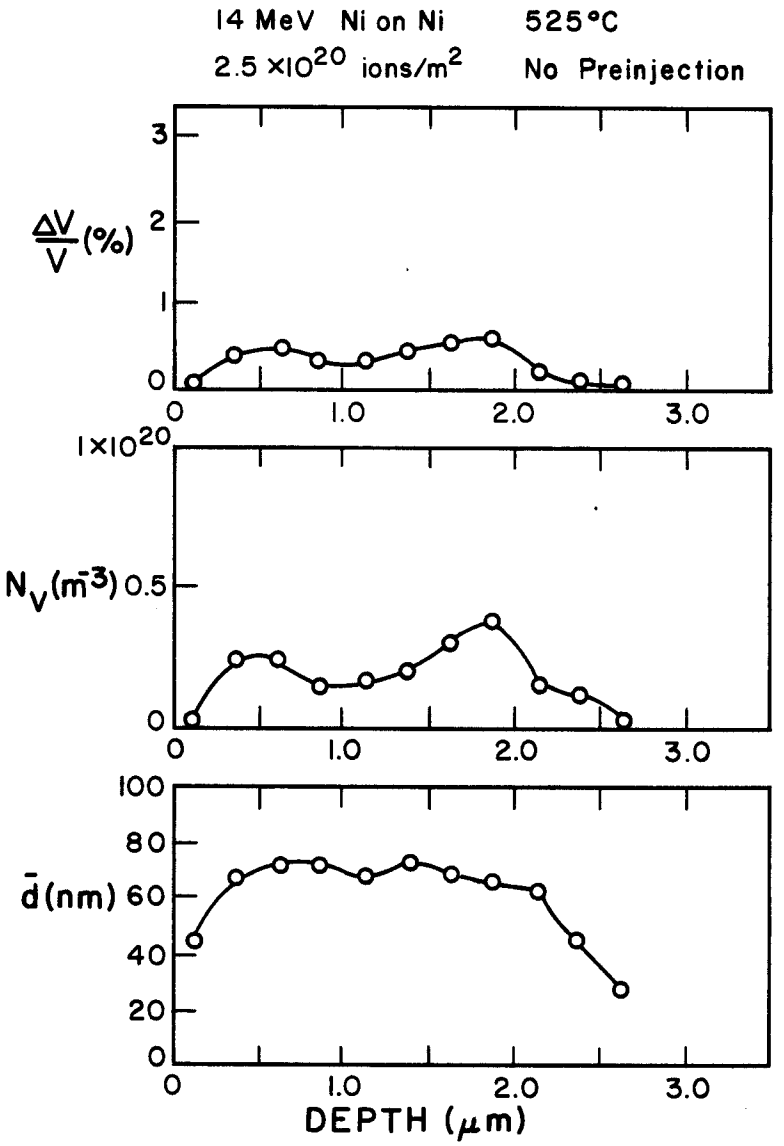

Fig. V-10. Swelling, void number density and mean void diameter vs. depth in nickel irradiated at 525°C to a fluence of 2.5 x 10^{20} ions/m^2.

the relatively large mean void diameter (~ 70 nm). This sample will be used as a basis for comparison for samples preinjected with hydrogen and irradiated to the same fluence at the same temperature. The results of these irradiations are presented in the following section.

B. Preinjected Hydrogen Effects

In an attempt to understand the role of hydrogen as a nucleating agent for void formation in nickel, well annealed nickel foils were mechanically polished and preinjected with various fluences of H_3^+ (3×10^{18} m^{-2} - 3×10^{19} m^{-2}, 100-1000 appm). The actual hydrogen fluence is 3 times the H_3^+ fluence ($3H/H_3^+$). These samples were then irradiated with nickel ions at either 525°C or 625°C to fluences ranging from 1.7×10^{20} ions/m^2 to 1×10^{21} ions/m^2. A notable hydrogen effect was found for irradiations at both temperatures with a constant nickel ion fluence (2.5×10^{20} ions/m^2).

B.1. 525°C Irradiations

A nickel sample preinjected with a fluence of 3×10^{18} H_3^+/m^2 (100 appm) at 25°C and irradiated with nickel ions to a fluence of 2.5×10^{20} ions/m^2 is shown in Fig. V-11. The swelling, void number density and mean void diameter as a function of depth are given in Fig. V-12. A comparison of data in Fig. V-10 and Fig. V-12 shows a slight increase in swelling which is mainly due to a dramatic increase in void number density. This increase is tempered somewhat due to the decrease in mean void diameter.

Increasing the preinjected hydrogen fluence to 1.5×10^{19} H_3^+/m^2 and 3×10^{19} H_3^+/m^2 (500 and 1000 appm, respectively) further in-

PREINJECTED HYDROGEN EFFECT IN SELF-ION IRRADIATED NICKEL
LOW HYDROGEN FLUENCE

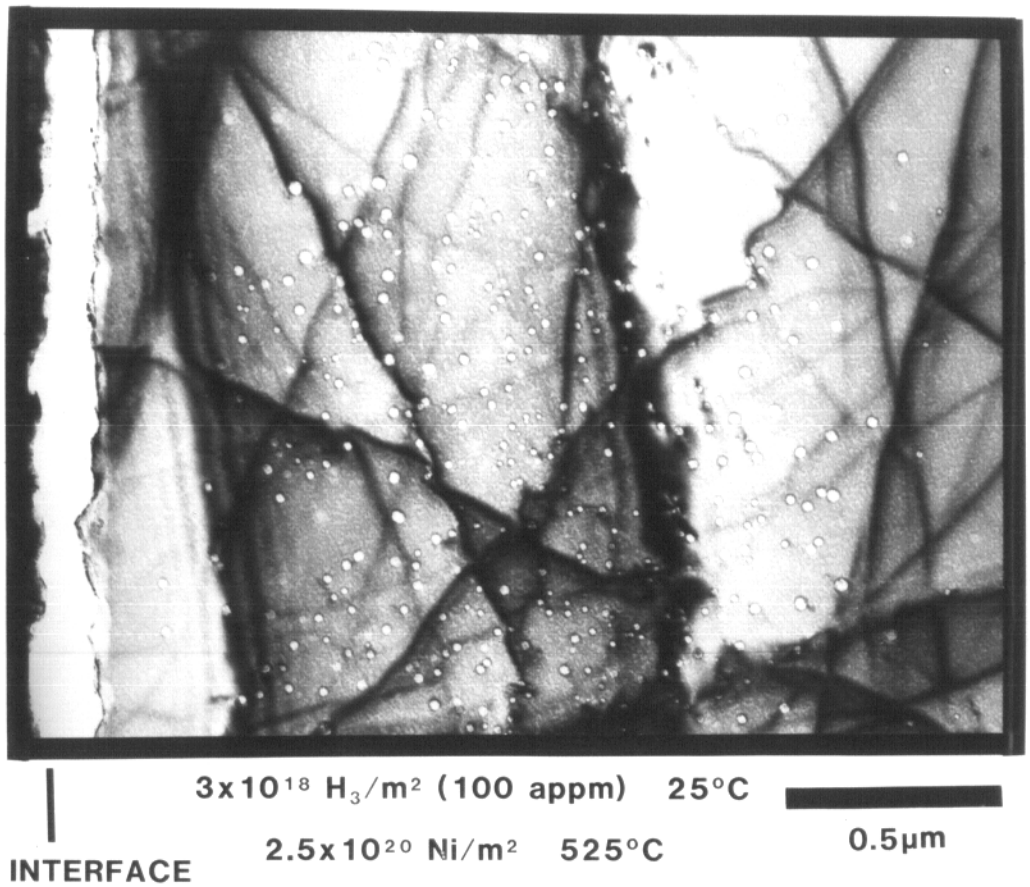

FIG. V-11. VOID FORMATION IN SELF-ION IRRADIATED NICKEL IRRADIATED TO A FLUENCE OF 2.5 x 10^{20} IONS/M^2 AT 525°C PREINJECTED WITH 3 x 10^{18} H_3^+/M^2 (100 APPM) AT 25°C.

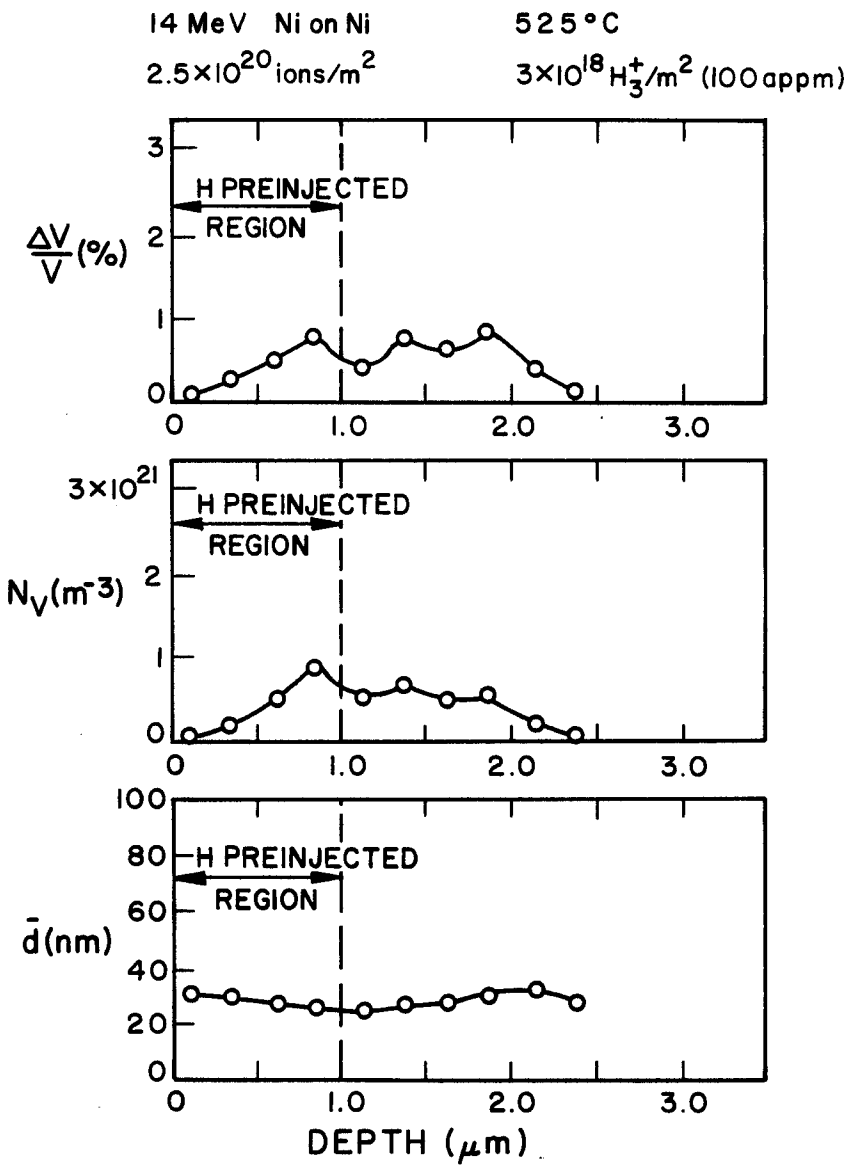

Fig. V-12. Swelling, void number density and mean void diameter vs. depth in hydrogen preinjected (3×10^{18} H_3^+/m^2) Ni irradiated at 525°C to a fluence of 2.5×10^{20} ions/m^2.

creases the swelling as shown by the micrographs (Fig. V-13 and Fig. V-15) and void data plots (Fig. V-14 and Fig. V-16). However, the mechanism by which the swelling increases changes somewhat. The 500 appm sample shows an increase in the void number density with a somewhat smaller mean void diameter when compared to the 100 appm preinjected sample. The high hydrogen fluence sample (100 appm injected, Figs. V-15 and V-16) again shows a slight swelling increase. This change is due to a slight increase in the mean void diameter coupled with a small decrease in the void number density. Further comparisons between these samples will be discussed in Chapter VI of this report.

The effect of a variation in damage level at a constant temperature and hydrogen concentration was studied by irradiating samples at 525°C which were preinjected with a hydrogen fluence of 3×10^{18} H_3^+/m^2 (100 appm) at 25°C. The low damage sample (Fig. V-17) was irradiated with nickel ions to a fluence of 1.7×10^{20} ions/m^2 (approximately 5 dpa at 1 μm). Figure V-18 gives the void data for this specimen. Note the surface denuded zone and the dislocation microstructure at a depth of 1 μm. The high damage sample, shown in Fig. V-19 was irradiated to a fluence of 1×10^{21} ions/m^2 (27 dpa at 1 μm). The swelling, void number density and mean void diameter as a function of depth are given in Fig. V-20. Note the variation in void orientation in the sample shown in Fig. V-19. This is evident as different void shapes (hexagon vs. diamond) in the same crystal.

PREINJECTED HYDROGEN EFFECT IN SELF-ION IRRADIATED NICKEL
INTERMEDIATE HYDROGEN FLUENCE

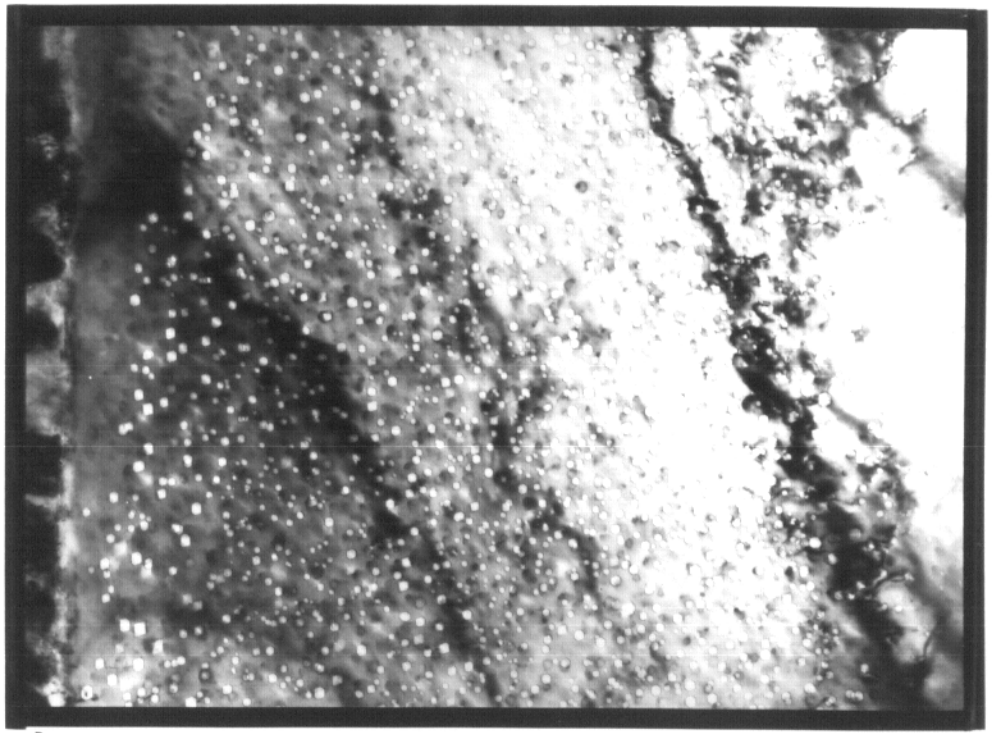

FIG. V-13. VOID MICROSTRUCTURE IN NICKEL IRRADIATED WITH 14 MeV NICKEL IONS TO A FLUENCE OF 2.5×10^{20} IONS/M^2 AT 525°C. SAMPLE WAS PREINJECTED WITH 1.5×10^{19} H_3^+/M^2 (500 APPM) AT 25°C.

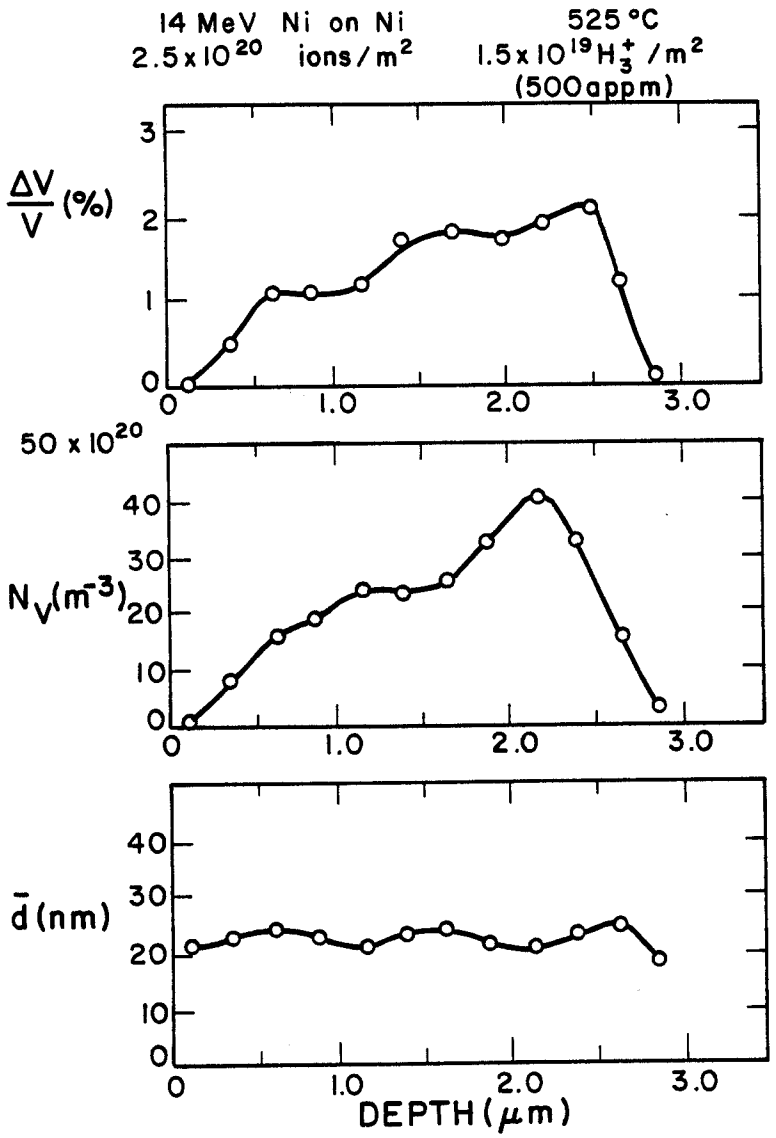

Fig. V-14. Swelling, void number density and mean void diameter vs. depth in hydrogen preinjected (1.5×10^{19} H_3^+/m^2) Ni irradiated at 525°C to a fluence of 2.5×10^{19} ions/m^2.

PREINJECTED HYDROGEN EFFECT IN SELF-ION IRRADIATED NICKEL

HIGH HYDROGEN FLUENCE

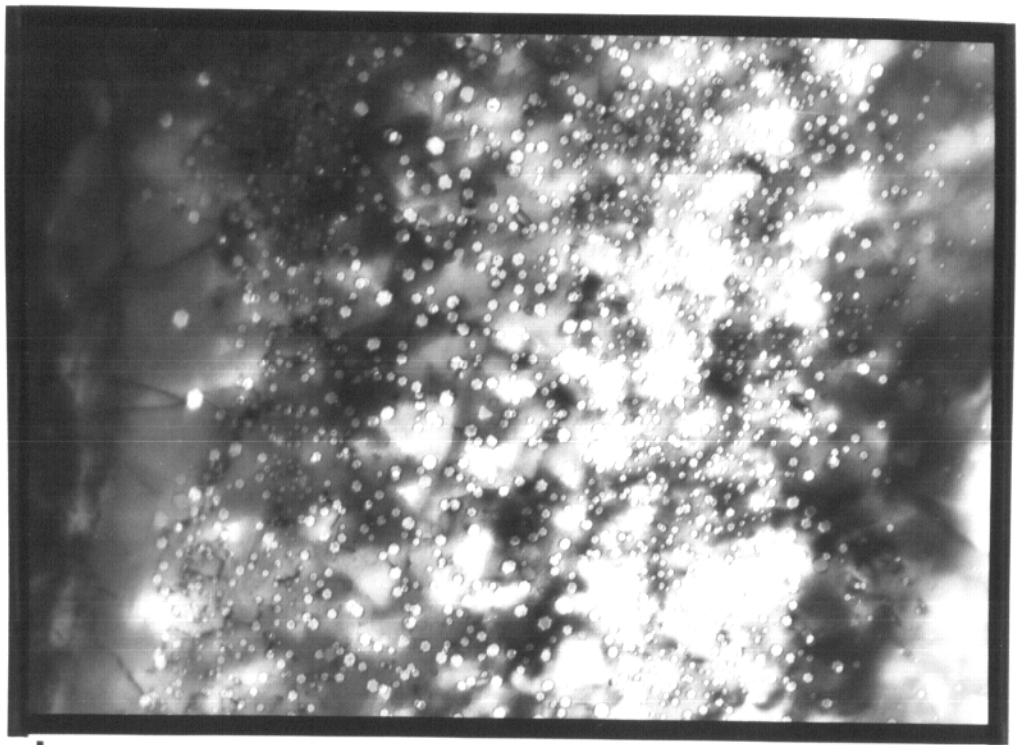

FIG. V-15. VOID MICROSTRUCTURE IN NICKEL IRRADIATED WITH 14 MeV NICKEL IONS TO A FLUENCE OF 2.5×10^{20} IONS/M^2 AT 525°C. SAMPLE WAS PREINJECTED WITH 3×10^{19} H_3^+/M^2 (1000 APPM) AT 25°C.

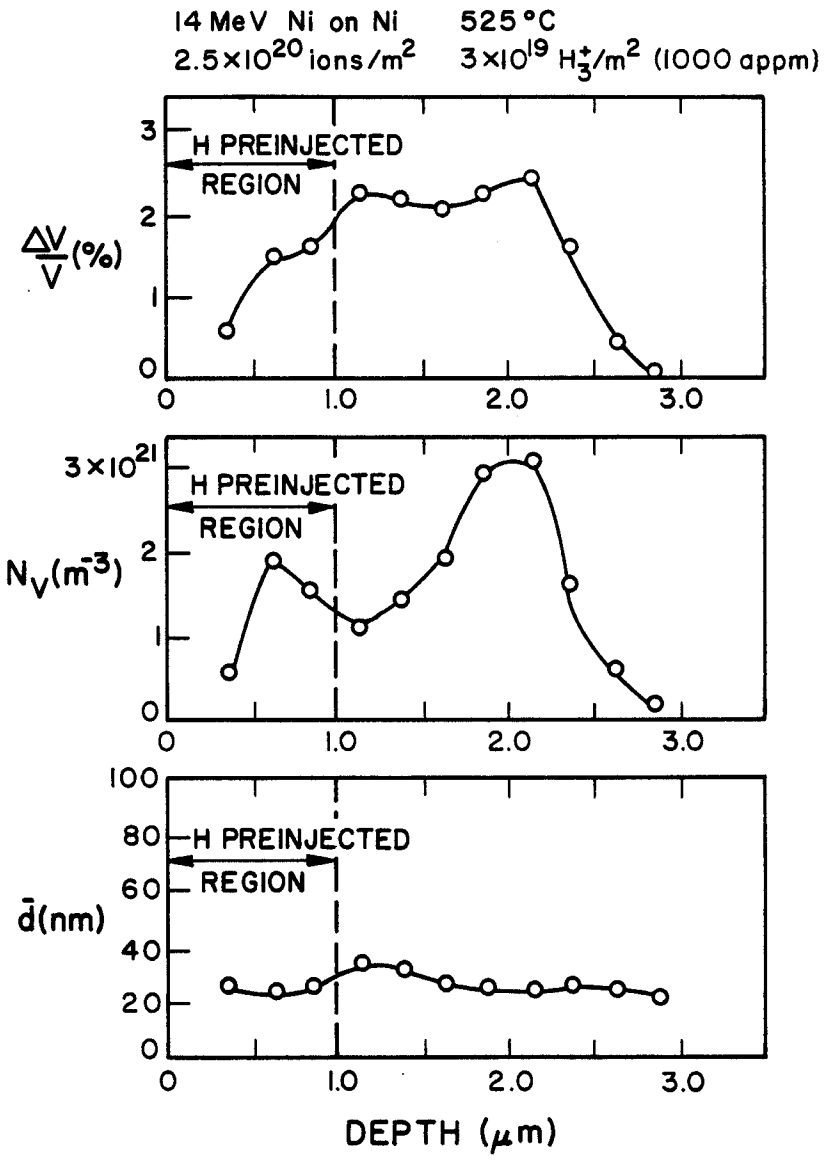

Fig. V-16. Swelling, void number density and mean void diameter vs. depth in hydrogen preinjected (3×10^{19} H_3^+/m^2) Ni irradiated at 525°C to a fluence of 2.5×10^{20} ions/m^2.

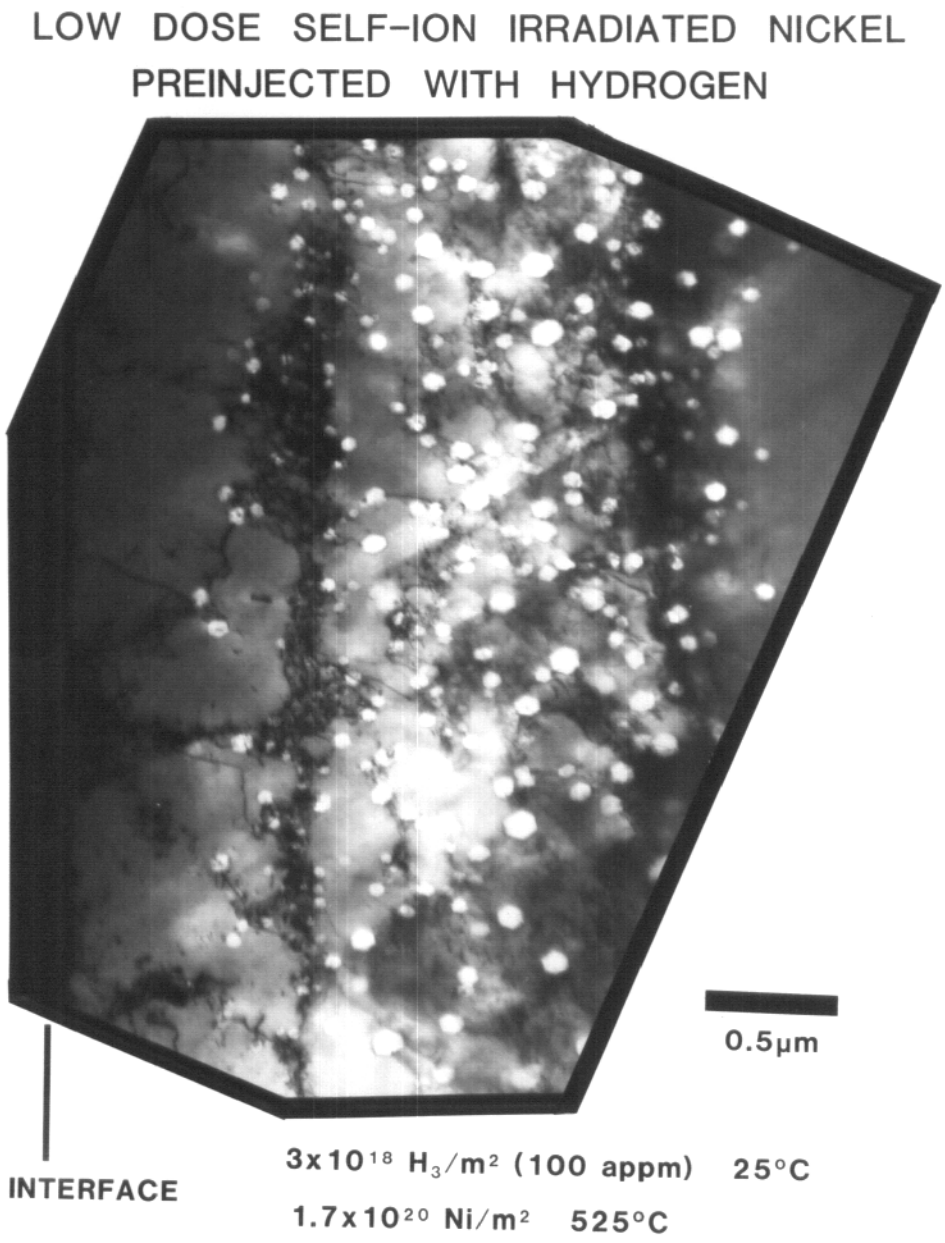

FIG. V-17. DAMAGE MICROSTRUCTURE PRODUCED IN SELF-ION IRRADIATED NICKEL IRRADIATED TO A FLUENCE OF 1.7×10^{20} IONS/M^2 AT 525°C. SAMPLE WAS PREINJECTED WITH 3×10^{18} H_3^+/M^2 (100 APPM) AT 25°C.

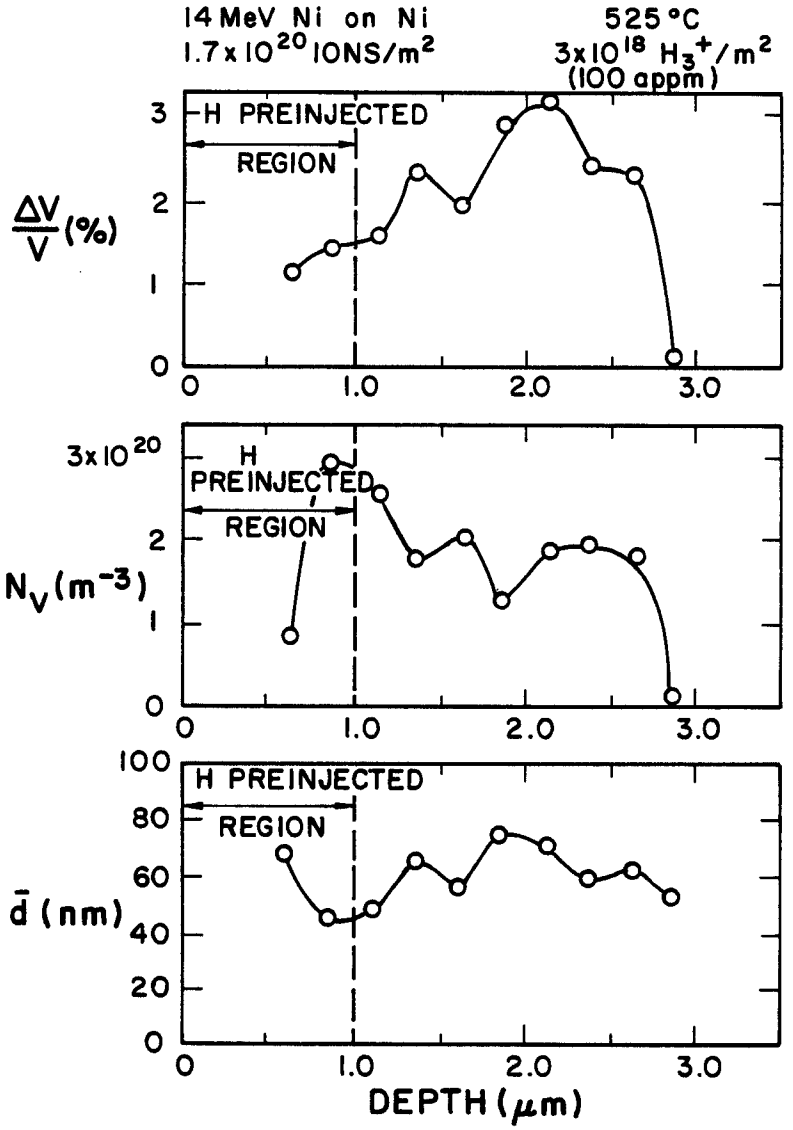

Fig. V-18. Swelling, void number density and mean void diameter vs. depth in hydrogen preinjected (3 x 10^{18} H_3^+/m^2) Ni irradiated at 525°C to a fluence of 1.7 x 10^{20} ions/m^2.

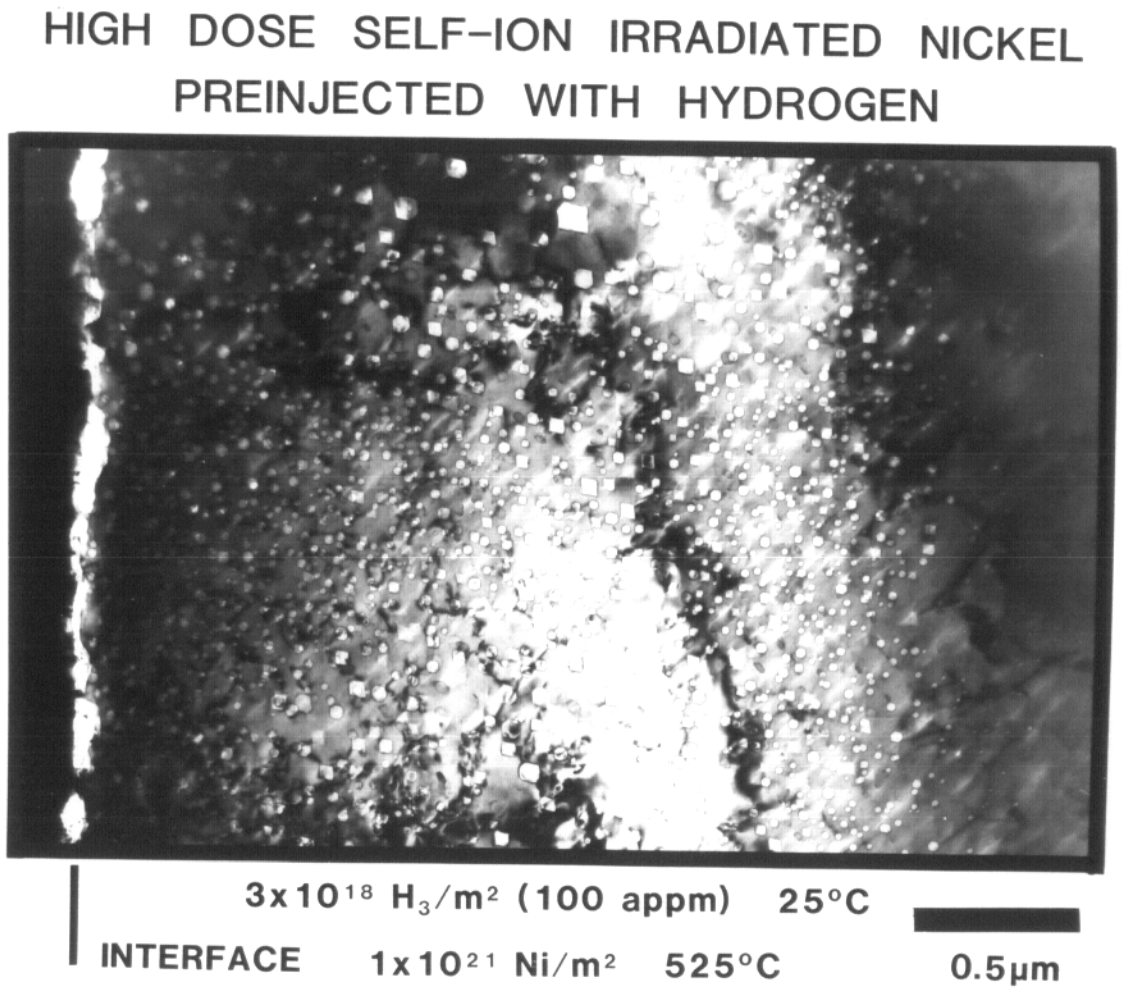

FIG. V-19. VOID MICROSTRUCTURE IN NICKEL IRRADIATED WITH 14 MEV NICKEL IONS TO A FLUENCE OF 1 x 10^{21} IONS/M^2 AT 525°C. SAMPLE WAS PREINJECTED WITH 3 x 10^{18} H_3^+/M^2 (100 APPM) AT 25°C.

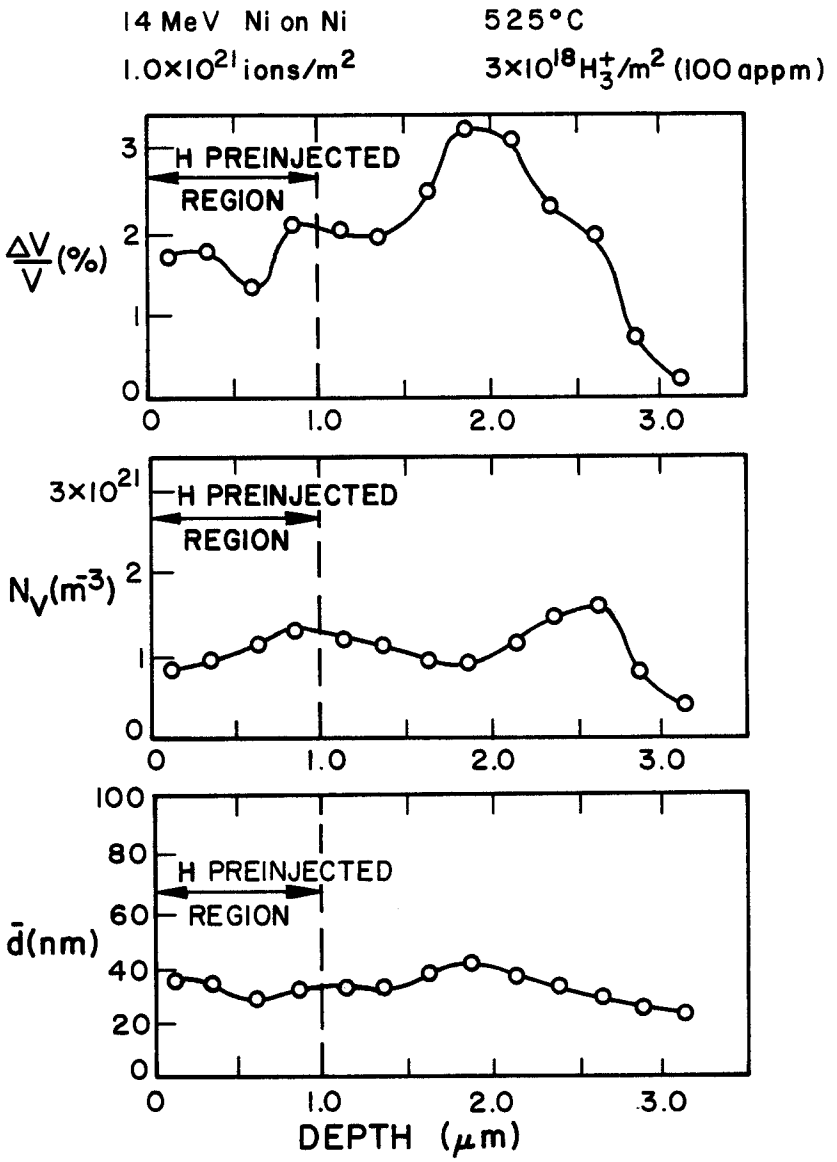

Fig. V-20. Swelling, void number density and mean void diameter vs. depth in hydrogen preinjected (3 x 10^{18} H_3^+/m^2) Ni irradiated at 525°C to a fluence of 1 x 10^{21} ions/m^2.

Further explanation of microstructural variations as a function of fluence will be presented in Chapter VI.

B.2 625°C Irradiations

Irradiations similar to the "hydrogen scan" completed at 525°C were also done at 625°C to allow for the study of possible temperature effects. Samples were irradiated with nickel ions to a fluence of 2.5×10^{20} ions/m^2 (7 dpa at 1 μm) after preinjection of 25°C with hydrogen with fluences of 3×10^{18} to 3×10^{19} H_3^+/m^2 (100 to 1000 appm injected). An increase in swelling with increasing hydrogen concentration was again noted in these 625°C irradiations.

The sample preinjected with hydrogen to a fluence of 3×10^{18} H_3^+/m^2 (100 appm) and irradiated with nickel ions to a damage level of 7 dpa at 1 μm is shown in Fig. V-21. This micrograph shows the formation of rather large voids which have a peak number density which corresponds to the peak damage region. The swelling produced is relatively low as shown in Fig. V-22. This is due to the low number density of relatively large voids.

The preinjection of 1.5×10^{19} H_3^+/m^2 (500 appm) prior to irradiation at the same conditions as the previous sample produces another increase in swelling. This is shown in Fig. V-23 and Fig. V-24. The micrograph of the 500 appm preinjected sample shows an increase in void number density compared to that in the 100 appm preinjected sample. However, the mean void diameter remained relatively constant at about 80 nm. These large diameter voids may indicate that there is very little hydrogen effect at 625°C and 500 appm preinjected

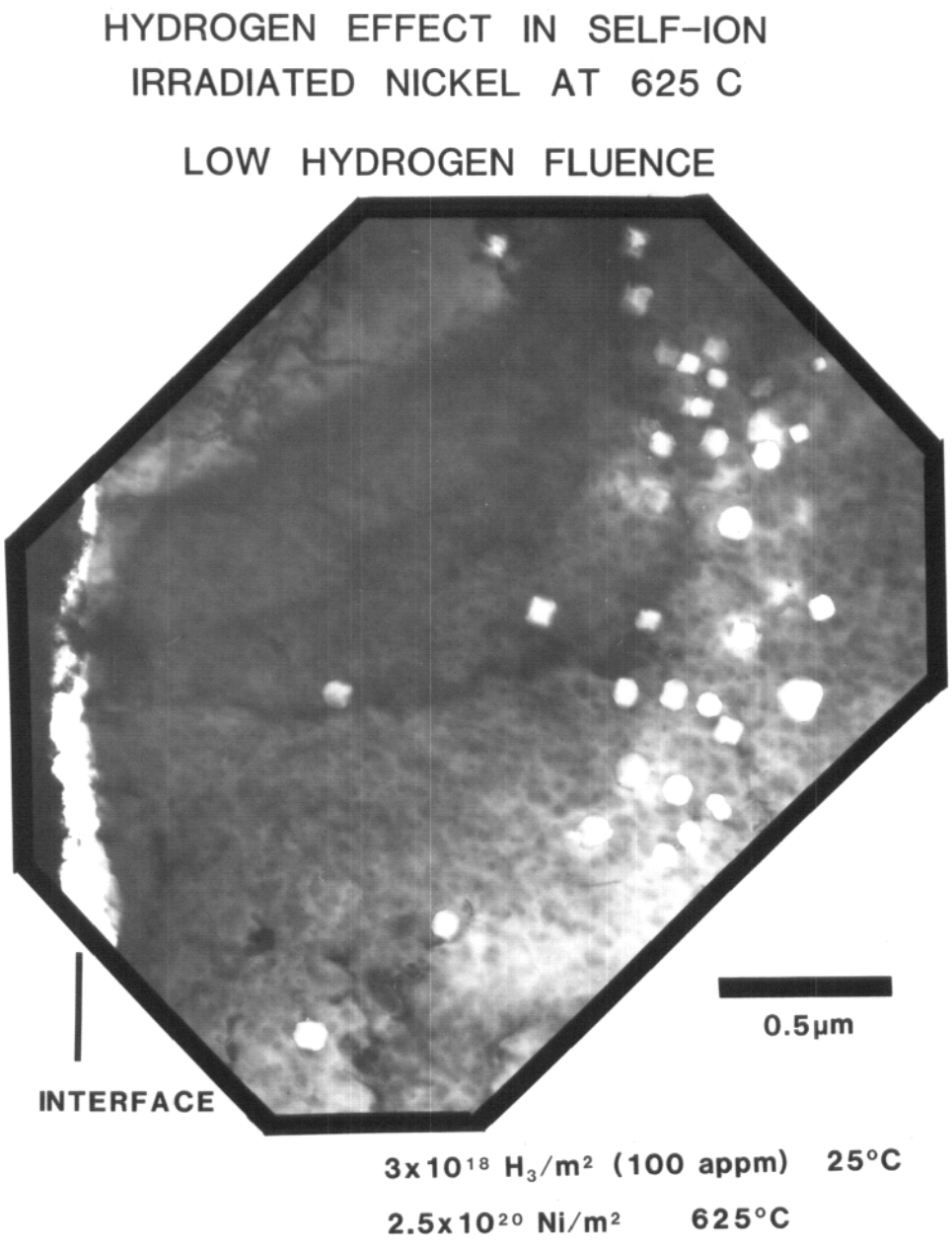

FIG. V-21. VOID FORMATION IN NICKEL IRRADIATED WITH 14 MeV NICKEL IONS TO A FLUENCE OF 2.5×10^{20} IONS/M^2 AT 625°C. SAMPLE WAS PREINJECTED WITH 3×10^{18} H_3^+/M^2 (100 APPM) AT 25°C.

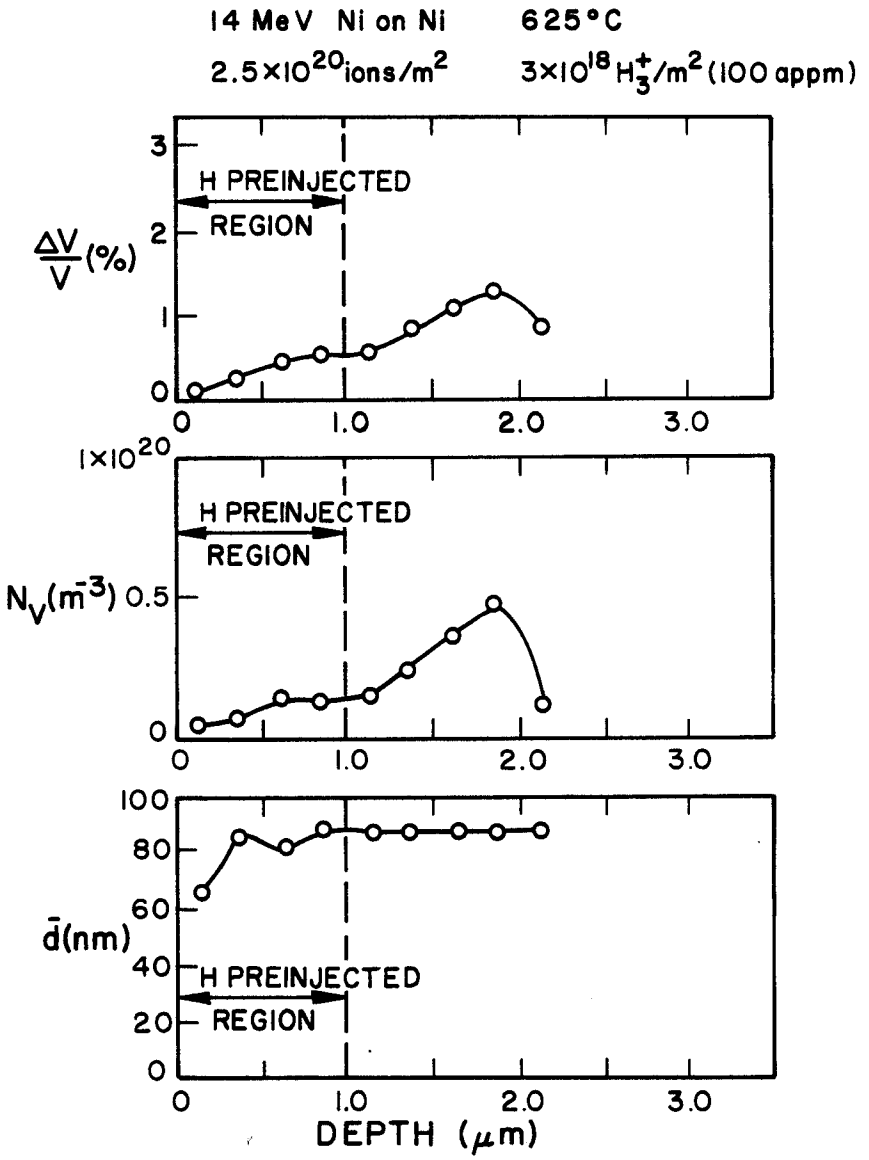

Fig. V-22. Swelling, void number density and mean void diameter vs. depth in hydrogen preinjected (3×10^{18} H_3^+/m^2) Ni irradiated at 625°C to a fluence of 2.5×10^{20} ions/m^2.

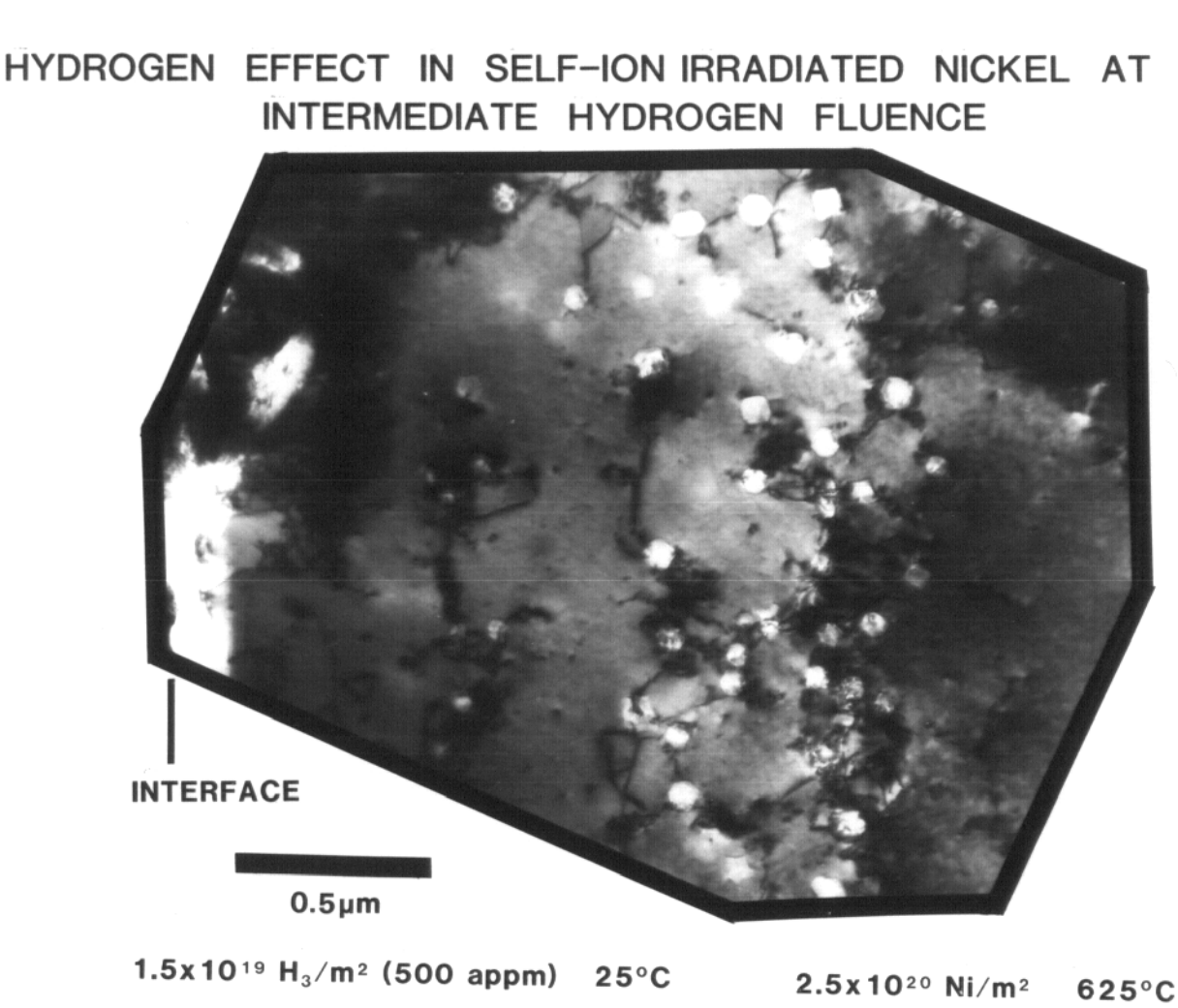

FIG. V-23. DAMAGE MICROSTRUCTURE PRODUCED IN NICKEL BY 14 MeV SELF-ION IRRADIATION TO A FLUENCE OF 2.5×10^{20} IONS/M^2 AT 625°C. SAMPLE WAS PREINJECTED WITH 1.5×10^{19} H_3^+/M^2 (500 APPM) AT 25°C.

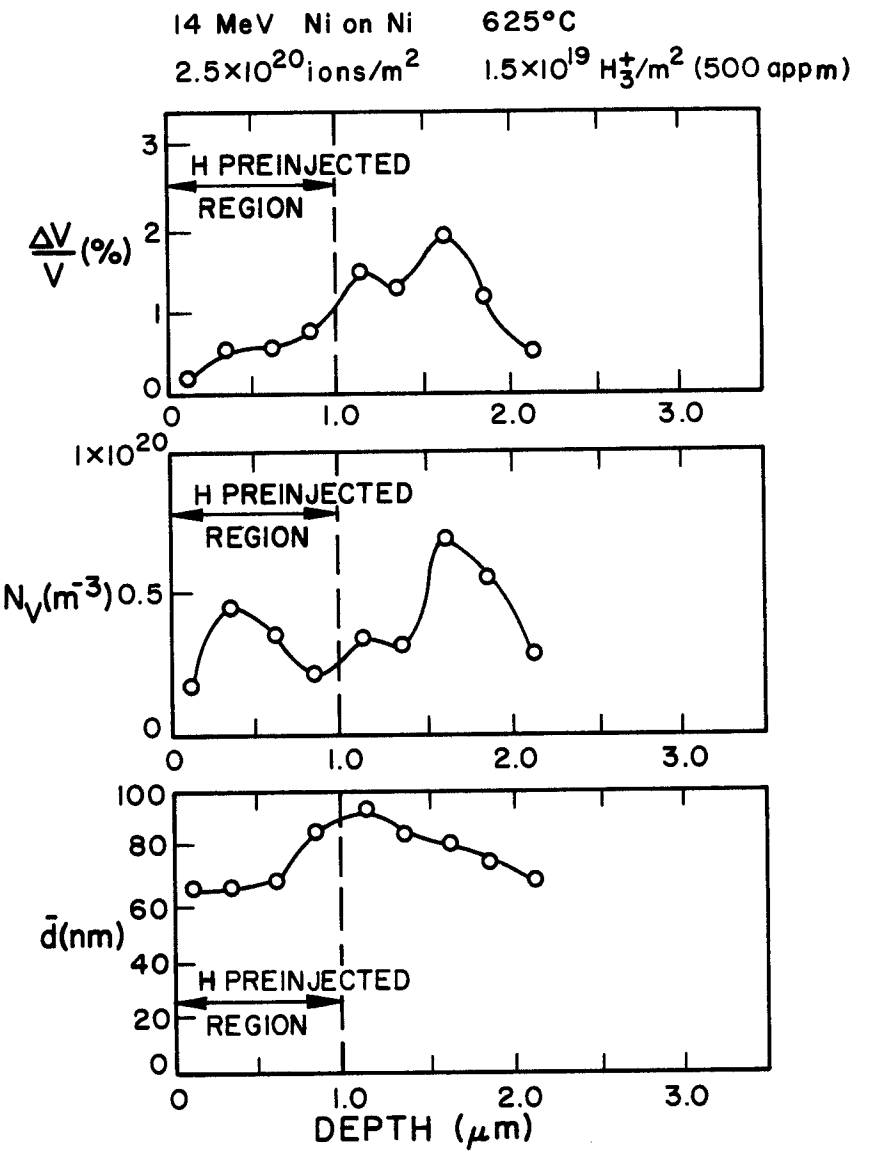

Fig. V-24. Swelling, void number density and mean void diameter vs. depth in hydrogen preinjected (1.5 x 10^{19} H_3^+/m^2) Ni irradiated at 625°C to a fluence of 2.5 x 10^{20} ions/m^2).

hydrogen since these diameters and number densities correspond well with the sample irradiated at 525°C (Fig. V-9) with no gas preinjection.

However, a dramatic increase in void number density was noted in the sample which was preinjected with hydrogen to a fluence of 3 x 10^{19} H_3^+/m^2 (1000 appm) and irradiated with nickel ions to a fluence of 2.5 x 10^{20} ions/m^2 at 625°C (Fig. V-25). The swelling increased slightly over the previous sample with a sharp increase in the void number density which was tempered by a reduction in the mean void diameter as seen in Fig. V-26. This may indicate the first true hydrogen effect observed in the 625°C irradiations which will be more evident in the following chapter.

One final hydrogen preinjected sample was irradiated at 625°C to a higher fluence in an attempt to discern the effects of higher dose. Figure V-27 shows the void microstructure produced in nickel which was preinjected with hydrogen to a fluence of 3 x 10^{18} H_3^+/m^2 (100 appm) and irradiated with nickel ions to a fluence of 5 x 10^{20} ions/m^2 (13 dpa at 1 μm). When compared to a sample with similar hydrogen preinjection which was irradiated to one-half the dose (Fig. V-21), an increase in void number density and a decrease in mean void diameter is noted. These variations result in an increase in swelling as noted in Fig. V-28.

C. Preinjected Helium Effects

Helium is another interstitial gas atom which is known to effect formation of cavities in metals in an irradiation environment. In

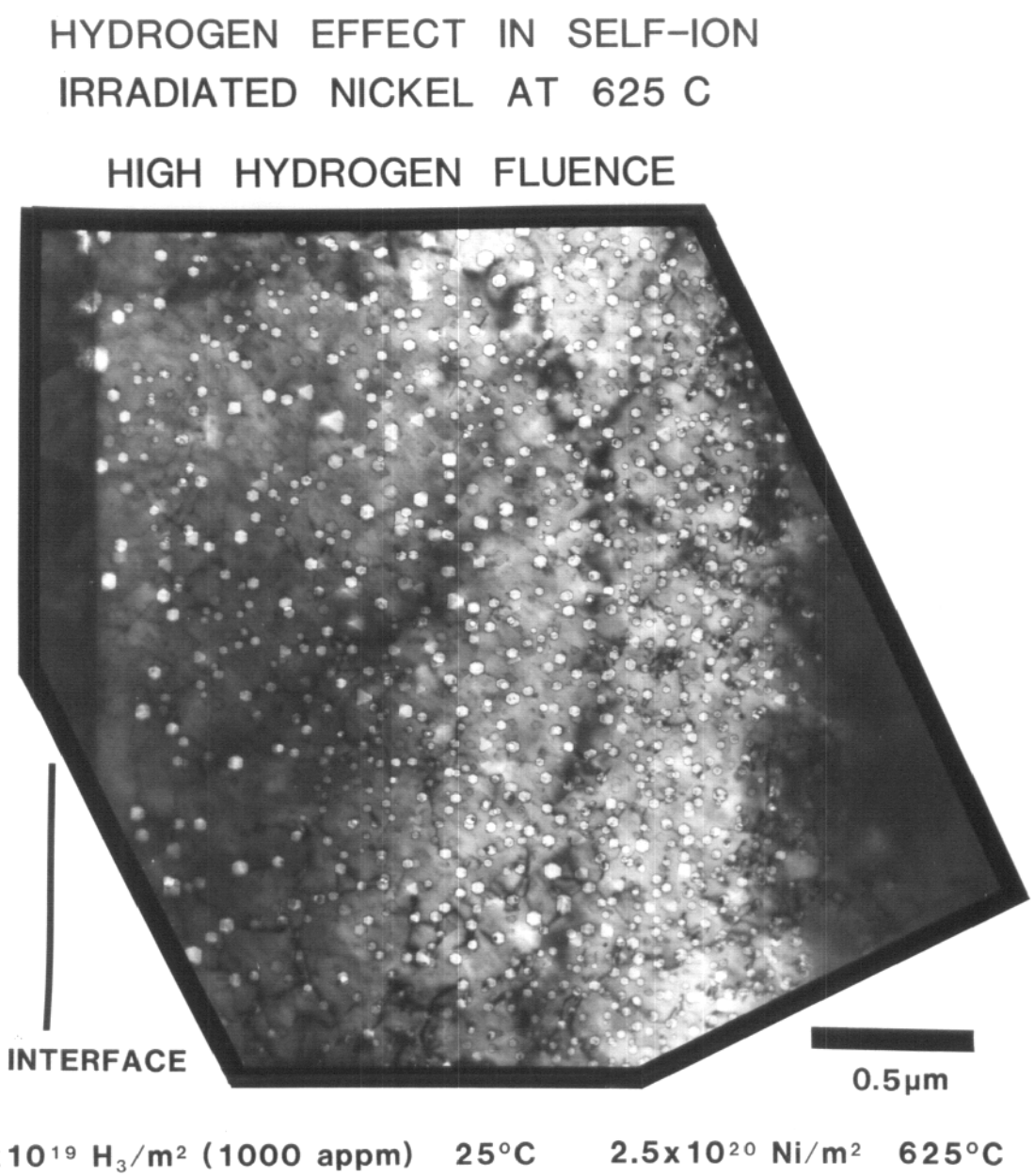

FIG. V-25. ENHANCED VOID FORMATION IN NICKEL IRRADIATED WITH 14 MeV NICKEL IONS AT 625°C TO A FLUENCE OF 2.5×10^{20} IONS/M^2. SAMPLE WAS PREINJECTED WITH 3×10^{19} H_3^+/M^2 (1000 APPM) AT 25°C.

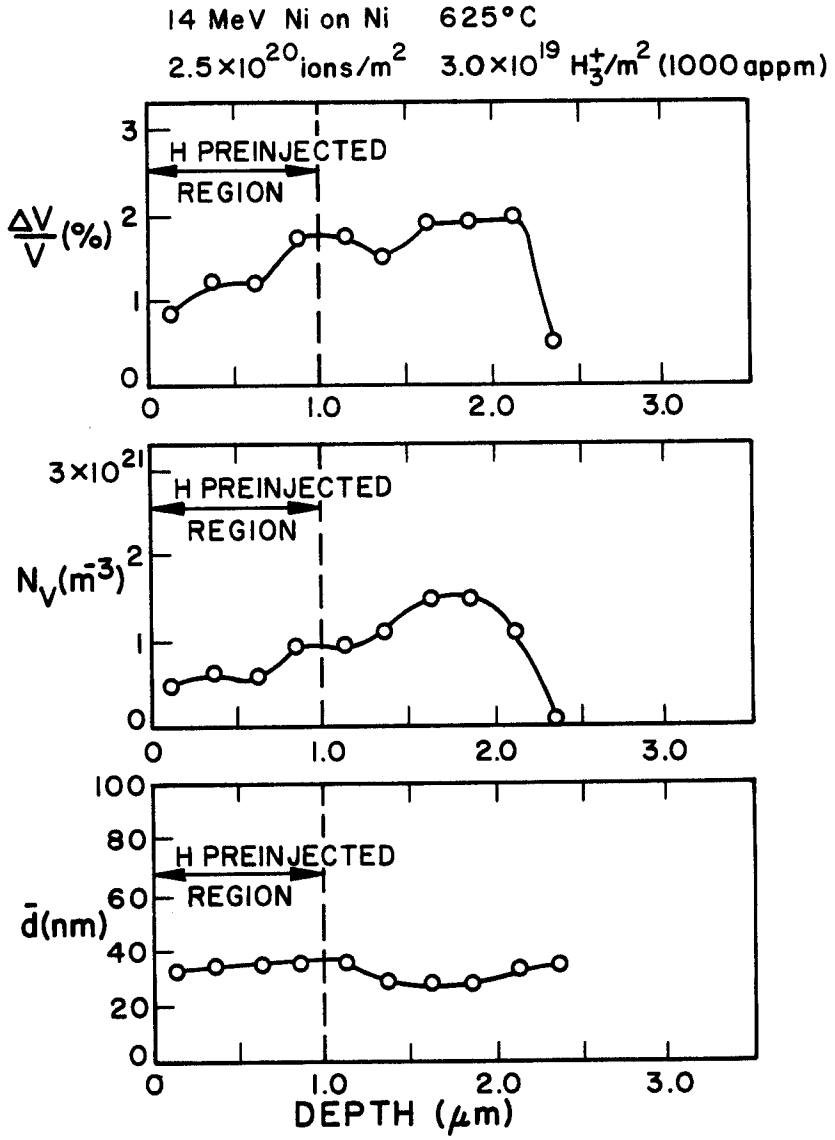

Fig. V-26. Swelling, void number density and mean void diameter vs. depth in hydrogen preinjected (3 x 10^{19} H_3^+/m^2) Ni irradiated at 625°C to a fluence of 2.5 x 10^{20} ions/m^2.

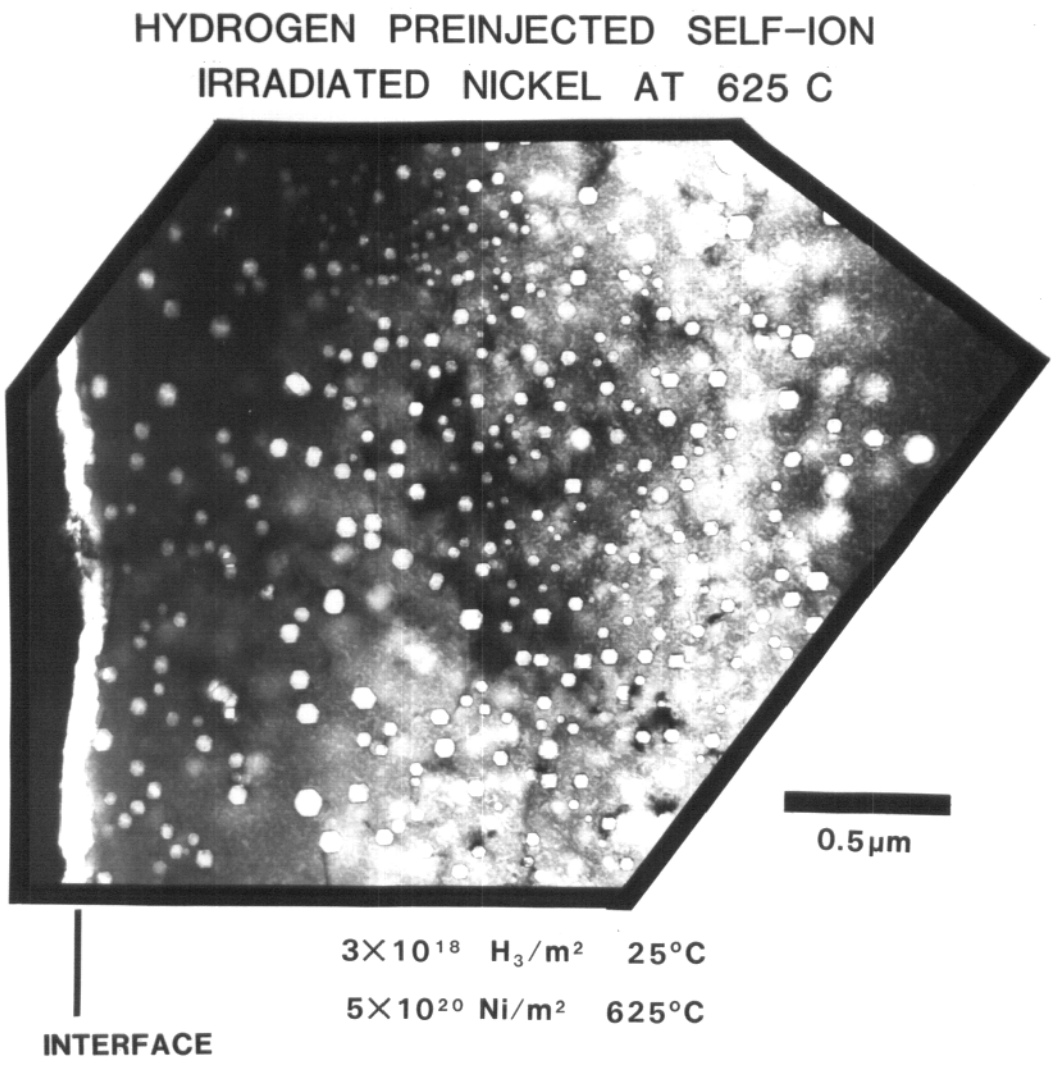

FIG. V-27. VOID MICROSTRUCTURE PRODUCED IN NICKEL PREINJECTED WITH 3 x 10^{18} H_3^+/M^2 (100 APPM) AT 25°C AND IRRADIATED WITH 14 MeV NICKEL IONS TO A FLUENCE OF 5 x 10^{20} IONS/M^2 AT 625°C.

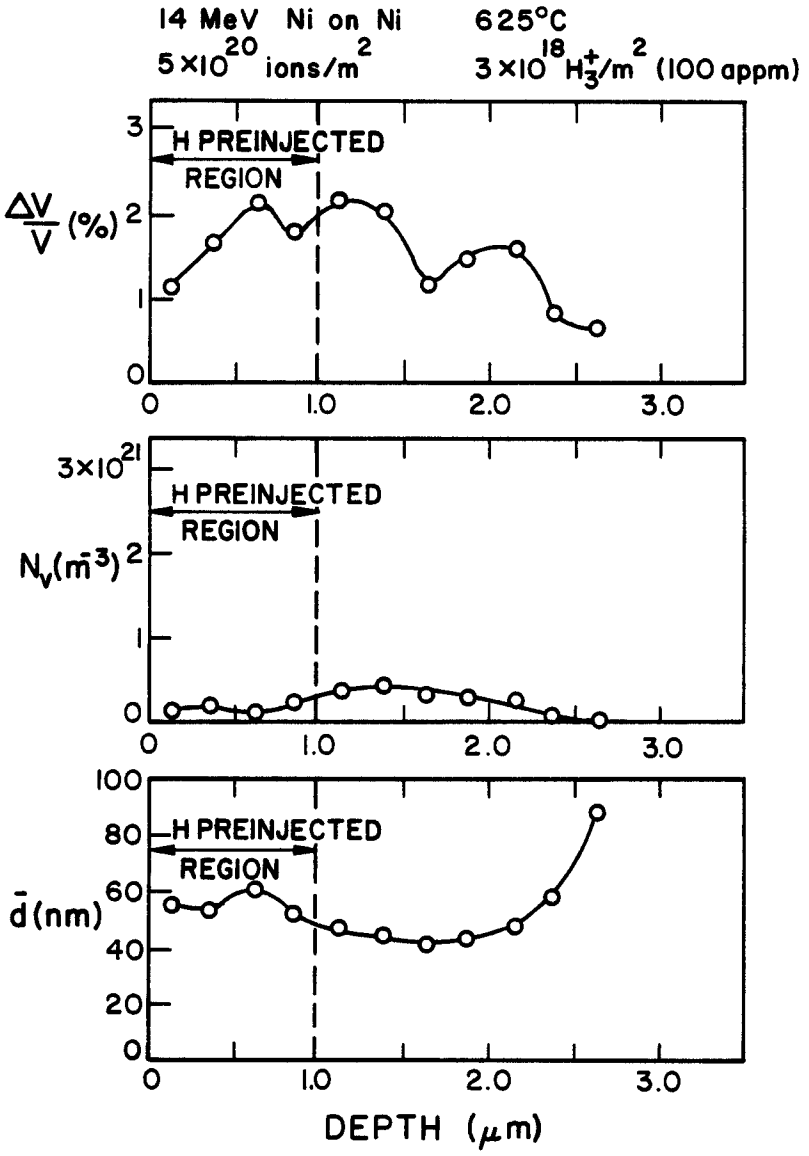

Fig. V-28. Swelling, void number density and mean void diameter vs. depth in hydrogen preinjected (3×10^{18} H_3^+/m^2) Ni irradiated at 625°C to a fluence of 5×10^{20} ions/m^2.

this study nickel samples were preinjected at 25°C with helium using two different methods. Initially a helium beam of varied energy (200-700 keV) was used to preinject a nickel sample with a uniform concentration of helium (100-600 appm) over a range which extended from the surface of the sample to a depth of 1.25 μm. Subsequent irradiation with nickel ions produced a notable reduction of visible voids in this region. However, it was not possible to completely differentiate the effects of helium preinjection from surface effects near the interface with this implantation method. Hence, another technique was utilized. This technique employed a monoenergetic beam of helium (700 keV) to implant nickel with peak concentrations of helium ranging from 65 to 3250 appm He at a depth of between 1 μm and 1.25 μm. The results of irradiations completed after preinjection with these methods is presented in the following sections.

C.1. Uniform Helium Preinjection Using Varied Beam Energies

Samples uniformly preinjected with helium to a depth of 1.25 μm at 25°C were irradiated with nickel ions at temperatures of 525°C and 625°C to fluences of 1-2.5 x 10^{20} ions/m^2 (3-7 dpa at 1 μm). All samples showed some suppression of void formation over the preinjected area with a marked increase in void number density at the end of range of the injected helium ions.

Irradiations at 625°C after uniform helium injection produced almost complete suppression of visible voids. Figure V-29 shows a nickel sample preinjected with 100 appm He to a depth of 1.25 μm at 25°C and irradiated with nickel ions to a fluence of 1 x 10^{20}

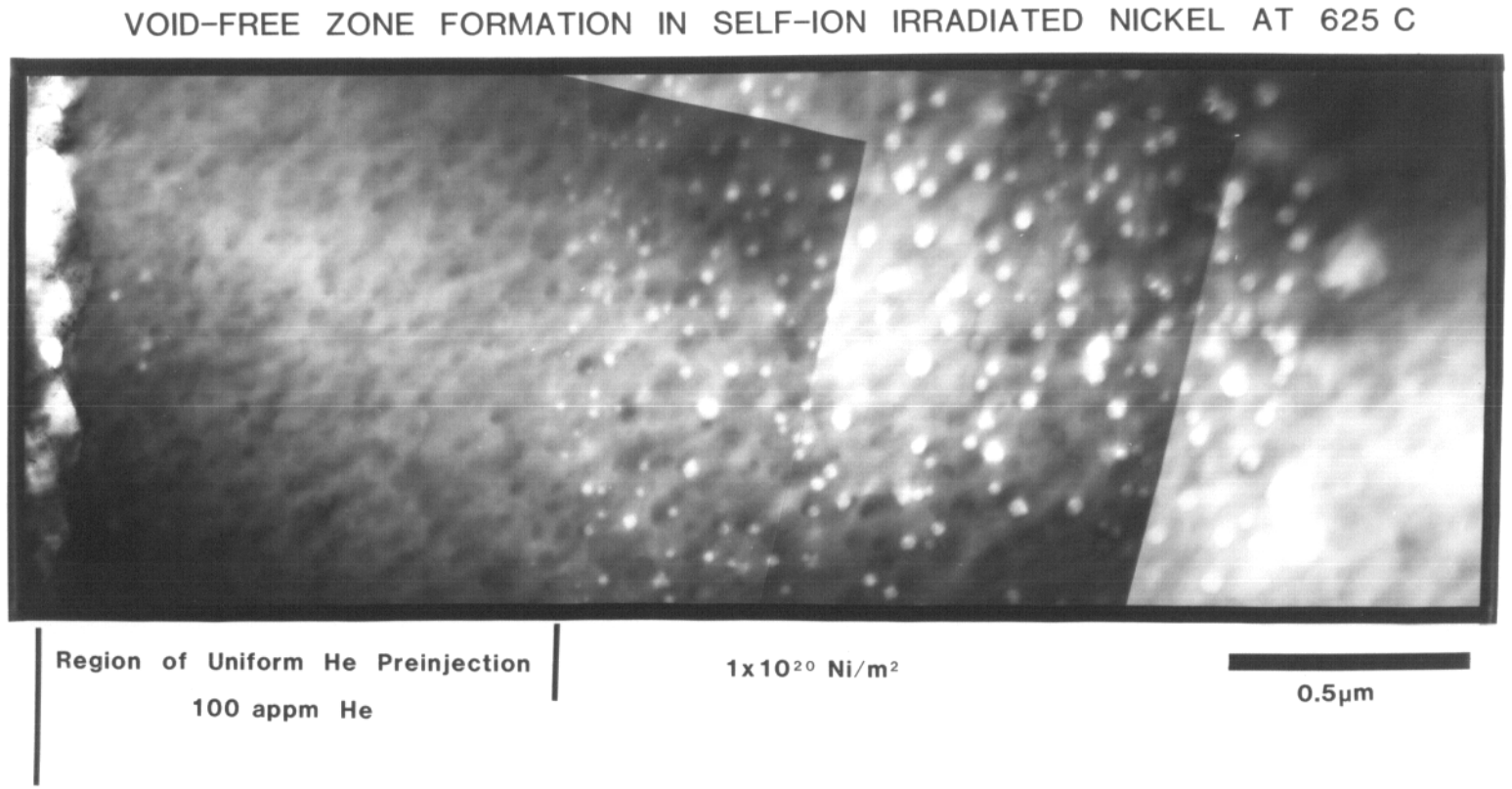

Fig. V-29. Void-free zone formation in nickel uniformly preinjected with 100 appm He at 25°C and irradiated with Ni ions to a fluence of 1×10^{20} ions/m^2 at 625°C

ions/m^2. Figure V-30 shows almost complete suppression of swelling due to the "apparent" reduction in void number density. As will be noted in subsequent samples this reduction in swelling is probably due to enhanced nucleation of cavities which are below the resolution limit of current electron microscopes.

An increase in the amount of preinjected helium to a uniform concentration of 600 appm completely suppresses visible void formation and swelling as shown in Fig. V-31 and Fig. V-32. This is probably due to even further enhancement of very small cavities made possible by the increased helium concentration. Comparison of the data presented in Figs. V-30 and V-32 shows that beyond the range of the preinjected He, the void number density and mean void diameter are approximately the same. This confirms that the helium is not very mobile during the irradiation.

Uniform helium preinjection was also completed on nickel samples irradiated at 525°C. A suppression of void formation was noted for a relatively low damage level with increased visible void formation at a higher damage level. A void-free zone was noted in nickel preinjected with 100 appm He at 25°C and irradiated with nickel ions to a fluence of 1 x 10^{20} ions/cm^2 (3 dpa at 1 μm) at 525°C. Figure V-33 shows this void free zone extends to a depth of slightly more than 1 μm and contains only dislocations. Figure V-34 gives the swelling and void microstructure data for the damage produced beyond the end of range of the preinjected helium.

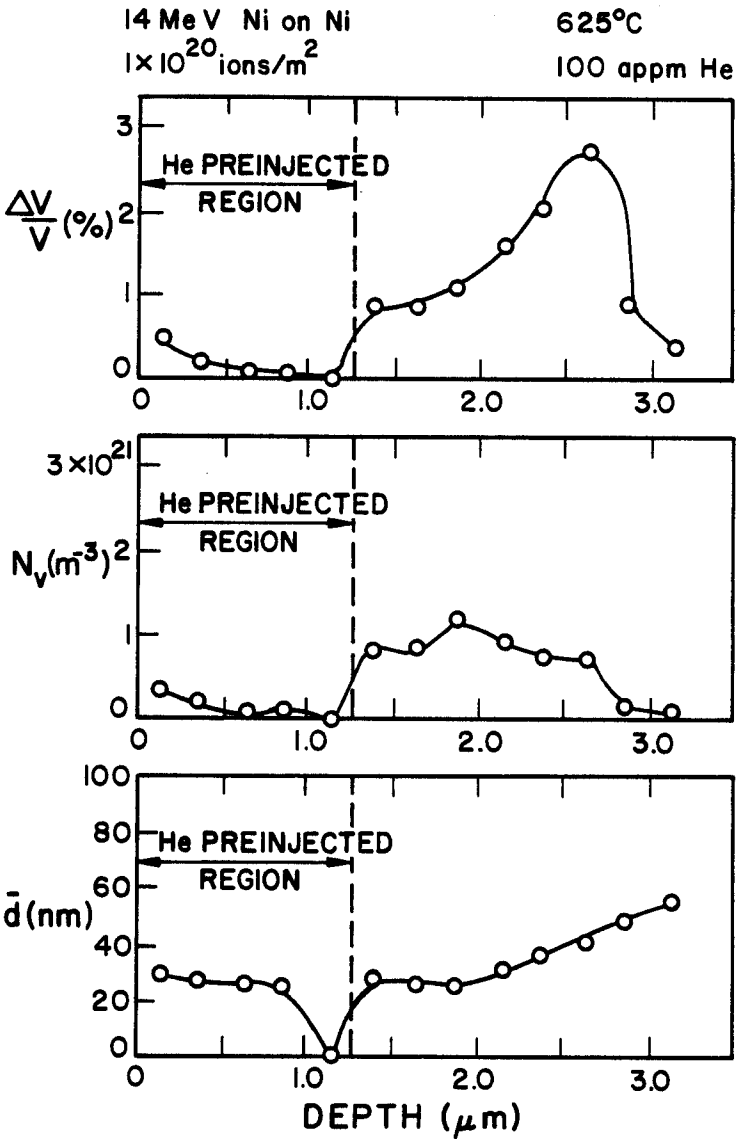

Fig. V-30. Swelling, void number density and mean void diameter vs. depth in helium preinjected (100 appm) Ni irradiated at 625°C to a fluence of 1 x 10^{20} ions/m^2.

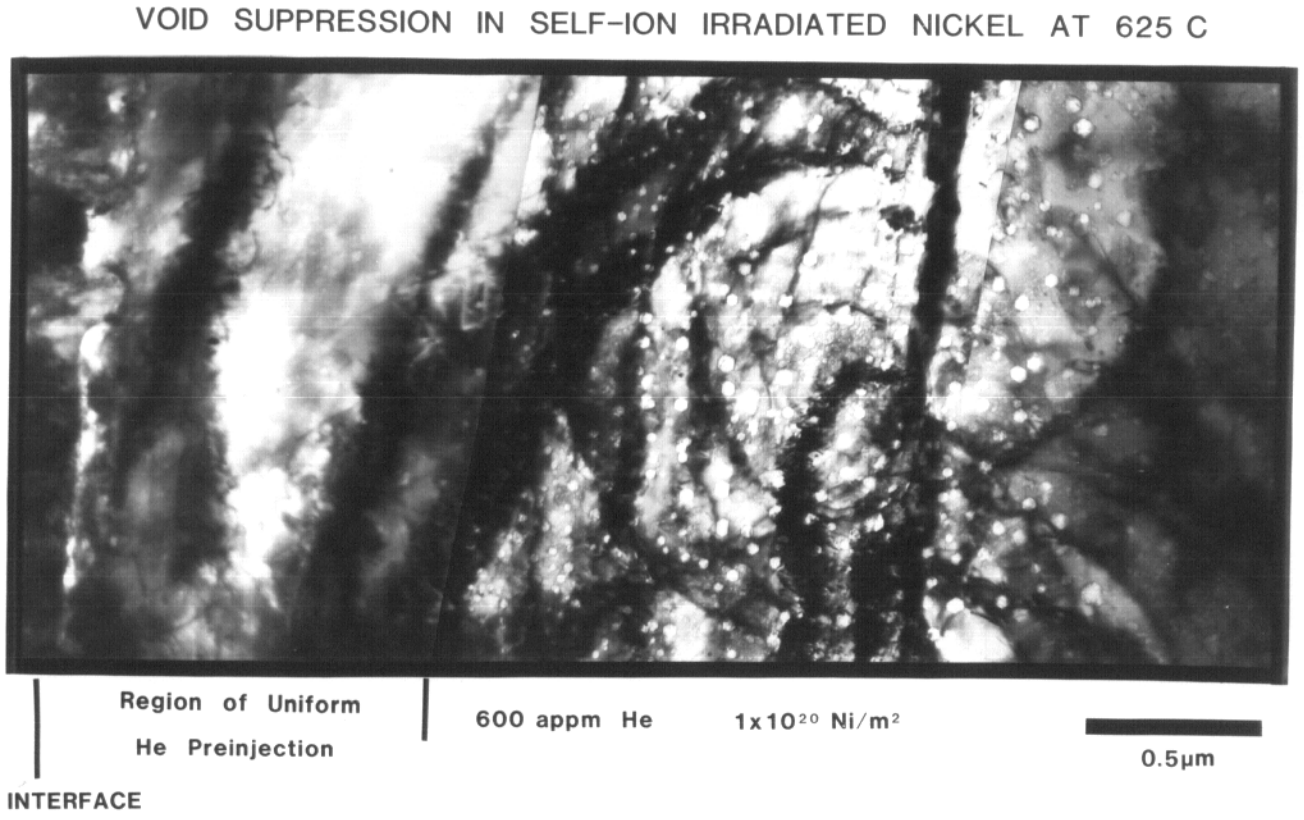

Fig. V-31. Void formation suppression in Ni preinjected with 600 appm He at 25°C and irradiated with Ni ions to a fluence of 1×10^{20} ions/m^2 at 625°C

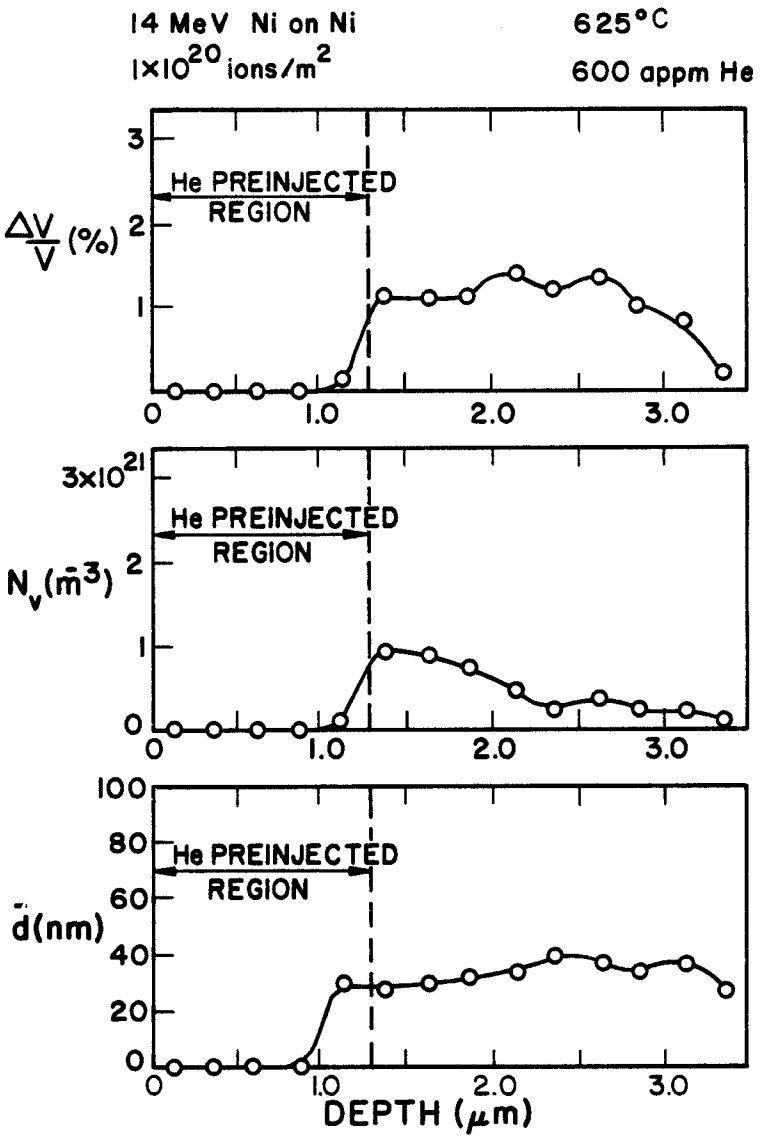

Fig. V-32. Swelling, void number density and mean void diameter vs. depth in helium preinjected (600 appm) Ni irradiated at 625°C to a fluence of 1 x 10^{20} ions/m^2.

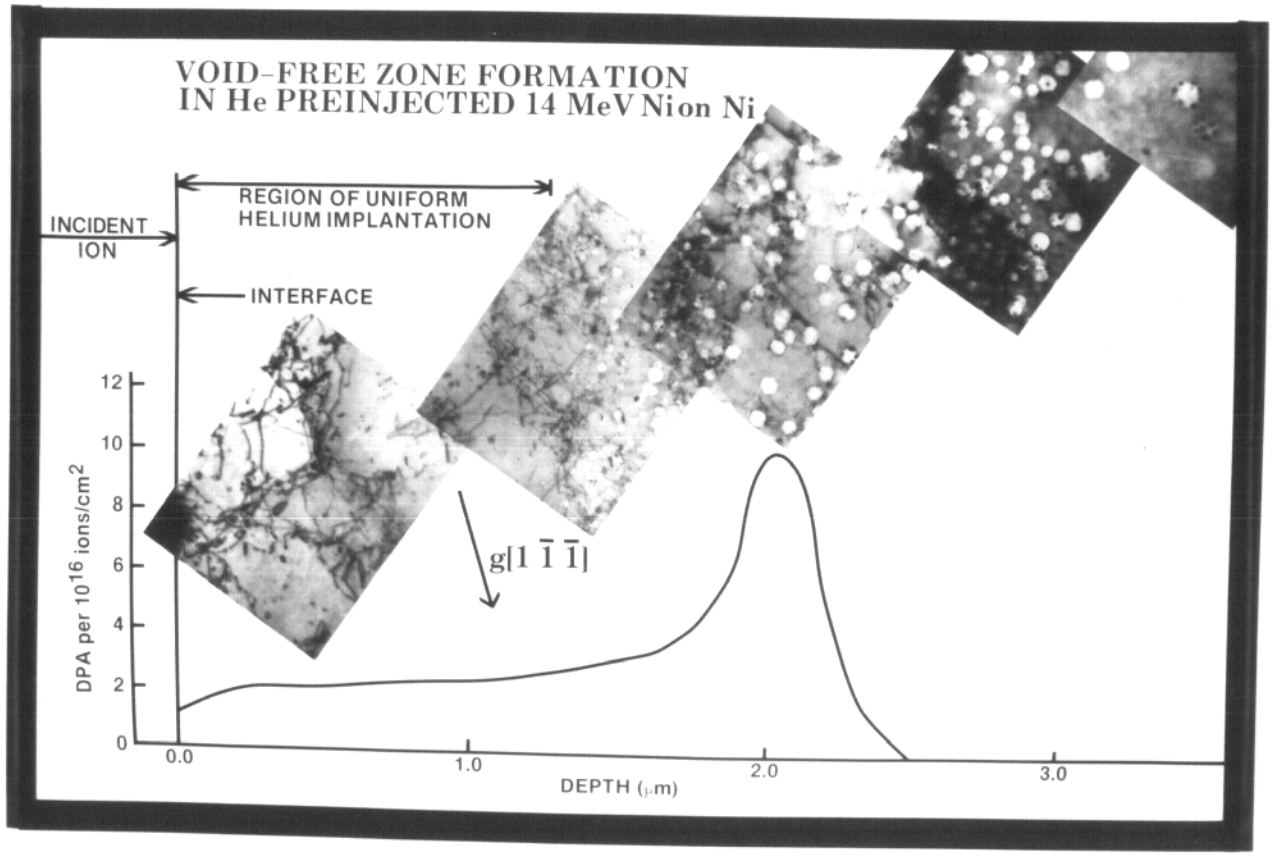

FIG. V-33. VOID-FREE ZONE FORMATION IN NICKEL UNIFORMLY PREINJECTED WITH 100 APPM HE TO A DEPTH OF 1.25 μM AT 25°C AND IRRADIATED WITH 14 MEV NICKEL IONS TO A FLUENCE OF 1 x 10^{20} IONS/M^2 AT 525°C.

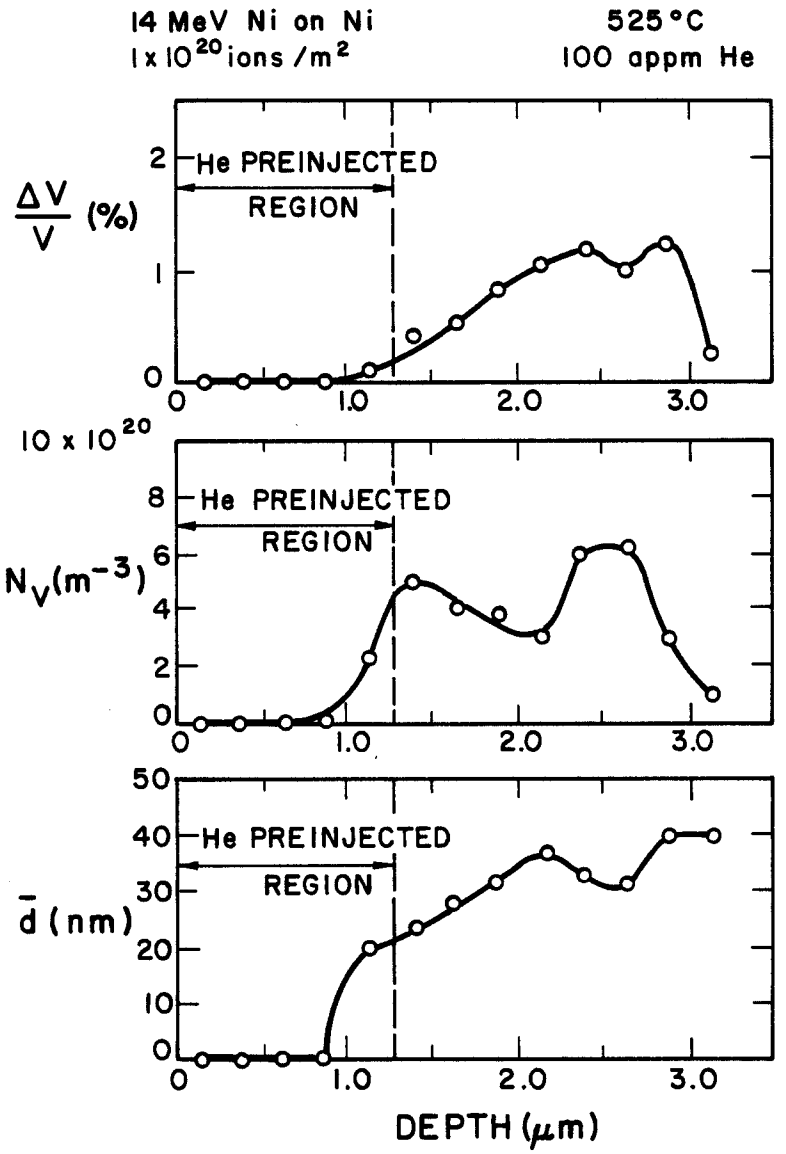

Fig. V-34. Swelling, void number density and mean void diameter vs. depth in helium preinjected (100 appm) Ni irradiated at 525°C to a fluence of 1 x 10^{20} ions/m^2.

At a higher damage level (7 dpa at 1 μm), the suppression of void formation over the preinjected region is not as evident as shown in Fig. V-35. The data presented in Fig. V-36 shows a marked increase in void number density and swelling when compared to Fig. V-34. The micrograph in Fig. V-35 shows a surface effect in this particular sample. The enhanced void formation near the surface is most likely due to a reduction in the helium concentration in that region due to escape by diffusion to the surface. The depth of this affected region is also an indication of how far past the preinjection range the helium may diffuse during the course of the irradiation.

C.2. Monoenergetic Helium Preinjection

Nickel samples which were preinjected with 700 keV He ions at room temperature all showed some swelling suppression within the preinjected zone. This suppression was the result of copious nucleation of sub-microscopic cavities in this region. This swelling suppressed zone is readily evident in Fig. V-37. Near the interface side of the suppressed zone there is a high number density of small voids, as shown in Fig. V-38. Beyond the suppressed zone a smaller number density of large voids are present. It should be noted that in this sample and the following sample, the helium preinjected region appears at a depth of less than 1 μm. This is due to problems which arose during the plating process in post-irradiation sample preparation. In an effort to insure plating adherence, the time period of the strike was increased from 3 sec to about 6 sec. This increased

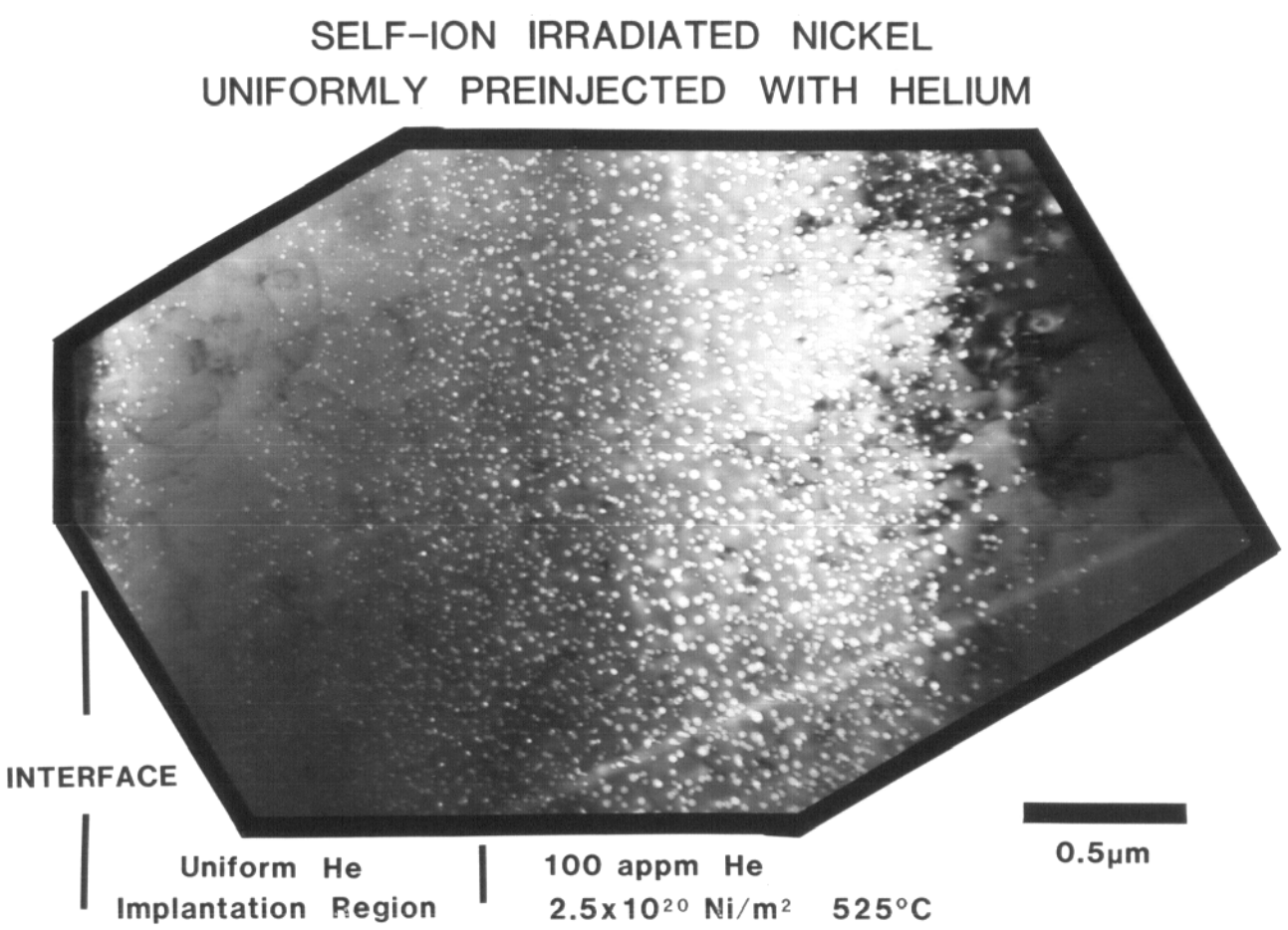

FIG. V-35. VOID SUPPRESSION IN NICKEL PREINJECTED WITH 100 APPM HE TO A DEPTH OF 1.25 μM AT 25°C AND IRRADIATED WITH 14 MEV NICKEL IONS TO A FLUENCE OF 2.5 x 10^{20} IONS/M^2 AT 525°C.

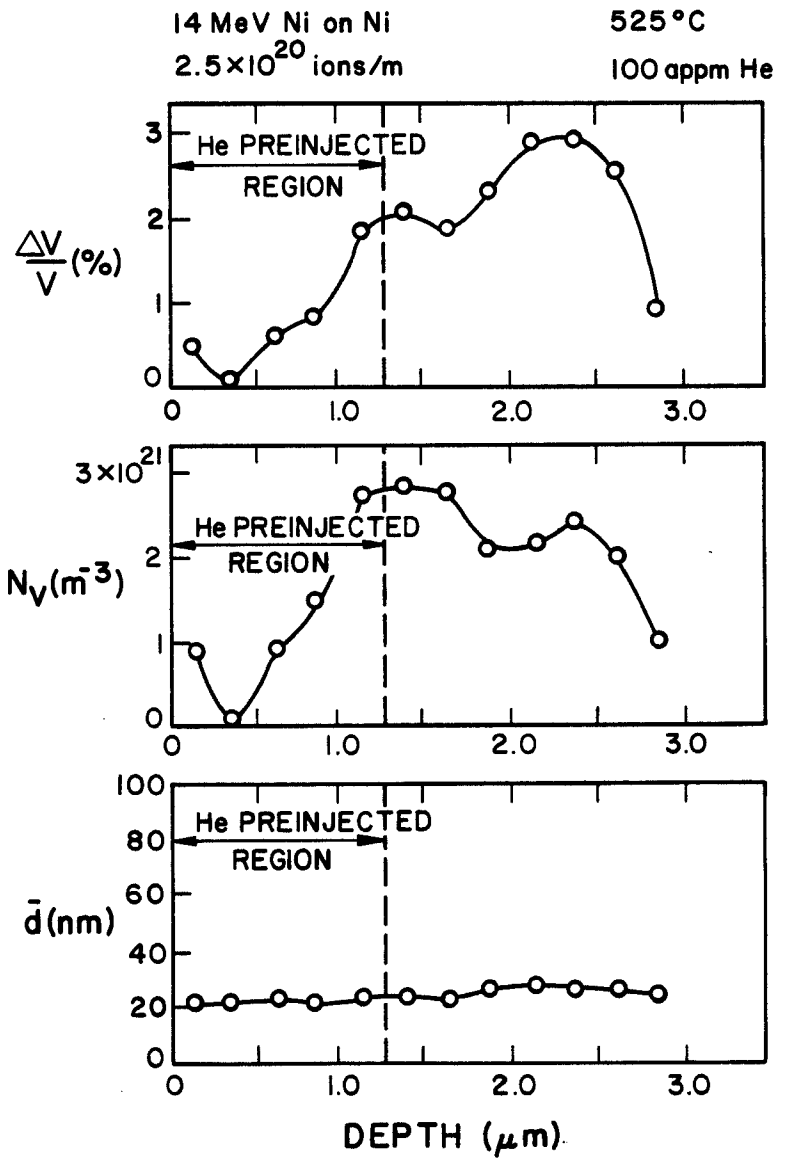

Fig. V-36. Swelling, void number density and mean void diameter vs. depth in helium preinjected (100 appm) Ni irradiated at 525°C to a fluence of 2.5 x 10^{20} ions/m^2.

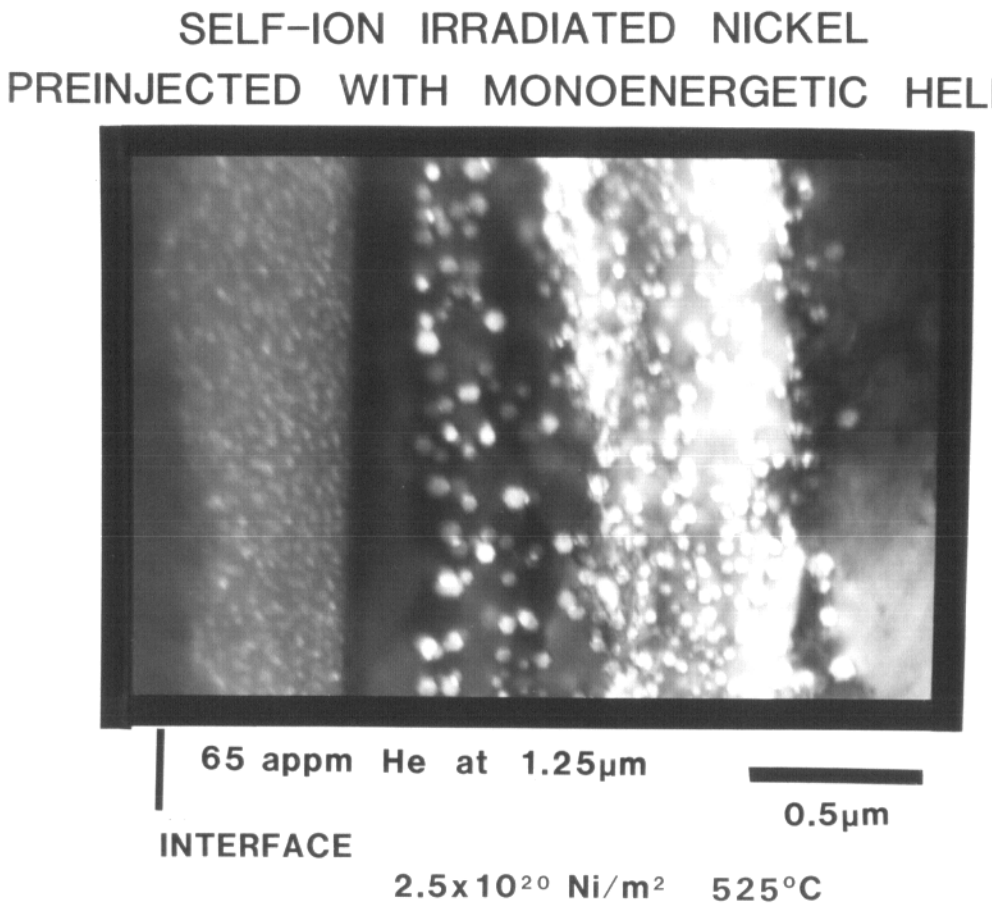

FIG. V-37. VOID FORMATION IN NICKEL PREINJECTED AT 25°C WITH A MONO-ENERGETIC (700 KEV) He^+ BEAM TO PRODUCE A CONCENTRATION OF 65 APPM HE AT A DEPTH OF 1.0 TO 1.25 μM. SAMPLE WAS IRRADIATED WITH 14 MEV NICKEL IONS TO A FLUENCE OF 2.5×10^{20} IONS/M^2 AT 525°C.

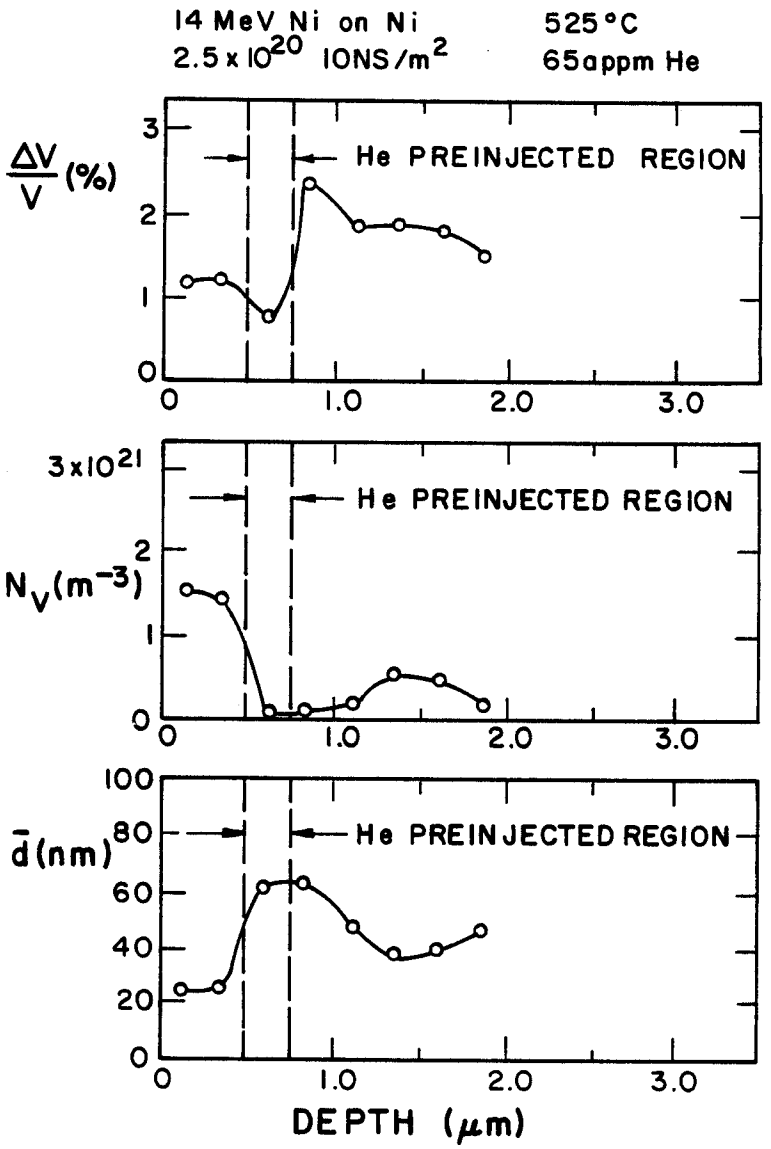

Fig. V-38. Swelling, void number density and mean void diameter vs. depth in helium preinjected (65 appm) Ni irradiated at 525°C to a fluence of 2.5 x 10^{20} ions/m^2. Note the shift in the He preinjected region 0.5 μm toward the sample surface to account for additional surface removed during the strike.

time not only removed the surface oxide layer but, unfortunately, also removed part of the damage region. In the case of this sample 0.5 μm of surface was removed. This was determined by a calibration experiment at the same strike conditions using optical interference microscopy techniques. However, since the helium preinjection region is so apparent in this sample and subsequent ones, the data presented can easily show the helium effects.

It would be expected that irradiation to a higher dose would produce increased swelling while increasing preinjected helium concentration may reduce observable swelling. The void microstructure shown in Fig. V-39 tend to support these expectations. This nickel sample was preinjected with helium to a concentration of 650 appm at 1.25 μm. However, due to a malfunction in the digital pyrometer during the preinjection, the sample temperature was allowed to reach at least 120°C. This sample was subsequently irradiated at 525°C with nickel ions to a fluence of 5×10^{20} ions/m^2 (13 dpa at 1 μm). The swelling and other void data presented in Fig. V-40 shows a slight dip in swelling at the preinjected region and a more uniform void diameter throughout the irradiated zone. This is indicative of helium diffusion at the higher temperature of the preinjection.

The most dramatic evidence of swelling suppression by helium preinjection is offered by the sample shown in Fig. V-41. This specimen was preinjected with helium to a concentration of 650 appm at a depth of 1.25 μm at 25°C. It was then irradiated with nickel ions at 525°C to a fluence of 1×10^{21} ions/m^2 (27 dpa at 1 μm). A

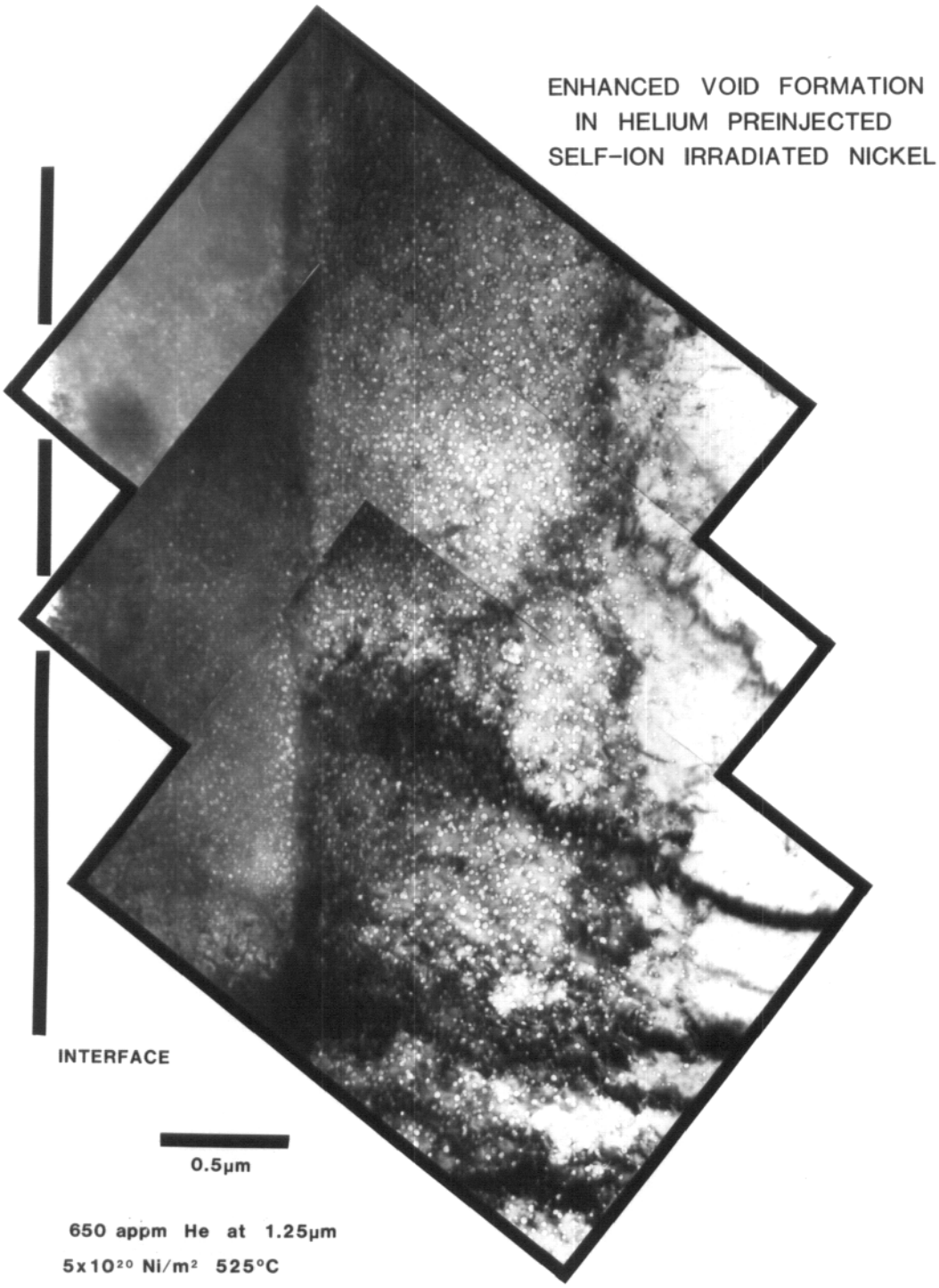

Fig. V-39. Enhanced void formation in Ni preinjected with 700 keV He at 120°C to a concentration of 650 appm He at 1.0-1.25 μm and irradiated with Ni ions to a fluence of 5×10^{20} ions/m² at 525°C

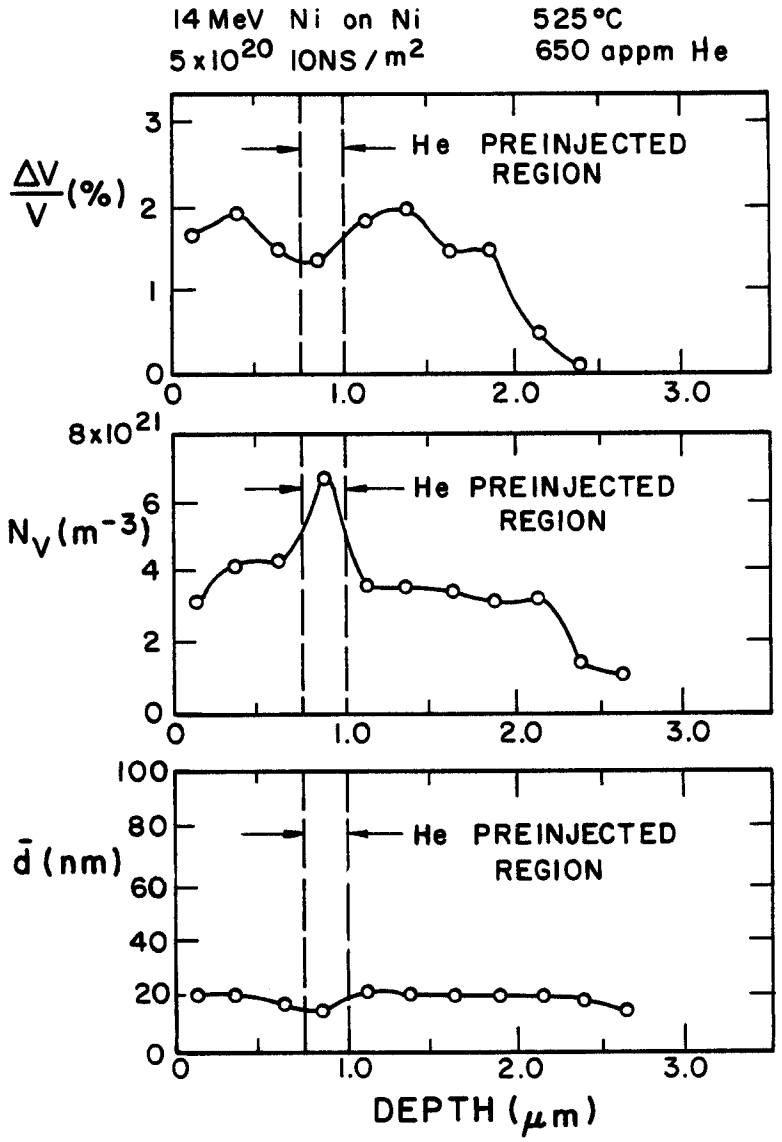

Fig. V-40. Swelling, void number density and mean void diameter vs. depth in helium preinjected (650 appm) Ni irradiated at 525°C to a fluence of 5 x 10^{20} ions/m^2. Note shift in the He preinjected region 0.25 μm toward the sample surface to account for additional surface removed during the strike.

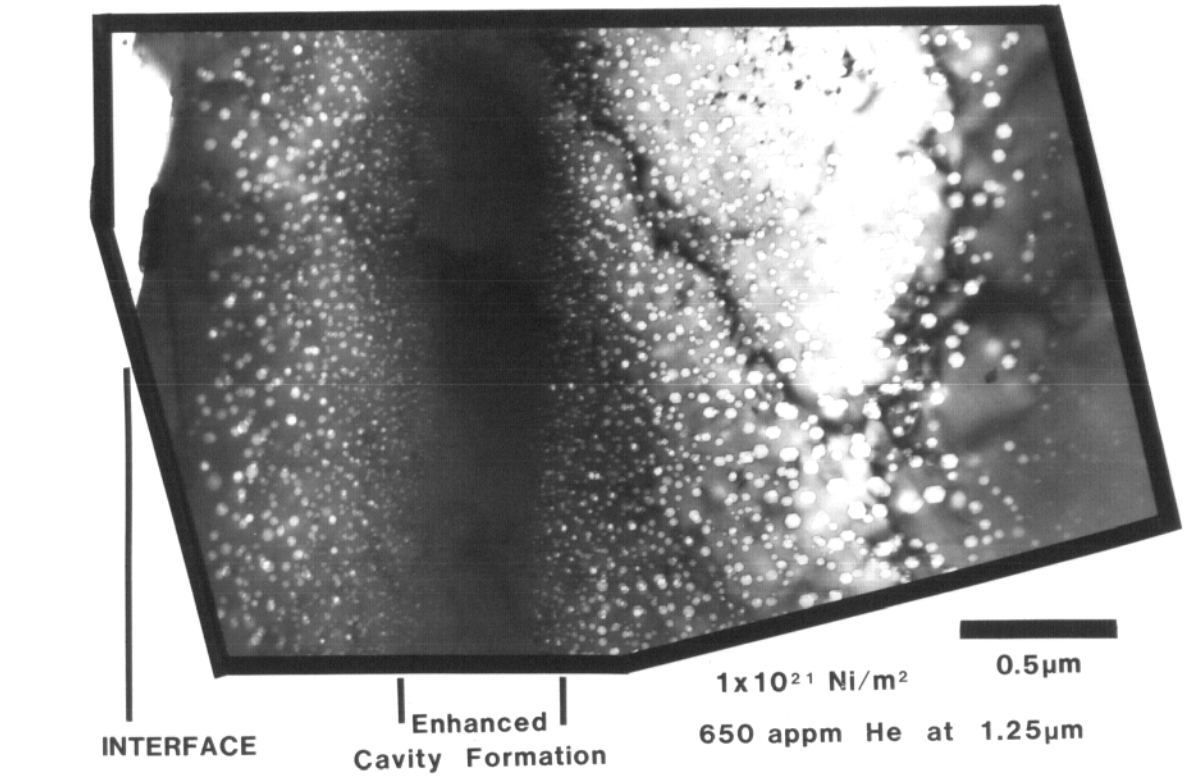

FIG. V-41. VOID SUPPRESSION IN NICKEL PREINJECTED WITH 650 APPM HE AT 1.0 TO 1.25 μM AT 25°C AND SUBSEQUENTLY IRRADIATED WITH 14 MEV NICKEL IONS TO A FLUENCE OF 1×10^{21} IONS/M^2 AT 525°C.

band of swelling suppression is readily visible over the preinjected region. This is due to enhanced formation of small cavities (4.5 nm) in this region as shown in Fig. V-42. This enhanced cavity nucleation with associated decreases in mean void diameter and swelling will be further illustrated and discussed in the following chapter.

The final helium preinjected sample containing 3250 appm He at a depth of 1.25 μm was implanted at 50°C and irradiated with nickel ions at 525°C to a fluence of 2.5 x 10^{20} ions/m^2 (7 dpa at 1 μm). Figure V-43 shows a region of enhanced cavity formation corresponding to the helium preinjected region. The mean diameter of cavities in this region (6 nm), is slightly larger than the diameter (4.5 nm) of the cavities formed in the comparable region of the sample preinjected with 650 appm He and irradiated to 27 dpa at 1 μm. Helium bubble formation may be responsible for the decrease in swelling noted in the He preinjected region shown in Fig. V-44.

D. Results Summary

A summary of the results presented in the previous sections is given in Table V-3. This table includes the dose, swelling at 1 μm, peak swelling, line dislocation density and loop density. Discussions of these results are presented in Chapter VI.

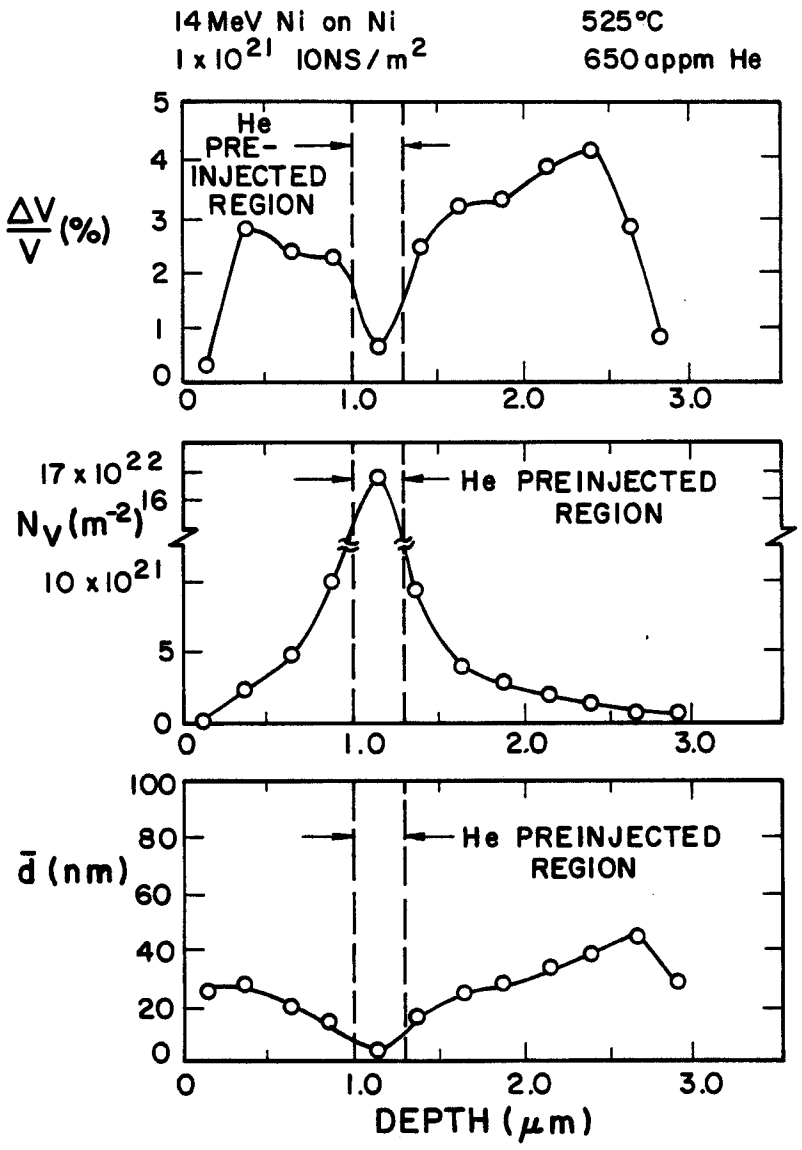

Fig. V-42. Swelling, void number density and mean void diameter vs. depth in helium preinjected (650 appm) Ni irradiated at 525°C to a fluence of 1 x 10^{21} ions/m^2.

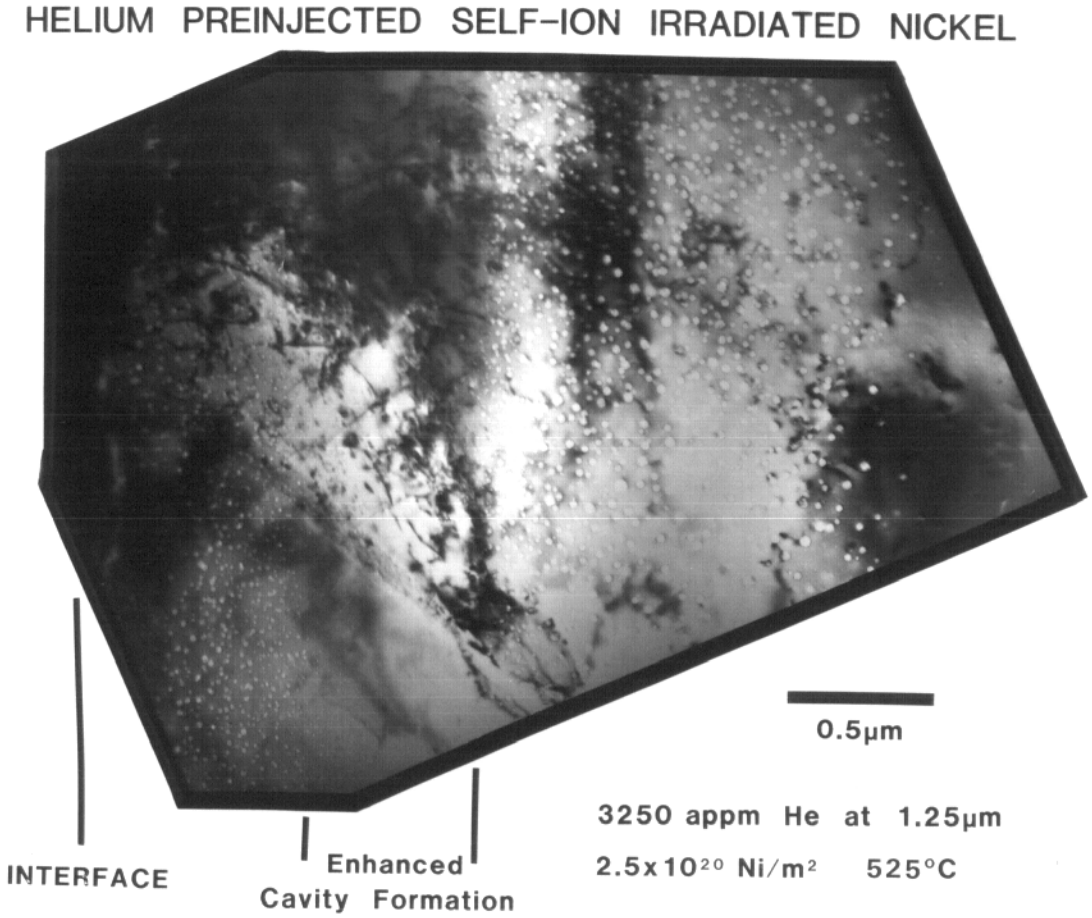

FIG. V-43. SUPPRESSION OF VOID FORMATION IN NICKEL PREINJECTED WITH 700 KEV HE IONS TO PRODUCE A CONCENTRATION OF 3250 APPM HE AT A DEPTH OF 1.0 TO 1.25 μM. SAMPLE WAS THEN IRRADIATED WITH 14 MEV NICKEL IONS TO A FLUENCE OF 2.5×10^{20} IONS/M^2 AT 525°C.

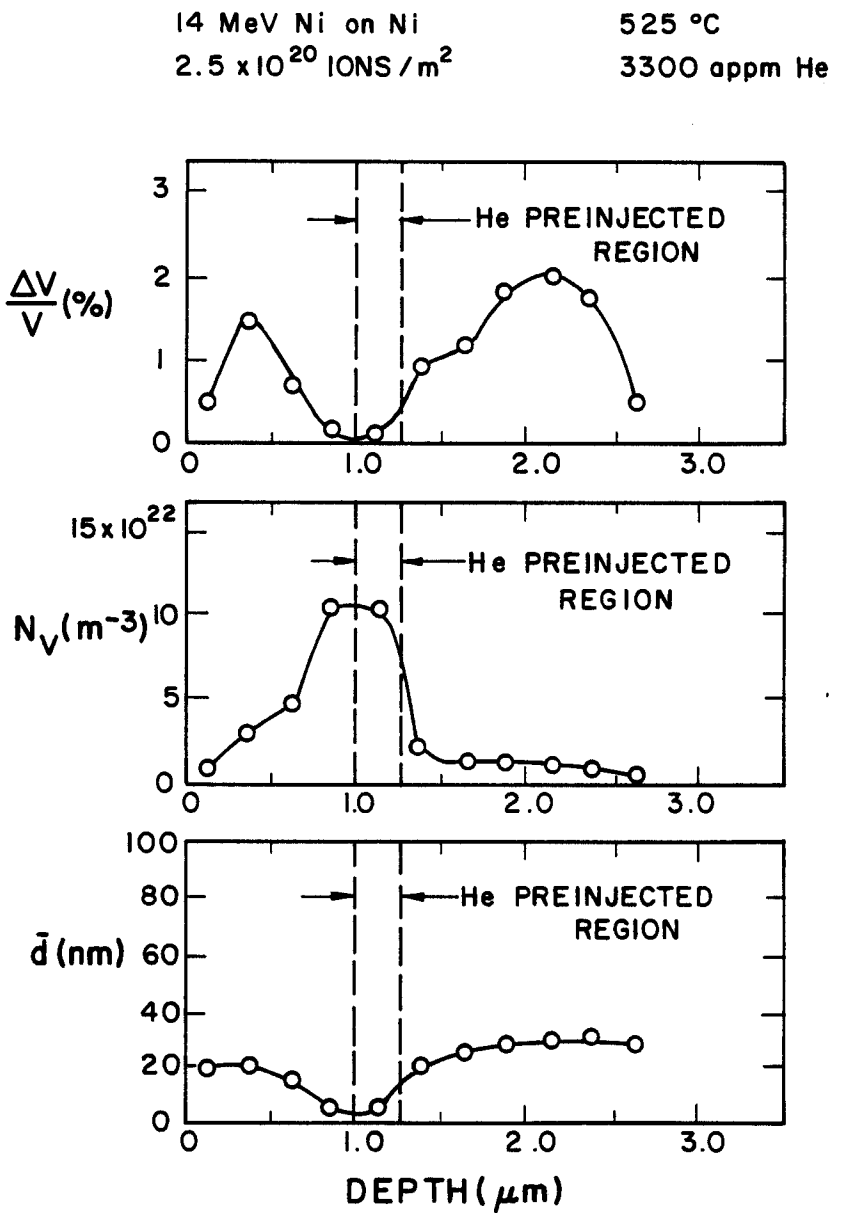

Fig. V-44. Swelling, void number density and mean void diameter vs. depth in helium preinjected (3250 appm) Ni irradiated at 525°C to a fluence of 2.5 x 10^{20} ions/m^2.

TABLE V-3. SUMMARY OF DAMAGE DATA

Sample	Dose at 1 μm (dpa)	Swelling at 1 μm (%)	Peak Swelling (%)	Line Dislocation Density Range (cm/cm^3) $x10^{10}$	Loop Density (cm^{-3}) $x10^{16}$
No Preinjection					
T-20-22-03	1	0.9	0	0.5-1.0	2
T-20-00-05	1	0.05	0	0.7-1.5	3
T-20-00-14	13	3.0	3.5	2.0-3.0	---
T-20-00-25	7	0.3	0.5	0.1-0.5	---
T-20-00-26	13	0	0	5-10	5
H Preinjection					
T-20-100H-18	13	2.0	1.6	0.1-0.4	---
T-20-1000H-27	7	1.8	2.0	0.5-1.0	---
T-20-500H-28	7	1.0	2.0	0.3-1.0	---
T-20-100H-29	7	0.5	1.3	0.1-0.3	---
T-20-1000H-30	7	2.0	2.5	0.2-0.7	---
T-20-500H-31	7	1.0	2.0	0.1-0.5	---
T-20-100H-32	7	0.5	0.7	0.1-0.5	---
T-20-100H-33	4	1.3	3.0	0.5-1.0	---
T-20-100H-34	27	2.0	3.0	0.3-0.8	---
He Preinjection					
T-20-100-09	3	0	2.8	0.5-1.0	---
T-20-600-10	3	0	1.4	0.7-2.0	---
T-20-100-11	3	0	1.2	1.0-3.0	---
T-20-100-12	7	1.0	3.0	0.5-1.0	---
T-20-650-20	13	1.3	2.0	0.1-0.5	---
T-20-65-21	7	0.8	2.0	0.3-1.0	---
T-20-650-22	27	0.7	4.0	0.1-0.3	---
T-20-3250-23	7	0.1	2.0	0.5-1.0	---

References for Chapter V

1. J.B. Whitley, Ph.D. Thesis, University of Wisconsin, Madison, Wisconsin, 1978.

2. R.L. Sindelar, private communication.

CHAPTER VI

DISCUSSION

A. Hydrogen Retention

The extremely low solubility of hydrogen[1] in nickel and its high diffusivity[2] may cause one to wonder if indeed any of the hydrogen which was preinjected into the nickel samples remained at the onset of the self-ion irradiation. During the course of sample preparation, the author had many occasions to observe the mobility of hydrogen which was preinjected into the foils. Figure VI-1 highlights the effect of this hydrogen migration which was observed. Figure VI-1 shows intergranular fracture of a plated foil which occurred as the 3 mm disc was punched from a plated slice. Note the smooth fracture surface indicative of the brittle fracture surface expected as a result of hydrogen embrittlement. This sample was preinjected with hydrogen to a fluence of 3×10^{18} H_3^+/m^2 (100 appm) and irradiated with nickel ions to a fluence of 1×10^{21} ions/m^2 (27 dpa at 1 μm). Another slice of this sample was successfully thinned for TEM analysis, the results of which were shown in Figs. V-19 and V-20. Similar hydrogen embrittlement problems were experienced on slices of plated foils from nearly all hydrogen preinjected foils which range in preinjection fluence from 3×10^{18} H_3^+/m^2 (100 appm) to 3×10^{19} H_3^+/m^2 (1000 appm).

Since the preinjected hydrogen appeared so very mobile, the question arises as to how much hydrogen is actually present in the

INTERGRANULAR FRACTURE DUE TO HYDROGEN EMBRITTLEMENT IN PREINJECTED SELF-ION IRRADIATED NICKEL

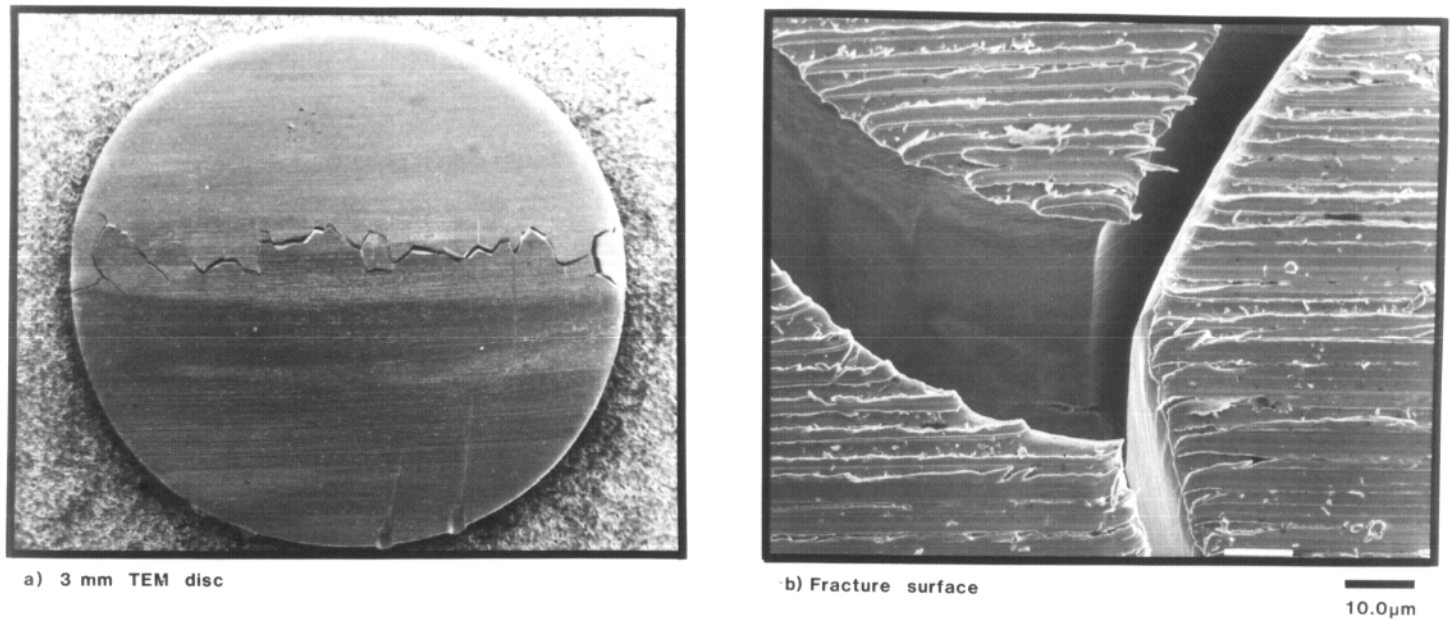

a) 3 mm TEM disc

b) Fracture surface

10.0μm

Fig. VI-1. SEM micrographs of intergranular fracture due to hydrogen embrittlement. Sample was preinjected with 3×10^{18} H_3/m_2 (100 appm) at 25°C and irradiated with Ni ions at 525°C to a fluence of 1×10^{21} ions/m^2. Fracture occurred when 3 mm TEM disc was punched from plated slice.

damage region at the beginning of the heavy-ion irradiation. A number of recent theoretical and experimental efforts have been published which address the trapping of hydrogen in metals.[3-13] These have been compared to the methods employed in this experiment to estimate the retained hydrogen after implantation.

Wilson and Pontau[8] and Tanabe et al.[11,12] have completed experiments, the results of which are most readily applicable to this experiment. Wilson injected samples of 304 stainless steel, Inconel 625, TZM and Ti-6Al-4V with a fluence of 1×10^{22} D/m^2 with a beam energy of 10 keV D_3^+ (3.3 keV/D atom) at temperatures ranging from 25°C to 275°C. A post-injection anneal was conducted and the amount of D released was determined using a quadrupole gas mass spectrometer. A representative sample of each injection was also analyzed utilizing the $^2D(^3He,\alpha)^1H$ reaction to determine near surface deuterium content. The high nickel alloy Inconel 625 provided the results which are of greatest interest to this study. Wilson found a trapping coefficient of approximately 0.01 for Inconel 625 implanted at 25°C. This means that 1% of the implanted deuterium was trapped in the near surface region.

Tanabe et al.[11,12] completed similar studies on pure nickel at temperatures in the range of 300-500°C with deuterium ions at energies between 20 keV and 30 keV. The 300°C implantation of pure Ni by Tanabe produced results very similar to the 275°C implantation of Inconel 625 by Wilson suggesting similar trapping coefficients exist for the two materials.

Another experiment by Wilson et al.[9] measured deuterium trapping characteristics in 304 stainless steel which was predamaged with 8 keV He^+ to a fluence of 10^{21} He^+/m^2. It was determined that this predamage increased the deuterium trapping by a factor of 3. This indicates an increase in deuterium retention with increased predamage. However, at very high predamage levels (10^{23} He^+/m^2) deuterium retention dropped. This reduction in retention was thought to be due to the formation of a dislocation network which extended from the damaged region to the surface allowing deuterium to escape.

The aforementioned experiments can be compared to this current work to provide an estimate of the actual hydrogen retained in the preinjected samples. Preinjections in this experiment were completed at accelerating potentials which were varied in 100 kV increments beginning at 700 kV and ending at 200 kV. This produced incident H^+ ions with energies ranging from 233 keV to 67 keV. These hydrogen ions produce damage over the implantation range (0.3-1.0 μm). Since a majority of the displacement damage is produced at the end of range of the irradiating ion, as described in detail in Chapter II, hydrogen trapping sites are expected to be formed over the same implanted range (0.3-1.0 μm).

Comparison of the Tanabe experiments to the Wilson work suggest a similar deuterium trapping coefficient for nickel and Inconel 625. Hence, for this work, it is assumed for a 25°C implantation, 1% of the injected hydrogen is trapped. This is a conservative estimate since variation in the energy of the beam in this experiment produces

traps over a wide range of depth (0.3-1.0 μm) as compared to the mono-energetic, low energy implantations of Wilson. Hence, for this experiment which implanted H_3^+ to fluences of 3 x 10^{18} to 3 x 10^{19} H_3^+/m^2 representing concentrations of 100-1000 appm if all the hydrogen was retained, the actual concentrations are assumed to be 1% of the injected concentrations or 1 appm, 5 appm and 10 appm. Referring to Chapter I of this study, it was found that for a Gas Driven Permeation model, first wall and blanket hydrogen isotope concentrations of 1-10 appm are expected in 316 stainless steel. When considering Plasma Driven Permeation, concentrations of hydrogen isotopes in the range 2-20 appm are expected. Therefore, the author feels that the preinjected hydrogen fluences used in this experiment, which represent retained hydrogen concentrations of at least 1-10 appm, are very relevant.

An effort was made in this work to investigate the microstructure of the as-injected material to determine the effects of preinjection. Figure VI-2 shows a nickel foil preinjected with hydrogen to a fluence of 3 x 10^{19} H_3^+/m^2 at 25°C. For this hydrogen preinjection case, there was a slight increase in dislocation density near the interface over bulk regions of the foil. This increase was from about 5 x 10^8 cm^{-2} to about 10^9 cm^{-2} which may be attributed to the stress produced by the plating. Hence, the damage produced by the hydrogen preinjection is not readily observable.

To investigate possible microstructural modification produced by the hydrogen as it becomes untrapped at the irradiation temperature,

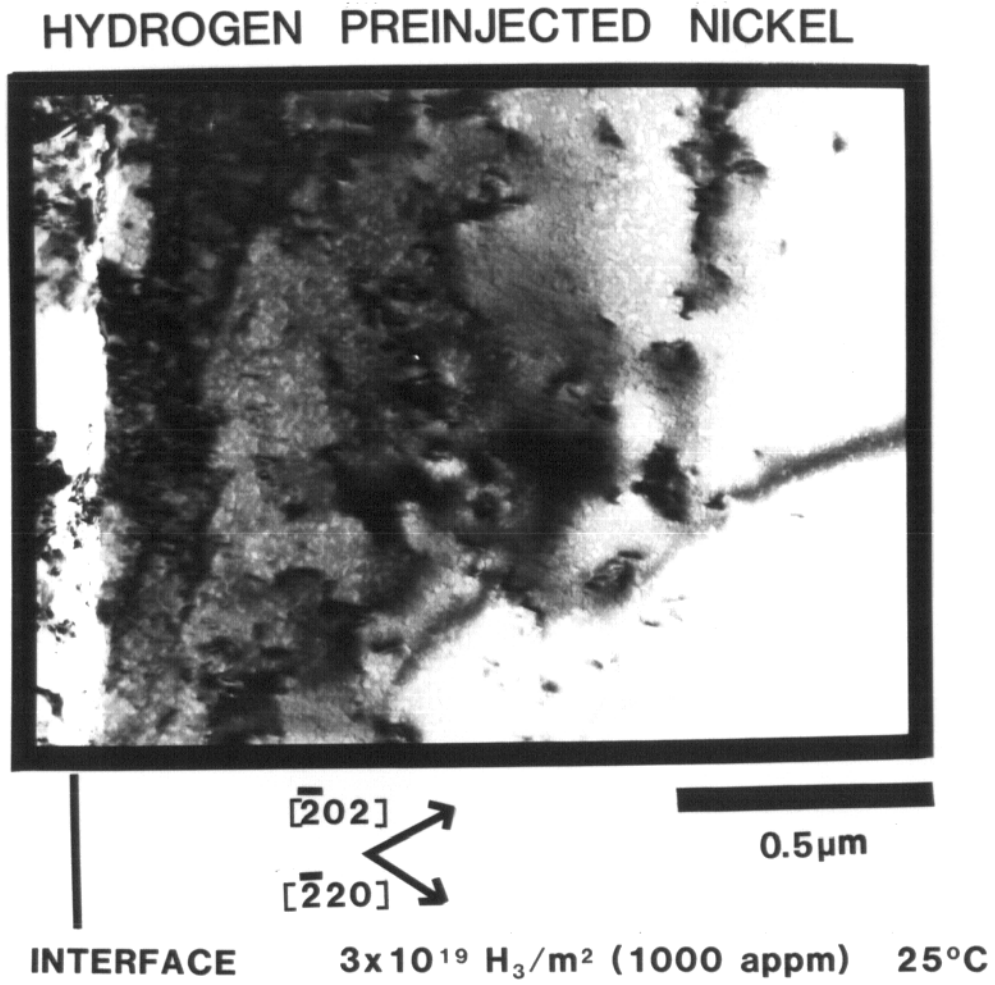

FIG. VI-2. DISLOCATIONS PRODUCED IN NICKEL DURING A PREINJECTION OF 3 x 10^{19} H_3^+/m^2 (1000 APPM) AT 25°C.

preinjected nickel foils were annealed at the irradiation temperature (525°C) for the approximate irradiation time (1 hour). Figure VI-3 shows a nickel sample which was preinjected with a hydrogen fluence of 3 x 10^{19} H_3^+/m^2 at 25°C and annealed at 525°C for 1 hour. No observable variation in microstructure was noted when compared to the sample injected at 25°C but not annealed. However, hydrogen embrittlement similar to that shown in Fig. VI-1 was experienced during post-irradiation sample preparation.

B. Hydrogen Effects on Void Formation

B.1. 525°C Irradiations

The effect of injected hydrogen concentration on microstructure was dramatic as can be seen in Fig. VI-4. This figure is a composite of micrographs showing the variation in void microstructure for a nickel sample which contains no gas and three samples with injected fluences of 3 x 10^{18} to 3 x 10^{19} H_3^+/m^2 (estimated retained concentrations of 1-10 appm). These samples were all subsequently irradiated at 525°C with nickel ions to a fluence of 2.5 x 10^{20} ions/m^2 (7 dpa at 1 μm).

The effect of the variation in hydrogen content on swelling in these samples is shown in Fig. VI-5. This figure shows the increase in swelling associated with increasing hydrogen concentration for two different damage levels (i.e., two different depths in the foil). Note that the dpa rate is constant for each damage level. The top curve shows the swelling variation at the peak damage region (27 dpa), while the bottom curve shows the swelling variation at a depth

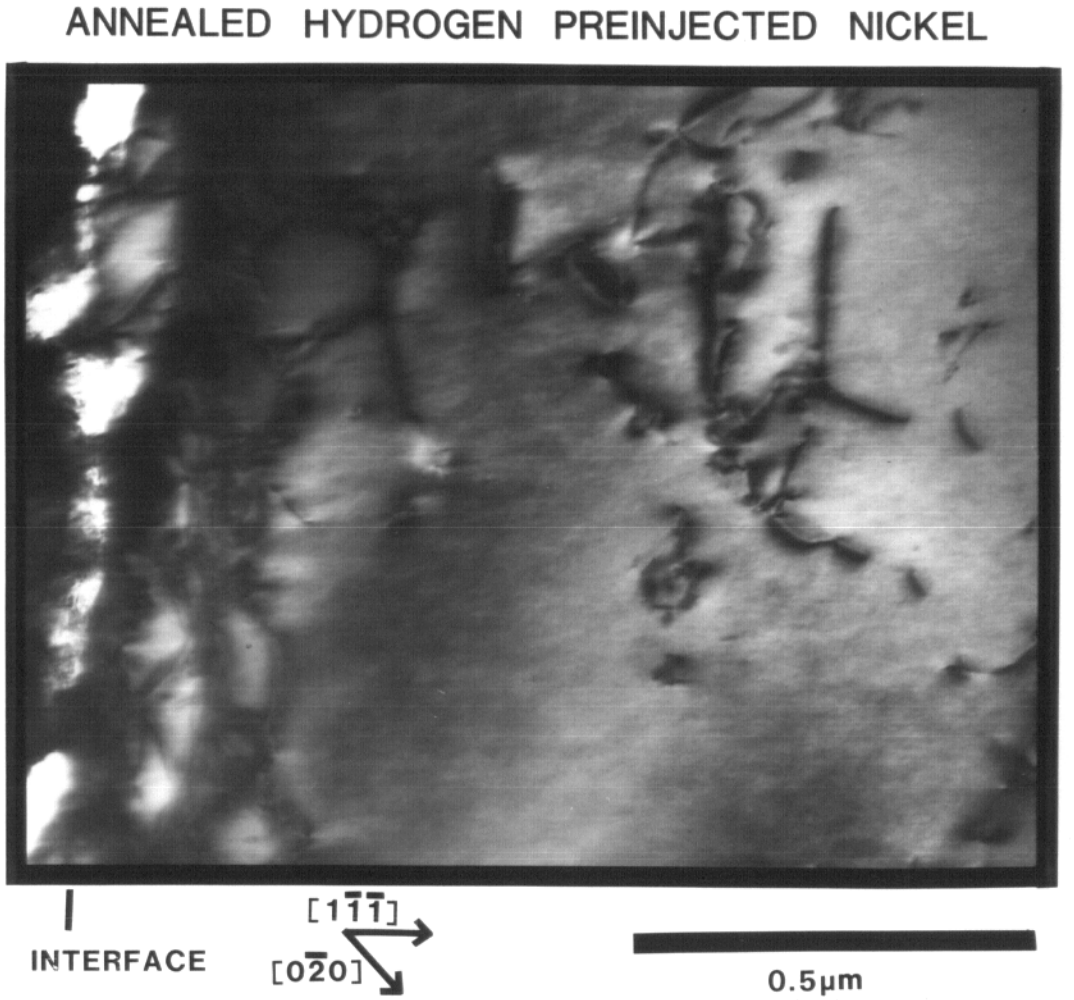

FIG. VI-3. DISLOCATION MICROSTRUCTURE IN NICKEL FOLLOWING A PREINJECTION OF 3 x 10^{19} H_3^+/M^2 (1000 APPM) AT 25°C AND A SUBSEQUENT ANNEAL AT 525°C FOR 1 HOUR.

VARIATION IN VOID MICROSTRUCTURE WITH INCREASING HYDROGEN PREINJECTION AT 525 C

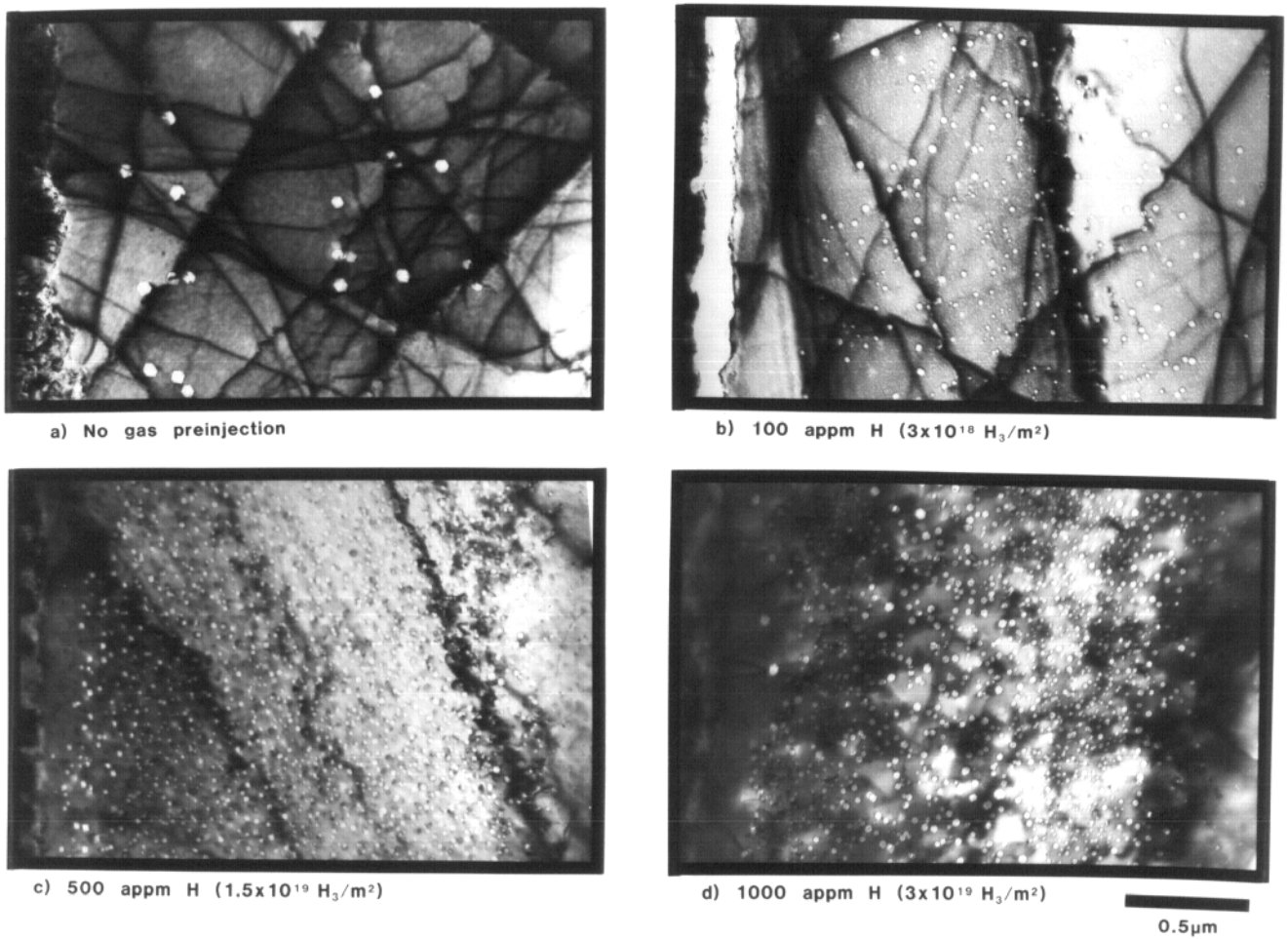

Fig. VI-4. Void microstructure at various hydrogen contents for Ni irradiated with Ni ions to a fluence of $2.5x10^{20}$ ions/m^2 at 525°C.

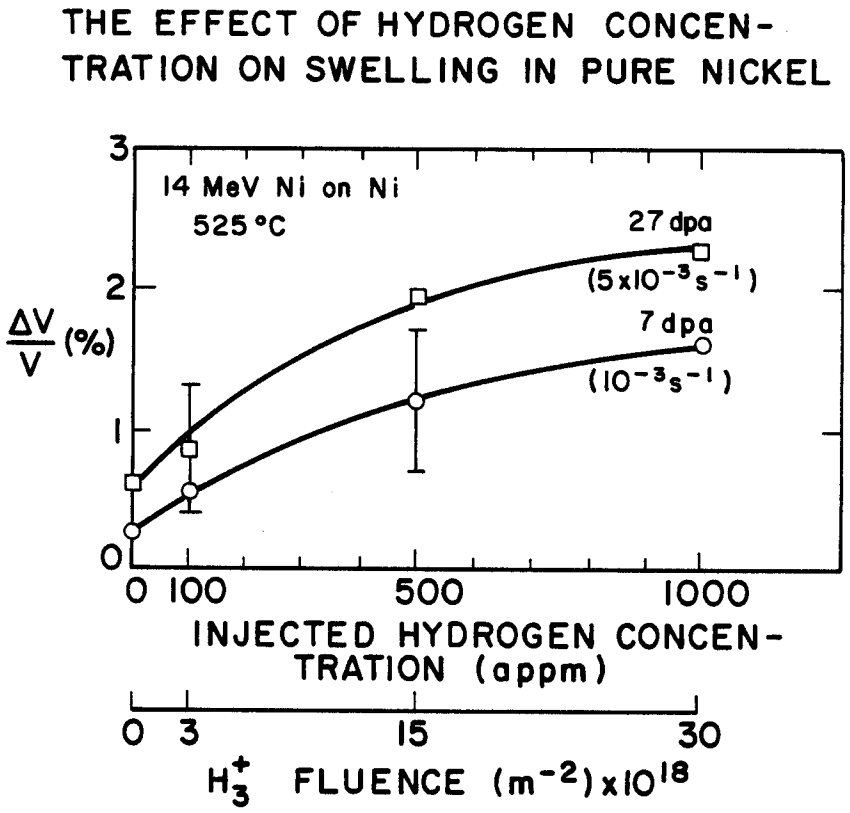

Fig. VI-5. Swelling vs. injected hydrogen concentration for nickel irradiated to a fluence of 2.5 x 10^{20} ions/m^2 at 525°C.

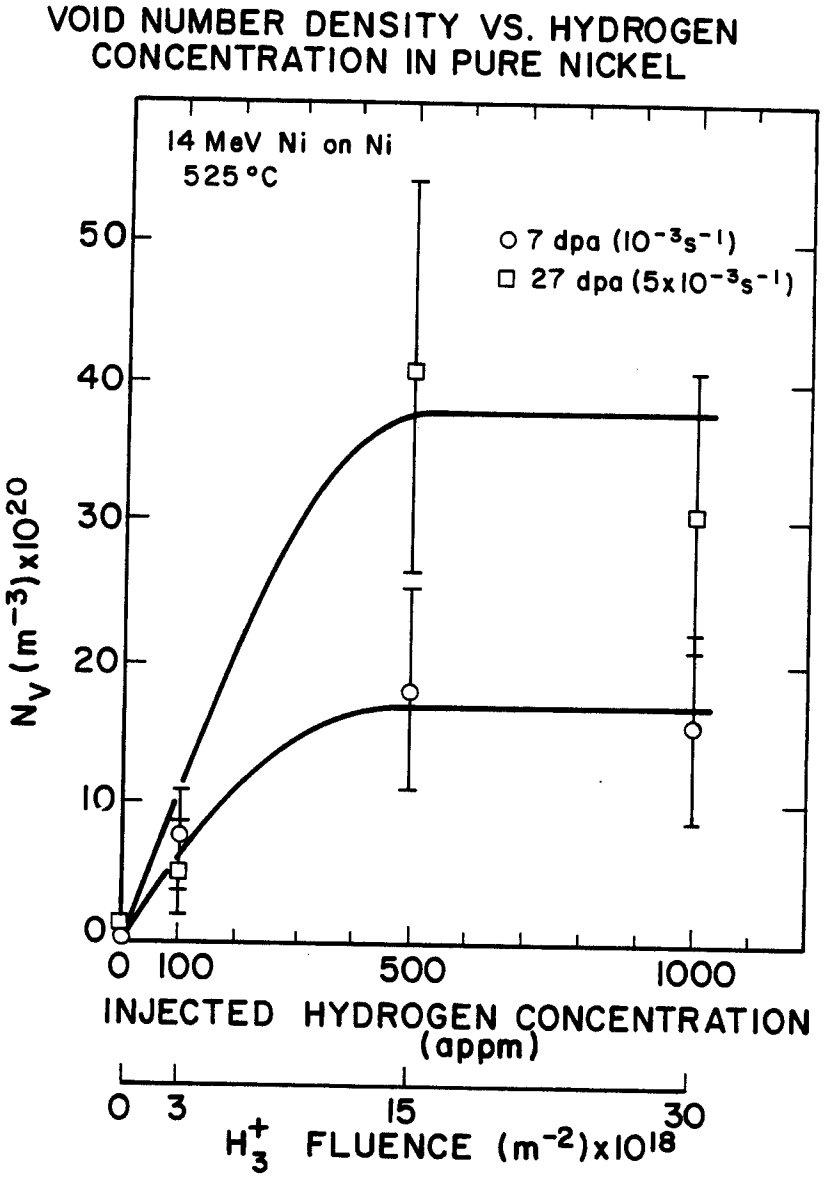

Fig. VI-6. Void number density vs. injected hydrogen concentration for nickel irradiated to a fluence of 2.5 x 10^{20} ions/m^2 at 525°C.

of 1 μm. Also note that as the hydrogen concentration is increasing, the rate of swelling increase is not linear but appears to be saturating. To provide conclusive evidence of this saturation a further increase in injected hydrogen content (perhaps 3000 appm) would be of value.

The variation in void number density as a function of injected hydrogen concentration is shown in Fig. VI-6. An increase in void number density is noted for increasing injected hydrogen concentrations from 0 to 500 appm (estimated 0-5 appm retained). A saturation in void number density appears when the injected hydrogen concentration reaches a level of 500 appm (5 appm retained). This is further evidence of the beginning of swelling saturation as proposed above.

The most dramatic effect of injected hydrogen concentration variation is shown by the marked decrease in mean void diameter (Fig. VI-7). With no hydrogen injection the mean void diameter is approximately 70 nm. The injection of even the smallest amount of hydrogen (100 appm injected, estimated 1 appm retained) reduces the mean void diameter to about 28 nm. This mean void diameter remains relatively constant with increasing hydrogen injection up to 1000 appm injected. It should also be noted that there is little variation in mean void diameter with increasing damage levels. Since the mean void diameter throughout the entire damage region (not just from 0 to 1 μm in depth) shows little variation, it might be suggested that there

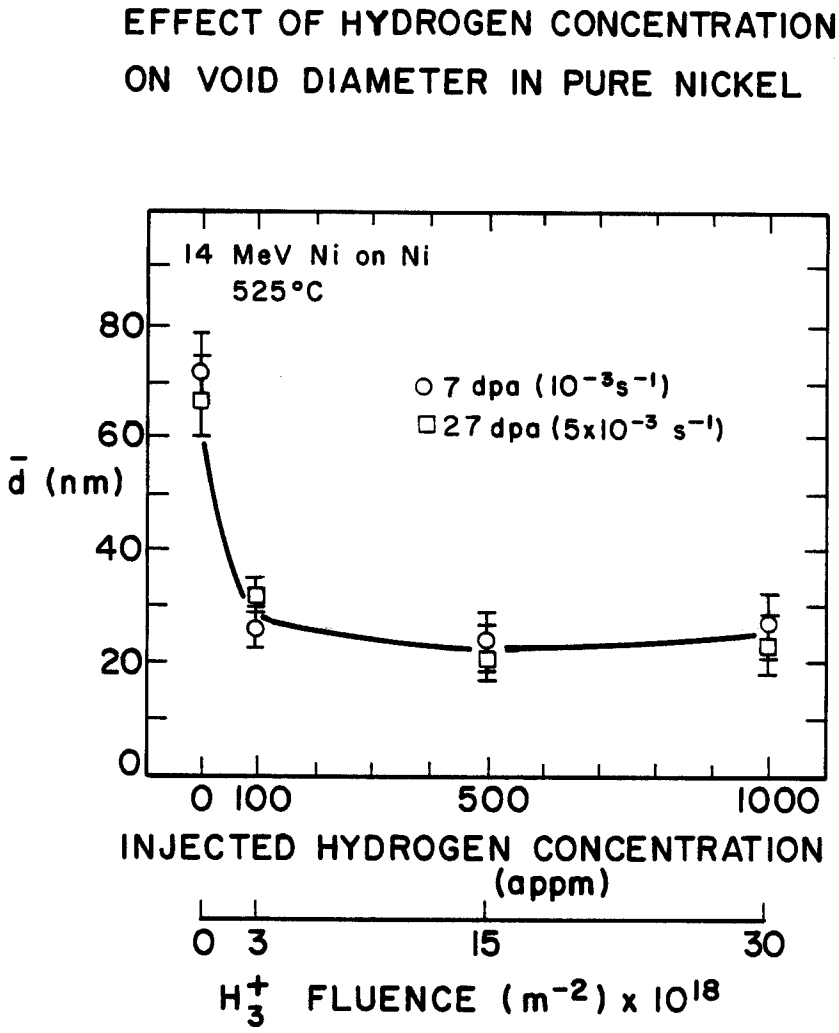

Fig. VI-7. Mean void diameter vs. injected hydrogen concentration for nickel irradiated to a fluence of 2.5×10^{20} ions/m^2 at 525°C.

exists some trapping of hydrogen throughout the sample and not just in the damage region produced by the preinjection.

A comparison of swelling versus displacement damage is presented in Fig. VI-8 for various injected hydrogen concentrations. The increase in swelling with increasing preinjected hydrogen concentration is again evident. Also, the saturation in swelling with increasing damage for each hydrogen concentration is shown. The increase in damage rate with increasing damage level must also be considered. This rate variation may contribute to the observed saturation in swelling. This saturation has been noted in other heavy-ion irradiations as indicated in Chapter III of this report. Whitley[14] reported a similar saturation characteristic in nickel. Comparisons to Whitley's work are made in a subsequent section of this chapter.

B.2. 625°C Irradiations

Irradiations at conditions similar to those presented in the previous section were completed at an irradiation temperature of 625°C. The void microstructure produced in these irradiations can be seen in Figs. V-21, V-23 and V-25. The effect of injected hydrogen concentration is very noticeable in these figures with the most dramatic effect occurring between injected hydrogen concentrations of 500 and 1000 appm (estimated 5-10 appm retained).

The effect of various hydrogen concentrations on swelling at 625°C is shown in Fig. VI-9. There is a continual increase in swelling with increasing injected hydrogen concentration for the low damage level (7 dpa) while at the higher damage level (27 dpa) there

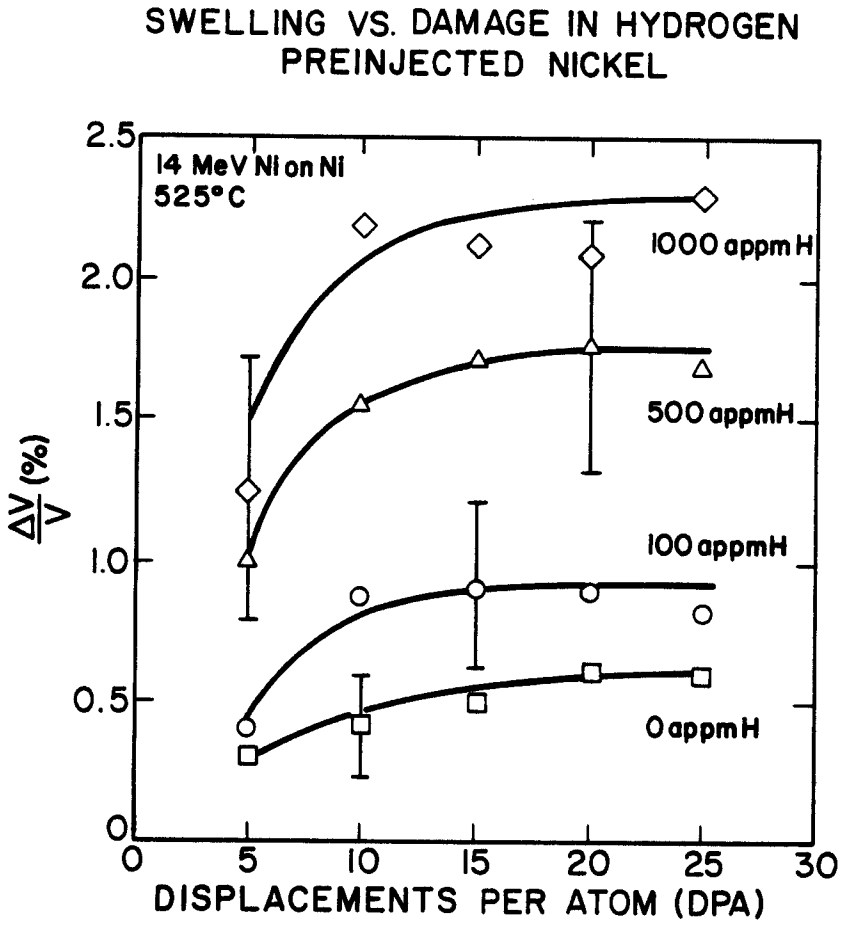

Fig. VI-8. Swelling vs. damage for various injected hydrogen concentrations in nickel irradiated to a fluence of 2.5 x 10^{20} ions/m^2 at 525°C. Note that the damage rate also increases with increasing total damage level.

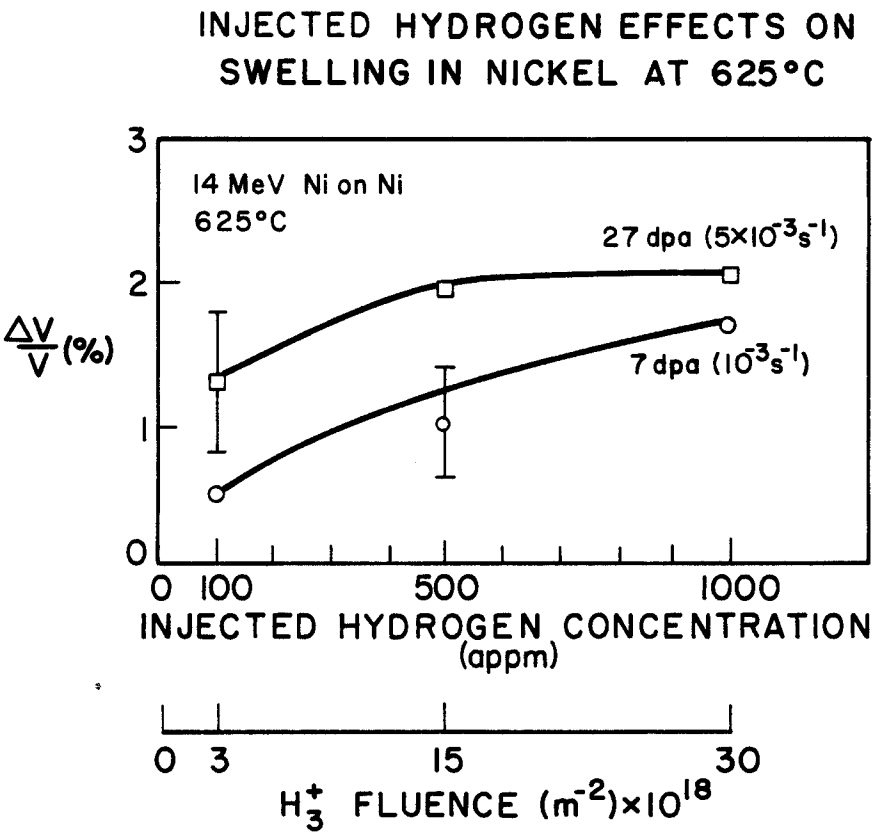

Fig. VI-9. Swelling vs. injected hydrogen concentration for nickel irradiated to a fluence of 2.5 x 10^{20} ions/m^2 at 625°C.

appears to be a saturation in swelling. This saturation is associated with a dramatic variation in microstructure morphology as discussed below.

The variation in void number density with increasing injected hydrogen concentration is shown in Fig. VI-10. There is a dramatic increase in void number density as the injected hydrogen concentration increases from 500 to 1000 appm. This increase is not unlike the increase noted between 0 and 500 appm injected hydrogen in the 525°C irradiations as shown in Fig. VI-6 and suggests that the first hydrogen effect on void formation at 625°C does not occur until an injected fluence of 3×10^{19} H_3^+/m^2 (1000 appm) is reached. One explanation for this observation is the possibility that the approximately 2 minutes required to heat the sample to the 625°C prior to the beginning of the irradiation may have been sufficient time for all of the trapped hydrogen to escape the foil in the 100 and 500 appm samples. If this is the case the actual hydrogen content of the 1000 appm sample may have also been substantially less.

Further indications of the possibility of hydrogen escape during the heating prior to irradiation at 625°C is given by the mean void diameter data presented in Fig. VI-11. The large diameters (90 nm) given for the 100 and 500 appm injected hydrogen concentrations are similar to the large voids formed with no gas present as shown in Fig. V-9. At 1000 appm injected hydrogen the mean void diameter drops to a level similar to that of the 525°C irradiations (35 nm).

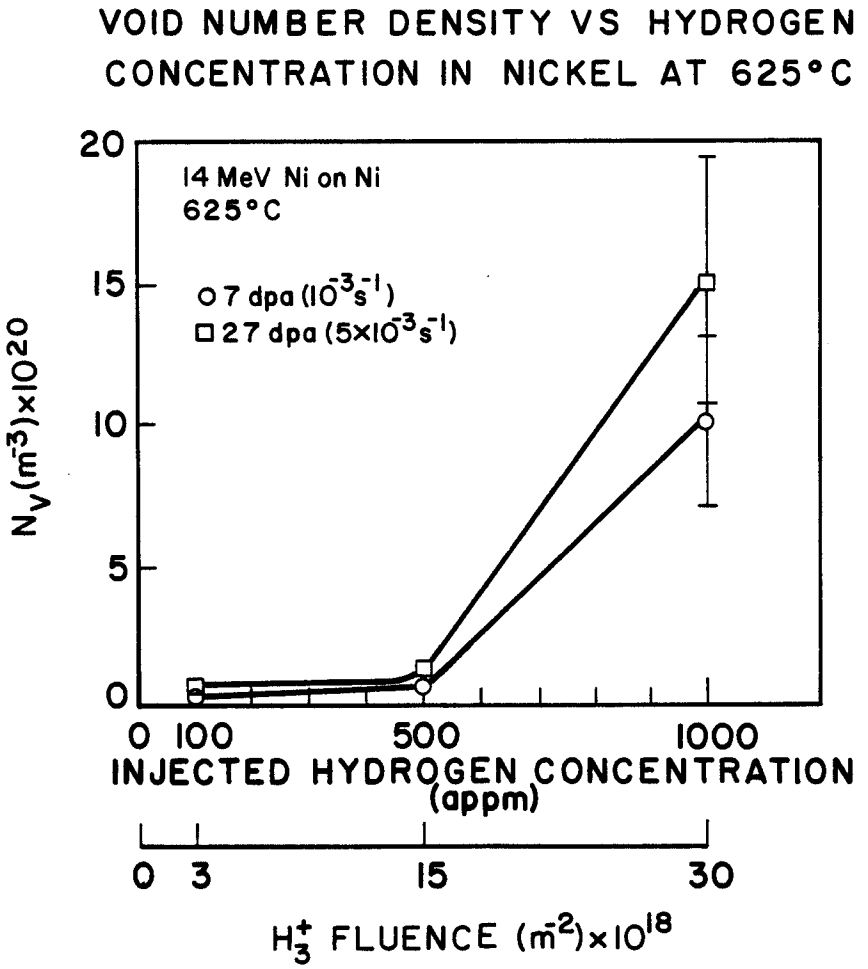

Fig. VI-10. Void number density vs. injected hydrogen concentration for nickel irradiated to a fluence of 2.5 x 10^{20} ions/m^2 at 625°C.

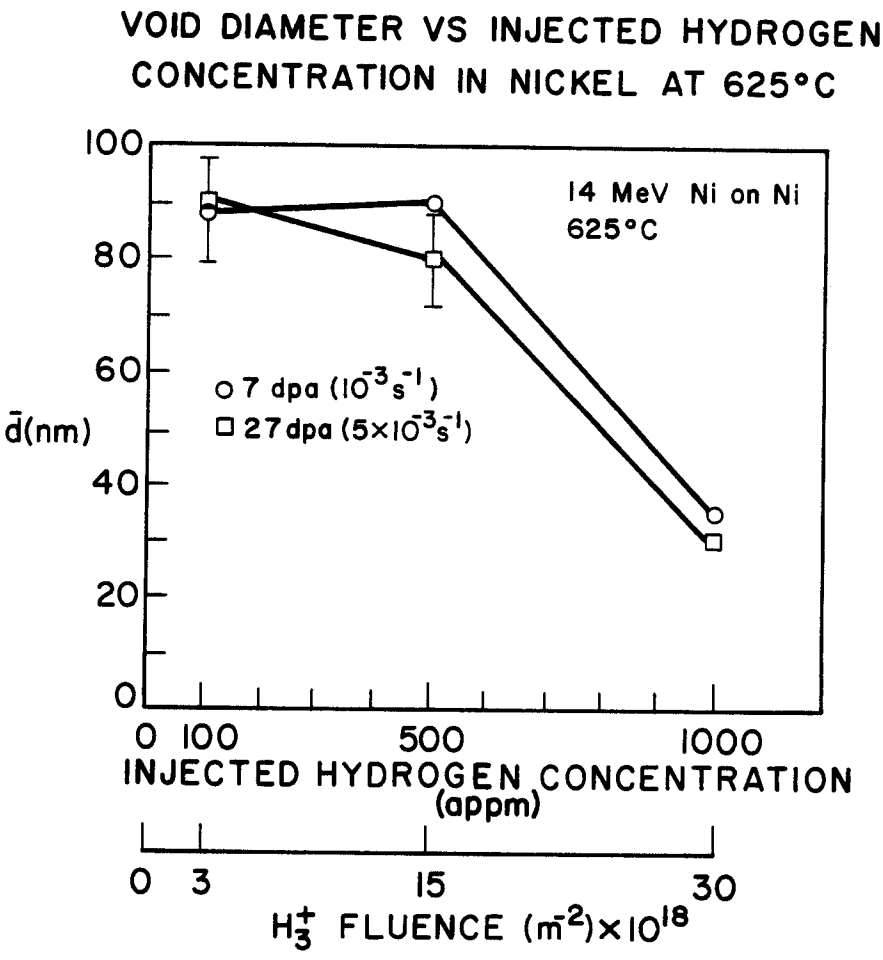

Fig. VI-11. Mean void diameter vs. injected hydrogen concentration for nickel irradiated to a fluence of 2.5 x 10^{20} ions/m^2 at 625°C.

This is also indicative of the effect of initial hydrogen content on void formation.

A comparison between the swelling and the damage at 625°C for various injected hydrogen concentrations is shown in Fig. VI-12. An increase in swelling with increasing injected hydrogen concentration represents the same trend as found in the 525°C irradiations. A saturation in swelling for each hydrogen concentration is also suggested. The data from this study suggests that gas content may play an important role in swelling exhibited in heavy-ion irradiation experiments. This is discussed further in the following section.

C. Rate Effects

One of the continuing questions regarding the applicability of ion irradiation data is the effect of the relatively high displacement rate on microstructural evolution. Some discrepancies have been noted between neutron irradiation data and ion irradiation data for similar damage levels.[15,16] These discrepancies were initially attributed to an "internal temperature shift" which was proposed by Garner and Guthrie.[17] Further work by Whitley[14] suggested the possibility of a displacement rate effect. A recent review by Garner[18] addressed possible injected interstitial effects as a partial cause for the discrepancies between neutron and ion irradiation data.

The cross-section method of sample analysis used in this study proves very valuable when attempting to further understand variations in dose rate effects. Garner[18] proposed injected interstitial

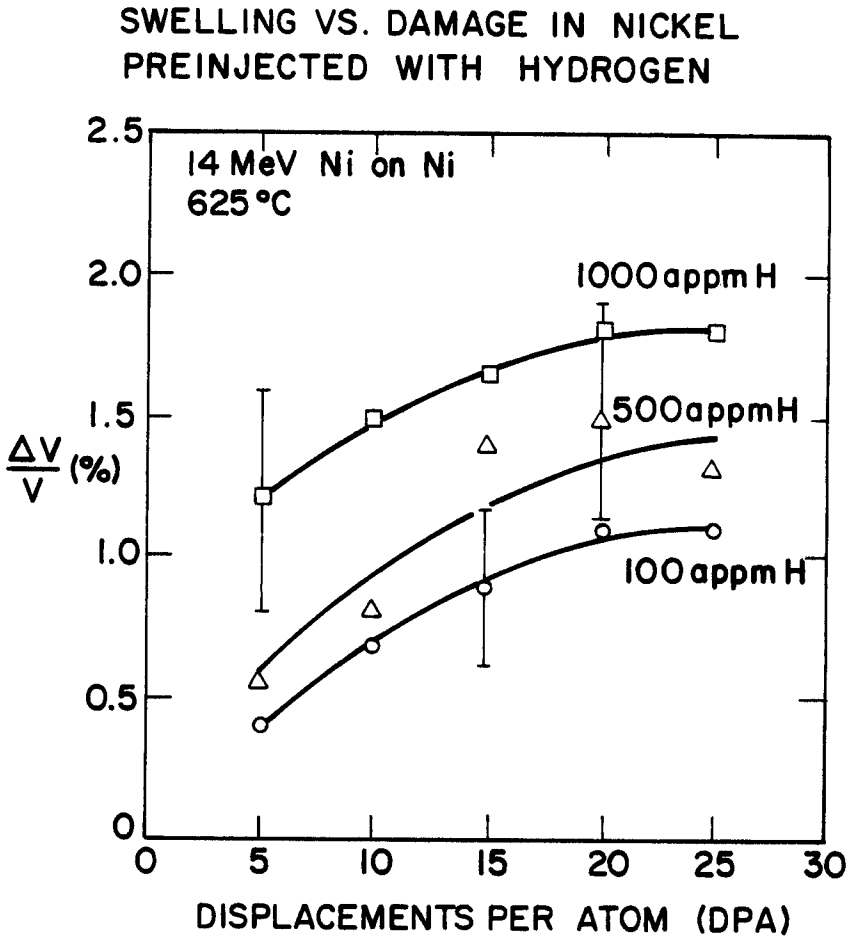

Fig. VI-12. Swelling vs. damage for various injected hydrogen concentrations in nickel irradiated to a fluence of 2.5 x 10^{20} ions/m^2 at 625°C. Note that the damage rate also increases with increasing total damage level.

effects as a possible explanation for the swelling suppression. Cross-section studies such as this one and that of Whitley[14] can provide a better understanding of dose rate effects by allowing the evaluation of swelling rate while eliminating the effects of injected interstitials and the effects of swelling saturation.

It should be noted at this time that the effect of injected hydrogen content on swelling rate which was derived from the data presented in Fig. VI-8 has some limitations. Since no data are available at damage levels below 5 dpa it is not possible to accurately determine the linear swelling regime. Hence, the data presented in the following figures (VI-13 and VI-14) can only suggest possible trends with respect to hydrogen effects on swelling rate.

The data presented in Fig. VI-13 represent the swelling rate versus the damage rate for nickel irradiated with 14 MeV nickel ions at 525°C. The data were taken from cross-sectioned samples in regions of the foil sufficiently far from the end-of-range of the injected interstitial to preclude any injected interstitial effects. Also, the level of swelling was in the linear portion of the swelling regime. The data from this study shown in Fig. VI-13 indicates a definite effect of injected hydrogen content. The swelling rate ranges from 0.06%/dpa with no injected hydrogen to 0.3%/dpa with an injected hydrogen concentration of 1000 appm (estimated 10 appm retained). A comparison to the work of Whitley with similar damage rates suggests that Whitley's samples probably contained concen-

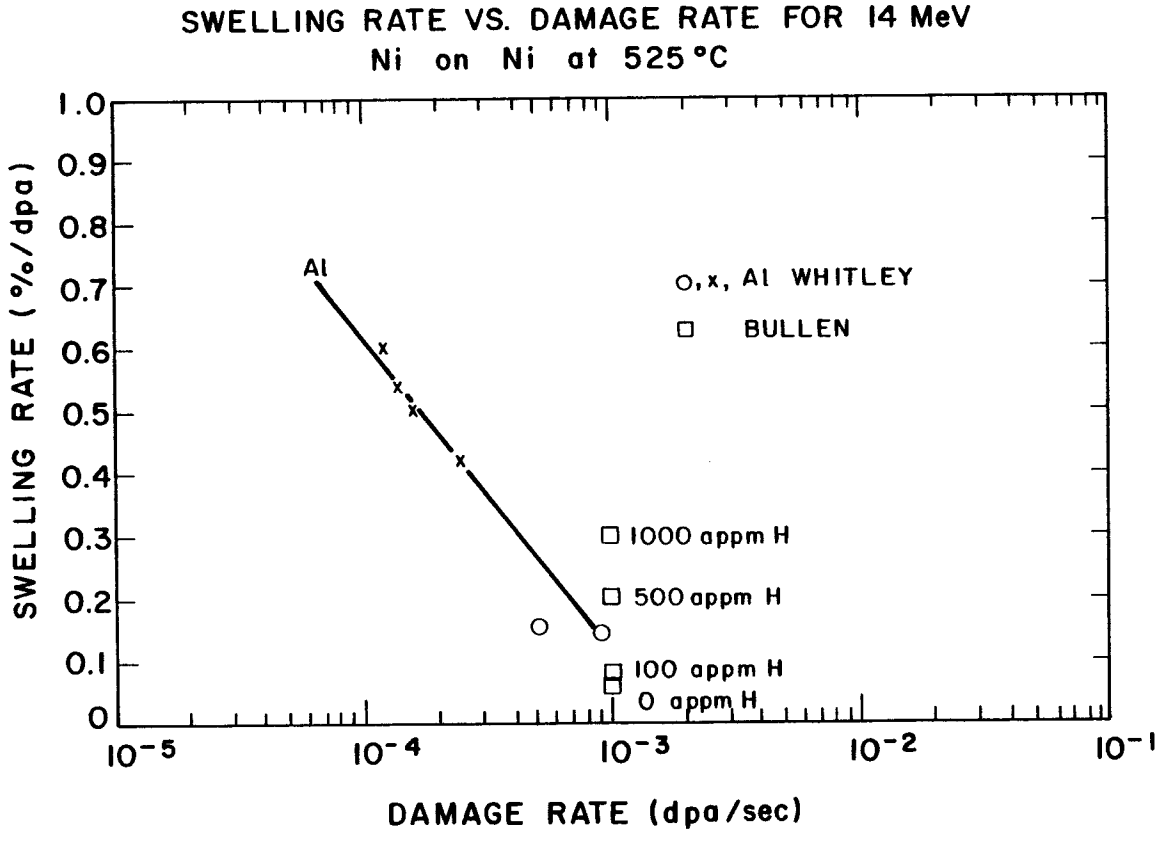

Fig. VI-13. Swelling rate vs. damage rate for self-ion irradiated nickel at 525°C. The data presented were obtained from cross-section foils well away from the injected interstitial peak and represents swelling in the linear regime (non-saturated).

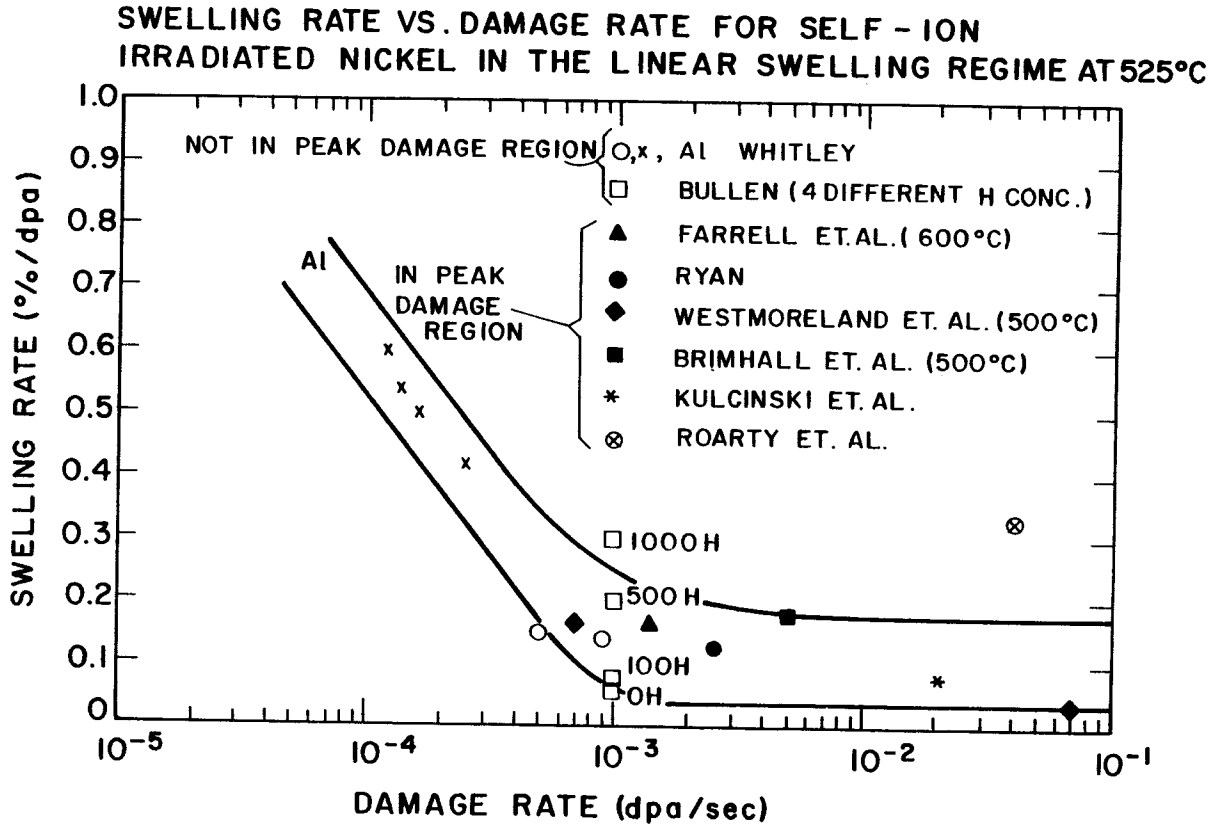

Fig. VI-14. Swelling rate vs. damage rate for self-ion irradiated nickel. The data presented represents swelling in the linear (non-saturated) regime.

trations of hydrogen between concentrations produced in this study by injections of 100 to 500 appm (estimated 1-5 appm retained).

The Whitley samples irradiated at lower dose rates show an increase in swelling rate, emphasizing the importance of damage rate on possible correlations to neutron data. The sample designated (A1) represents the swelling rate obtained by irradiation with 8.1 MeV aluminum ions at a dose rate of 6×10^{-5} dpa/sec. It should be noted that the variation in hydrogen content may be quite large in the Whitley samples due to the method of hydrogen introduction (preirradiation electropolish) and the lack of a complete temperature history of each sample.

Previous self-ion irradiation studies in nickel which utilized the backthinning technique of post-irradiation sample preparation can provide further insight into rate effects. The data from Farrell et al.,[19] Ryan,[20] Westmoreland,[21] Brimhall et al.,[22] Kulcinski et al.,[23] and Roarty et al.[24] (see Chapter III) has been plotted with that of Whitley and this study and is shown in Fig. VI-14. As discussed previously, the damage level in all of these samples is in the linear swelling regime below the saturation level. However, all data (except for that of Whitley and this study) includes injected self-interstitial effects. It should also be noted that these samples contain no helium. The data of Brimhall et al.[22] and Westmoreland et al.[21] are for irradiation temperatures of 500°C while the data from Farrell et al.[19] are at 600°C.

Evaluation of this data (Fig. VI-14) for non-saturated swelling shows two distinct trends. There is no clear evidence of any injected interstitial effects in self-ion irradiated nickel at 525°C at damage rates above 10^{-3} dpa/sec for the range of damage levels presented in these studies (1-40 dpa, see Chapter III). Below a damage rate of 10^{-3} dpa/sec, hydrogen concentration and damage rate are important variables with respect to swelling rate. The hydrogen effect observed in this study suggests another parameter which should be considered when attempting to correlate neutron and heavy-ion irradiation data.

D. Injected Interstitial Effects

The effect of injected interstitials on cavity nucleation in heavy-ion irradiations has been considered recently by Garner[18] as a possible factor in the correlation of neutron and heavy-ion data. The suppression of nucleation at low temperature (T < 400°C) was initially noted by Whitley.[14] An attempt to more accurately define the temperature range in which nucleation suppression due to injected interstitials occurs was undertaken in this study as shown in Figs. V-1 through V-6. Figure V-1 shows suppression of nucleation at the end of range of the injected self-interstitial at 450°C. Increased suppresion is noted in Fig. V-3 at 425°C. Almost complete suppression is noted at 400°C in Fig. V-5.

A more complete understanding of the microstructural evolution during the course of these low temperature (400-450°C) irradiations is obtained by applying the void nucleation program developed by

Plumton.[25] This program considers the effect of injected interstitials on void nucleation as a function of temperature and material properties. Figure VI-15 shows the calculated nucleation rate as a function of depth for 14 MeV nickel ions incident on nickel. The top curve is the nucleation rate for an irradiation temperature of 400°C. The middle curve represents the nucleation rate for 450°C, while the lower curve gives the nucleation rate for 525°C. Note the increase in suppression of nucleation with decreasing temperature over the range of the injected self-interstitial (1.75-2.25 μm). Comparison of these curves to the data presented in Figs. V-1 to V-6 shows a qualitative agreement with the model for suppression at the end-of-range of the irradiating ion. As the temperature decreases the suppressed region increases in size in accordance with the model calculations.

E. Helium Effects

The role of helium as a nucleating agent has long been recognized as a major contributing factor in the swelling behavior of irradiated metals.[19,26-28] The results presented in this report represent one of the few studies which employs the cross-section technique to study the effects of preinjected helium on void formation in self-ion irradiated nickel. The only other cross-section study on helium injected self-ion irradiated nickel was completed by Farrell et al.,[19] the results of which will be compared to this study in Section VI-F of this report.

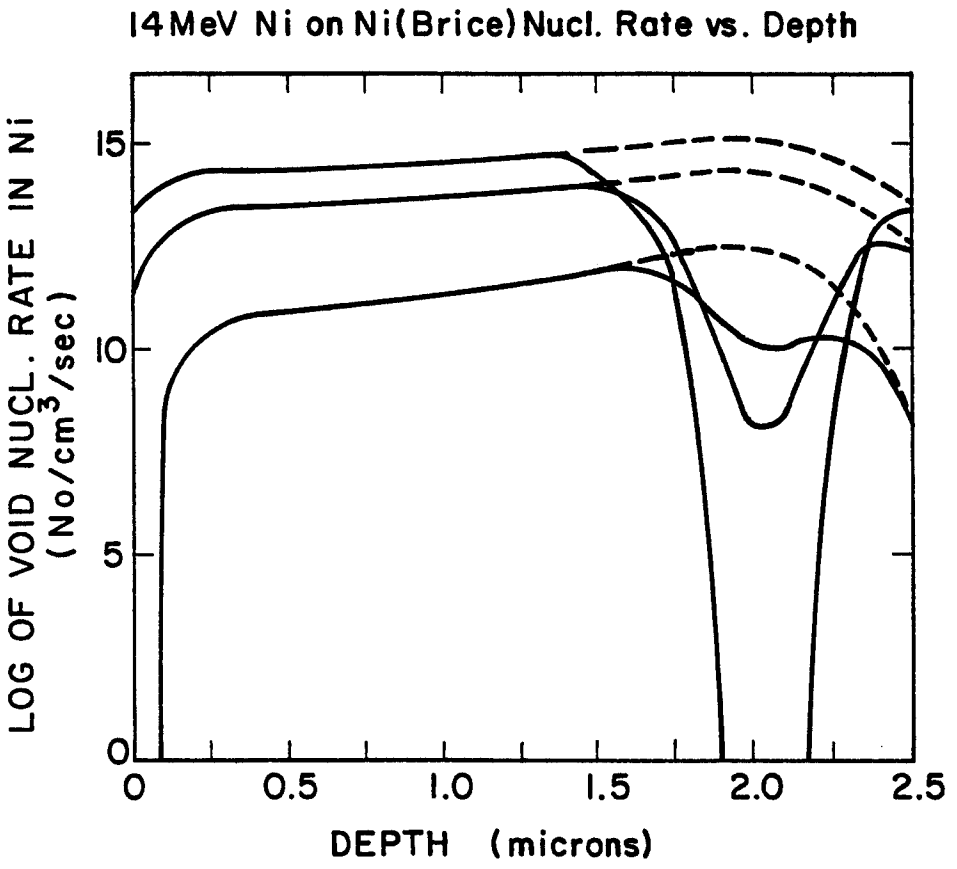

Fig. VI-15. Nucleation rate vs. depth for 14 MeV nickel self-ion irradiation. Irradiation temperature variations of 400, 450 and 525°C are represented by the top, middle and bottom curves respectively. Dashed lines indicate nucleation rate without considering injected interstitials. Solid lines show nucleation suppression with decreasing temperature at the end-of-range of the injected self-interstitial (1.75 μm - 2.25 μm). (From Plumton[25]).

In this study helium was preinjected at 25°C using two methods. The first method involved variation of the incident helium ion energy from 700 keV down to 200 keV to produce a relatively uniform helium concentration over a region extending from a depth of 1.25 μm to the surface. The second method used a 700 keV He^+ beam to preinject helium at a depth of 1.0-1.25 μm.

E.1. Uniform Helium Implantation

The results presented in the previous chapter for self-ion irradiated nickel which had been uniformly preinjected with He at concentrations of 100 and 600 appm showed some suppression in void formation in all cases. An attempt was made to more completely understand the effects of such preinjections by studying the microstructure of a nickel sample following uniform helium implantation. Figure VI-16 shows the loop microstructure produced by the injection of He to a uniform concentration of 1000 appm at 25°C. The mean loop diameter was 7.5 nm with a loop number density of 2×10^{20} m^{-3}. The microstructure suggests the existence of numerous trapping sites for He interstitials at the beginning of the self-ion irradiation which supports the results shown in Figs. V-29 through V-36.

The effect of the elevated temperature experienced during the irradiation on the microstructure of the helium preinjected nickel sample was investigated in the following manner. A nickel sample was preinjected at 25°C with a uniform concentration of 1000 appm He and then annealed at 525°C for 1 hour. The annealing time was chosen to correspond to the irradiation time for a fluence of 2.5×10^{20}

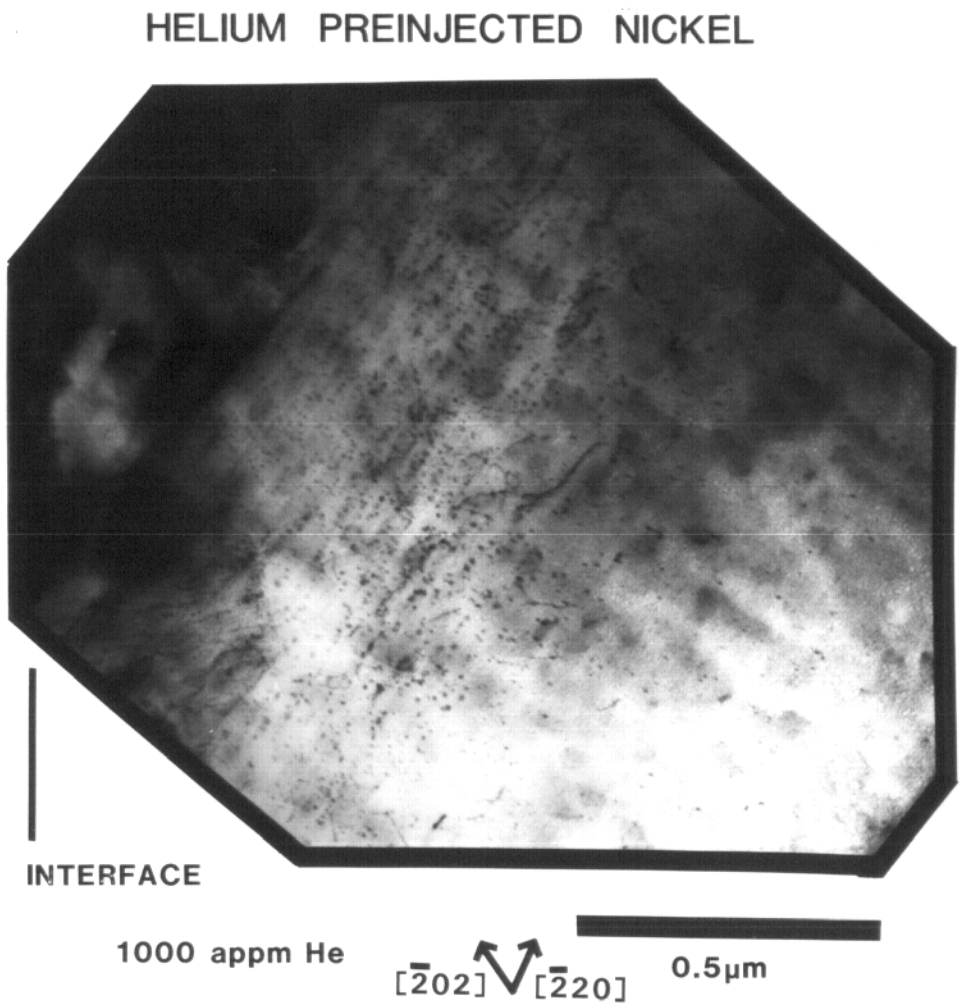

FIG. VI-16. LOOP MICROSTRUCTURE PRODUCED IN NICKEL DURING HE PREINJECTION TO A UNIFORM CONCENTRATION OF 1000 APPM HE AT 25°C.

ions/m^2. Figure VI-17 shows the loop microstructure obtained in nickel following preinjection and annealing as stated above. The mean loop diameter remained relatively constant at 7.0 nm (within experimental error) while the loop number density also remained constant at 2×10^{20} m^{-3}. This relatively constant loop diameter with no noticeable reduction in loop number density is expected for the stated conditions and further emphasizes the stabilizing effect He has on loops. This characteristic of loop stability with He present has been noted by Van Swygenhoven et al.[29,30] and Jager et al.[31] who have completed studies on the precipitation of helium into small bubbles and loop-punching by helium precipitation below the vacancy migration energy in He^+ injected nickel.

The previous samples were preinjected with 1000 appm He and experienced different thermal histories with no noticeable helium bubble formation. An attempt to produce helium bubbles was made with the results shown in Fig. VI-18. This figure shows the formation of helium bubbles in nickel which was preinjected at 25°C with 10000 appm He uniformly distributed from a depth of 1.25 μm to the surface of the sample. The injected sample was then annealed at 525°C for 1 hour to allow for bubble growth. The bubbles which formed had a mean diameter of 3.0 nm and a number density of approximately 10^{23} m^{-3}. These helium bubbles which formed are the precursors of blister formation. Similar bubble formation was noted prior to blistering by Fenske et al.[32] for He irradiated at 525°C.

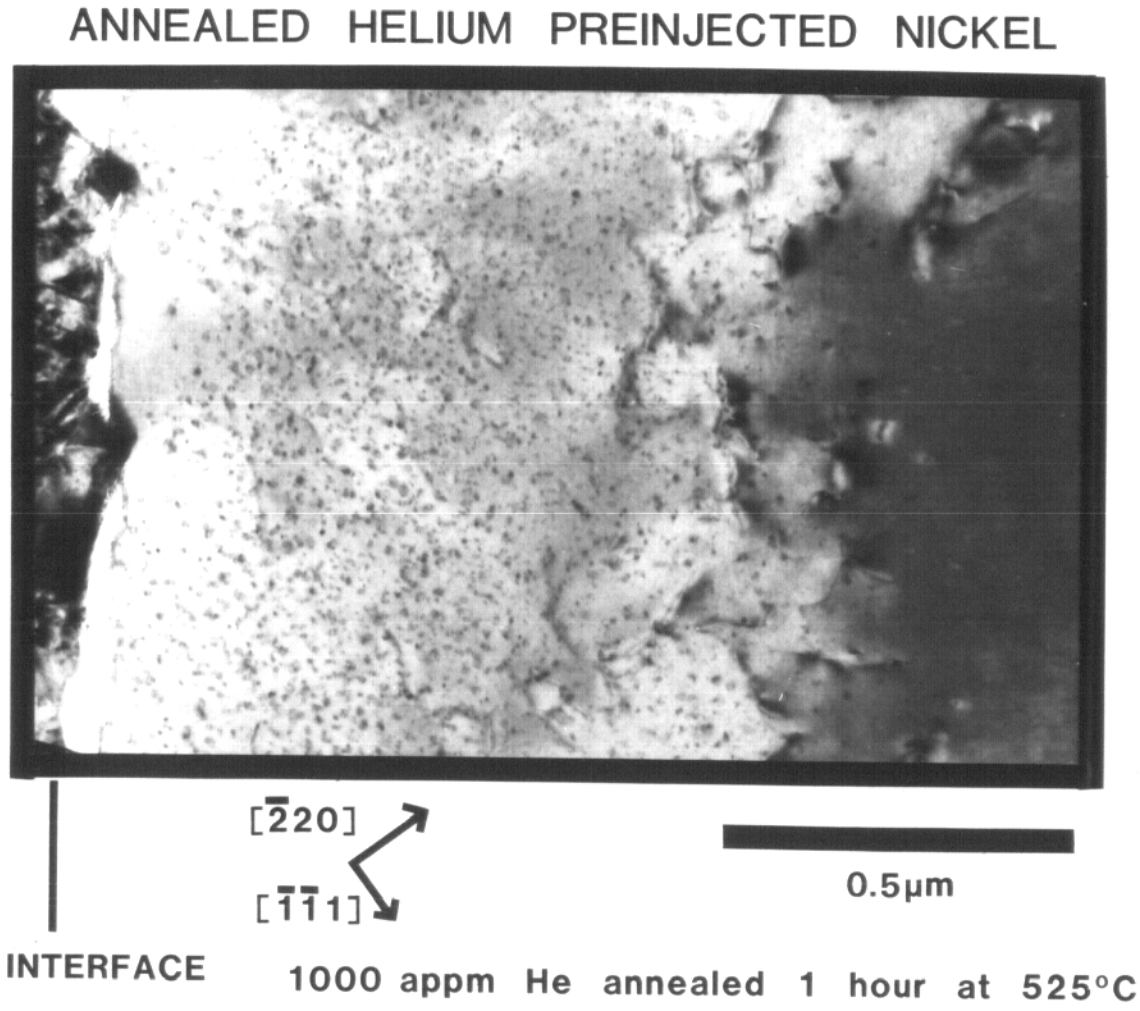

FIG. VI-17. LOOP MICROSTRUCTURE IN NICKEL PREINJECTED AT 25°C TO A UNIFORM CONCENTRATION

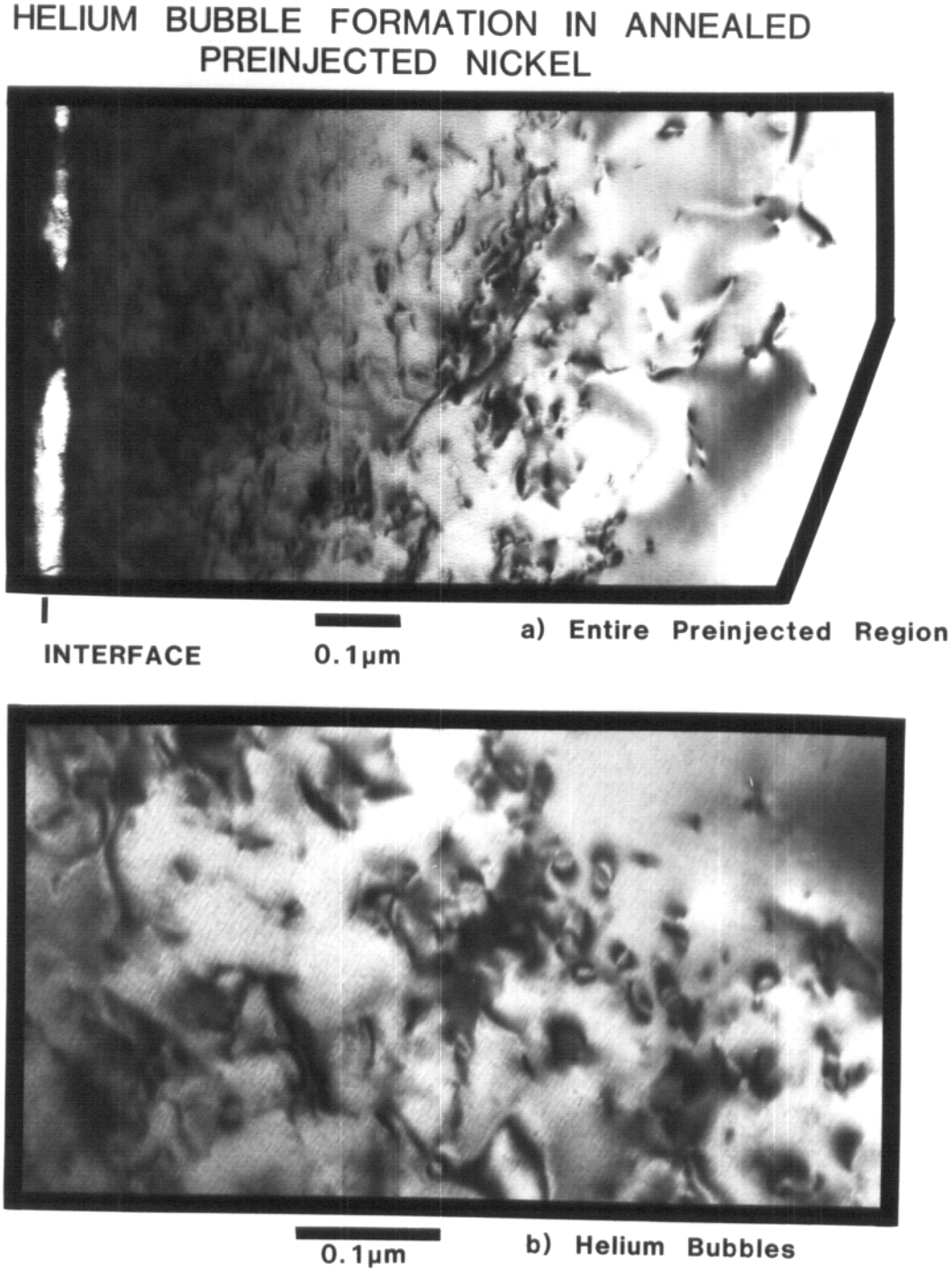

FIG. VI-18. HE BUBBLE FORMATION IN NICKEL PREINJECTED TO A UNIFORM CONCENTRATION OF 10000 APPM AT 25°C AND ANNEALED FOR 1 HOUR AT 525°C.

Samples which were uniformly preinjected with helium and irradiated to 1 x 10^{20} Ni/m^2 formed "apparent" void-free zones over the injected area as seen in Figs. V-29, V-31 and V-33. Each sample contained at least 100 appm helium. This concentration was obviously much too high to allow observable swelling to be produced. The sample in Fig. V-35 was irradiated to a 2.5 x 10^{20} ions/m^2 at 525°C with a preinjected He concentration of 100 appm. Some observable swelling is noted as the mean void size increases with the increased damage. These samples provide good qualitative results. However, to obtain more quantitative results the irradiations should have been completed with lower He preinjection concentrations and higher damage levels.

E.2. Monoenergetic Helium Implantation

The suppression of swelling due to helium implantation at 25°C was caused by a dramatic increase in cavity nucleation as shown in Figs. V-37 through V-44 of the previous chapter. This reduction in swelling with low temperature helium preinjection has been noted previously by Farrell et al.[19] and Packan et al.[28] and others.[33,34] The significance of the present study is the utilization of ions (He and Ni) which have dissimilar ranges in nickel. Previous preinjection and dual ion irradiation studies as outlined in Chapter III, did not utilize the cross-section technique of sample preparation. Application of traditional backthinning techniques required that the incident ions (He and Ni) have similar ranges to allow study of the interactive effects. The cross-section technique

which was employed in this study allows for particles with differing ranges to be used. This allows the separation of the effects of the different beams such as those caused by injected self-interstitials. No previous preinjection study has employed such a technique.

The microstructure of an annealed, monoenergetically preinjected nickel foil is shown in Fig. VI-19. This sample was preinjected with 6500 appm He at 25°C utilizing a 700 keV He^+ beam. The sample was then annealed at 525°C for 50 minutes. An extremely dense dislocation microstructure was evident at the end-of-range of the injected helium. No bubble formation was noted.

This preinjection dislocation microstructure could act as a trapping site for the injected helium. This may result in the enhanced formation of cavities upon ion irradiation. Figure VI-20 shows the region of enhanced cavity formation in a nickel sample preinjected with 650 appm He at 25°C and irradiated with nickel ions to a fluence of 1×10^{21} ions/m^2 at 525°C. Irradiation to this high damage level is required to allow observation of the cavities nucleated with the aid of preinjected helium concentrations of 650 appm or less. This is verified by examination of micrographs shown in Figs. V-38 and V-40. These samples were preinjected with He concentrations of 65 appm and 650 appm, and irradiated to fluences of 2.5×10^{20} and 5×10^{20} ions/m^2, respectively. Each specimen exhibits a region of swelling suppression which results from enhanced nucleation due to the preinjected He. Continued irradiation to higher doses would

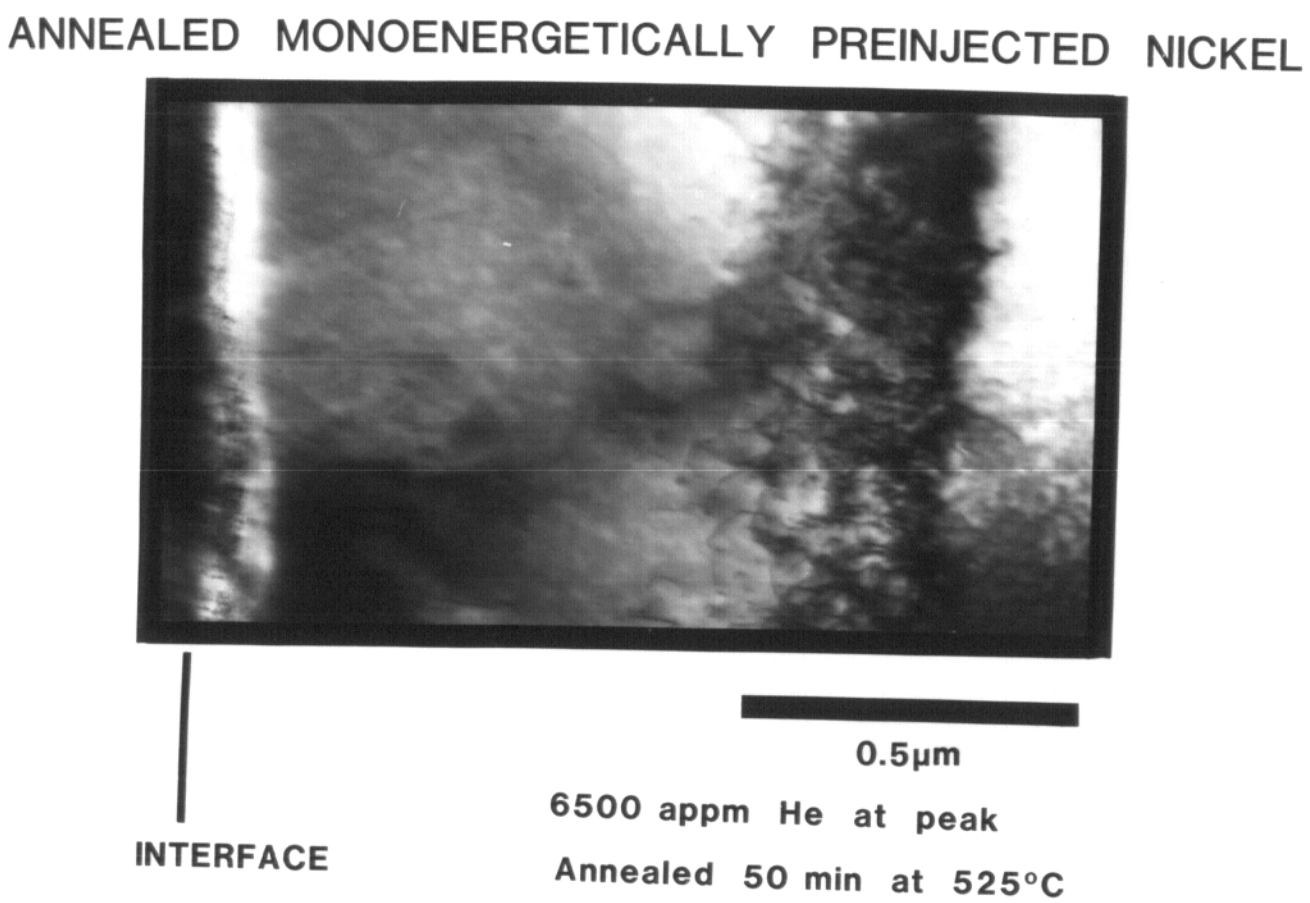

FIG. VI-19. DISLOCATION MICROSTRUCTURE IN NICKEL PREINJECTED WITH A MONO-ENERGETIC (700 KEV) He^+ BEAM TO A CONCENTRATION OF 6500 APPM AND ANNEALED FOR 50 MIN. AT 525°C.

allow the nucleated cavities to grow to a visible size as shown in Fig. VI-20.

Preinjection of 3250 appm He at 25°C followed by nickel ion irradiation to a fluence of 2.5 x 10^{20} ions/m^2 at 525°C results in the formation of observable cavities (Fig. V-43). Since these cavities appear at a relatively low dose and an extremely high injected He concentration, it is likely that a transition from void growth to bubble growth has occurred. At this He concentration, Fenske et al.[32] noted the formation of a very high number density of bubbles in He irradiated nickel at 525°C.

The high cavity number densities in the He preinjected regions of the monoenergetically preinjected samples (7 x 10^{21} to 1.7 x 10^{23} m^{-3}) correspond well with previous He preinjection studies. Brimhall and Simonen[27] reported similar void densities for helium injected nickel. Singh and Foreman reported void densities ranging from 10^{21} to 10^{23} m^{-3} for He concentrations of 1 appm to 1000 appm in various steels. The similarities in cavities number densities suggests similar nucleation rates for given helium concentrations.

F. Comparisons to Other Studies Utilizing Cross-Section Techniques

There have been three previous studies of irradiated nickel which used a cross-section technique similar to that utilized in this study. These studies were completed by Whitley,[14] Fenske et al.[32,36] and Farrell et al.[19] A comparison of experimental parameters is presented in Table VI-1. The results of each study warrant comparison to this study.

ENHANCED CAVITY FORMATION DUE TO HELIUM PREINJECTION

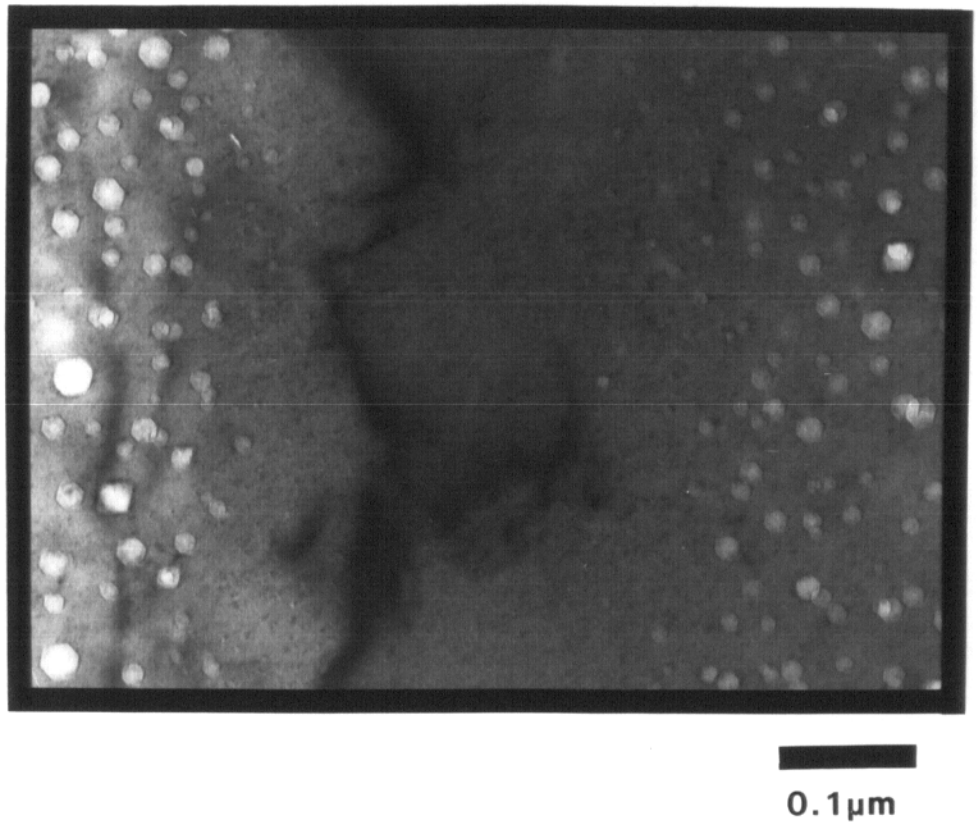

FIG. VI-20. SMALL CAVITY FORMATION IN THE "APPARENTLY" VOID FREE ZONE OF A NICKEL SAMPLE PREINJECTED AT 25°C WITH 650 APPM HE AT A DEPTH OF 1.0 TO 1.25 μM AND IRRADIATED WITH NICKEL IONS TO A FLUENCE OF 1×10^{21} IONS/M^2 AT 525°C.

TABLE VI-1. EXPERIMENTAL PARAMETER COMPARISONS FOR DEPTH DEPENDENT STUDIES IN ION IRRADIATED NICKEL

Parameter	Whitley[14]	Fenske et al.[32]	Farrell et al.[19]	This Study
Material	Marz Ni	Marz Ni	Pure Ni	Marz Ni
Irradiating Ion	Ni, Cu, Al, C	He	Ni	Ni
Ion Energy (MeV)	14, 15, 8, 5	0.02, 0.5	4	14
Irradiation Temp. (°C)	200-625	500	600	525, 625
Implanted Gas	H	He	He	H, He
Implantation Method	Electro-polish	Accelerator	Accelerator	Accelerator
Implantation Energy (MeV)	---	0.02, 0.5	0.2-0.4	0.2-0.7
Implantation Temp. (°C)	25	500	25 - preimplant 600 - co-implant	25
Implanted Gas Concen. (appm)	---	600-30000	20 - preimplant 1000 - co-implant	100-1000 H (1-10 retained) 65-3250 He

The work of Whitley[14] provides the best basis for comparison with respect to heavy-ion irradiation parameters. Whitley used high energy heavy ions (Ni, Cu, Al), all of which have ranges of about 2 μm in nickel. The present study also used 14 MeV Ni ions to produce displacement damage. The method of gas introduction is the primary

difference in these two studies. Whitley introduced hydrogen into the nickel prior to heavy-ion irradiation via a pre-irradiation electropolish. The present study introduced hydrogen utilizing an accelerator implantation at varying energies (200-700 keV) at 25°C. A comparison of the microstructure observed following irradiation with 14 MeV nickel ions at 525°C and 625°C shows a similarity in swelling, void number density and mean void diameter for Whitley's electropolished samples and samples in this study which were implanted with hydrogen to a fluence of 3 x 10^{19} H_3^+/m^2 (1000 appm implanted, 10 appm retained). This suggests that Whitley's samples probably contained between 1 appm and 10 appm H at the onset of the heavy-ion irradiation. A saturation in swelling at about 3% was noted in this study which compares with similar findings by Whitley[14] and Kulcinski et al.[23]

Comparisons to the work of Fenske et al.[32,36] are most applicable to the portion of this study dealing with the microstructure produced during the He preinjections. Fenske studied the formation of helium bubbles in nickel as a function of depth for He ion irradiations at 500°C. Fenske used the cross-section technique to observe He bubble formation due to irradiations with He ions with energies of 20 keV and 500 keV in concentrations ranging from 600-30000 appm. Results reported previously in this chapter for annealed, preinjected nickel compare favorably with the 500 keV irradiations of Fenske. For concentrations of 3000 appm and 15000 appm He, Fenske found He bubbles with a mean diameter of 2.8 and 3.0 nm and number densities

of 7.6 x 10^{22} m^{-3} and 17.5 x 10^{22} m^{-3}, respectively. This study found a mean diameter of 3 nm and a number density of 10 x 10^{22} m^{-3} for a nickel sample preinjected with 10000 appm He and annealed for 1 hour at 525°C, which compares favorably to Fenske's work.

The helium preinjected self-ion irradiated nickel experiments completed in this study are most easily compared to recent work by Farrell et al.[19] Farrell completed self-ion irradiations of nickel with preimplantation and co-implantation of He. Farrell's preimplantations were completed at 25°C to concentrations of 20 appm He, while the co-implantations had concentrations of 1000 appm at the end of the irradiation. A suppression of swelling was noted for the cold preimplanted samples, while an enhancement of swelling was noted for high temperature co-implantations. The results of cold preinjected He noted in Chapters V and VI of this study also showed a reduction in swelling due to enhanced cavity nucleation. This was particularly evident in the sample shown in Figs. V-41 and VI-20. One advantage presented by this work over that of Farrell is the use of beam energies which separate the He preinjected region from the peak damage region. This allows the observation of nucleation enhancement due to He without the competing effect of nucleation suppression due to injected-self interstitials.

G. Extended Range Observations

All of the depth dependent studies[14,19,32,36] noted in the previous section have observed damage microstructure 20 to 40% beyond the calculated end-of-range of the irradiating ion. This phenomena

was also noted in this study as shown in Fig. V-33. This figure shows a curve of the calculated displacement damage as a function of depth plotted below a series of micrographs which extend over the entire range of damage produced by irradiation with 14 MeV Ni ions to a fluence of 1 x 10^{20} ions/m^2 at 525°C. The damage extends to a depth of greater than 3 μm while the predicted damage, calculated using the Brice[37] code, only extends to a depth of 2.5 μm. Similar extended range observations were made for the rest of the samples in this study.

A number of explanations have been made for the observation of damage beyond the calculated end-of-range in ion irradiated nickel. Farrell et al.[19] argue that diffusional spreading is primarily responsible for this observation. Whitley[14] addressed the possibility of diffusional spreading and determined that it could not account for the magnitude of the discrepancy noted (15-20%) in the 14 MeV irradiations. Whitley,[14] Fenske et al.[32] and Bullen et al.[26] have all attributed extended range observations in nickel to inaccuracies in the electronic stopping data used to calculate range profiles. Calculations by Fenske[38] and Attaya[39] have shown that by reducing the electronic stopping one could explain the anamolous ranges. There is nothing in this study to support or refute any of the theories mentioned above. However, this thesis does reinforce the discrepancy.

H. Applicability of Current Theories

The data presented in this report shows that injected hydrogen produces an increase in the swelling rate for a given damage rate. This is due to an increase in the void nucleation rate as shown in Chapter II (Eq. II-24). Recent work by Wolfer[40] shows an enhancement in void nucleation due to chemisorption of surface-active gases, such as H_2. Wolfer[40] calculated a reduction in surface energy of -0.2 J/m^2 in nickel at 500°C with a hydrogen content of 10 appm. This reduction in surface energy reduces the vacancy reemission rate from small void embryos and thereby increases the nucleation rate. The increase in swelling with increasing injected hydrogen content presented in this study is thought to be a direct effect of the reduction in surface energy caused by hydrogen chemisorption.

The variation in swelling rate with damage rate as shown in Figs. VI-13 and VI-14 is due to a decrease in cavity number density at higher damage rates. A comparison between the work of Whitley[14] and this study illustrates this point. Whitley used a damage rate of $1.4\text{-}1.8 \times 10^{-4}$ dpa/sec at a depth of 1 μm while this study employed a damage rate of 1.2×10^{-3} dpa/sec at 1 μm. Figure V-12 shows a peak void number density of about 0.5×10^{21} m^{-3} for nickel preinjected with 100 appm H and irradiated with 14 MeV nickel ions to a fluence of 2.5×10^{20} ions/cm^2 (7 dpa at 1 μm). A comparable irradiation completed by Whitley[14] shows a peak void number density of 4×10^{21} m^{-3} for a fluence of 2×10^{20} ions/m^2 at 525°C. The mean void diameter ranges from 20 to 30 nm for both studies.

The rate effects shown above highlight one problem which the classical theories of cavity nucleation and growth (Chapter II) do not adequately describe. In an irradiation environment, as the number of defects grows, the number of sinks available for point defects also grows causing a reduction in the supersaturation of point defects. Recent calculations by Wehner[41] indicate the existence of a time dependent nucleation barrier. This barrier continues to grow as the sink strength increases eventually becoming impenetrable and causing nucleation to cease. Calculations by Wehner[41] indicate that this termination of nucleation occurs at approximately 0.1 dpa at 500°C in nickel for a damage rate of 10^{-3} dpa/sec. Wehner also notes that higher damage rates yield higher void number densities due to higher vacancy supersaturation.

The effect of injected self-interstitials at low temperatures (400-450°C) on void nucleation correlates well with the current model proposed by Plumton[25] (as shown in Fig. VI-15). The suppression in void nucleation at the peak of the injected self-interstitial as shown in Figs. V-1, V-3 and V-5, correlates well with this model. The irradiations at higher temperatures (525°C and 625°C) further support this model by indicating little or no injected interstitial effect on void nucleation.

I. Implications of This Study

The results and discussion presented in this chapter and the previous chapter have a number of important implications with respect to the applications of materials to a fusion reactor environment.

This section will briefly review the significant aspects of this study which will possibly have direct impact on fusion materials selection.

The effect of injected hydrogen on cavity nucleation and subsequent swelling in nickel has wide ranging ramifications in current and future fusion devices. Preliminary testing of all fusion devices will include the formation of a hydrogen (H_2) plasma to verify machine operating characteristics and to provide plasma discharge cleaning of the reactor vacuum chamber. This hydrogen plasma will promote diffusion and permeation of hydrogen atoms into the first wall of the reactor introducing nucleation sites for cavities which are directly analogous to the preinjections done in this study. The results of this study suggest further studies of hydrogen effects on all candidate first wall materials should be completed.

A further ramification of the hydrogen study is the observation of rate effects in self-ion irradiated nickel samples which were evaluated in regions away from the injected self-interstitial peak in the linear (non-saturated) swelling regime. These results and associated comparisons to previous self-ion irradiations indicated a definite hydrogen effect on swelling rate and an observable damage rate effect on swelling rate below 10^{-3} dpa/sec. This study also identified no clearly observed injected self-interstitial effect of damage rates above 10^{-3} dpa/sec at 525°C. These rate effects may be important in limiters, divertor and neutral beam dump surfaces. The displacement rates could be quite high (e.g., 10^{-3} dpa/sec for 10^{14}

D/T ions per cm^2-sec). Since the rate at which cavities form is so rate-dependent, variations in charge exchange or particle fluxes could produce differing results in the same reactor component surface.

The injected helium studies also have possible direct application in fusion materials research. Areas of a fusion reactor which see high helium fluences with associated neutron damage, such as the near surface of a first wall or the limiter of a tokamak, may experience cavity nucleation and growth similar to that shown in this study for helium injected, self-ion irradiated nickel. The copious cavity formation found in this study suggest that further research on materials which will experience a high helium fluence as well as neutron displacement damage is warranted to better understand the possible material response to such an environment.

Finally, the injected interstitial effects noted at low temperatures and the extended range observations made in this study raise questions about the valid conditions under which heavy-ion irradiations should be conducted. This data may also aid in the development of theoretical models which more accurately describe the microstructural evolution in a heavy-ion irradiation environment. Such calculations may then aid in the correlation of heavy-ion and neutron irradiation data.

References for Chapter VI

1. R.M. Latanision and H. Opperhauser, Jr., Hydrogen in Metals, American Society for Metals, (1974) p. 539-544.

2. G.C. Smith, Hydrogen in Metals, American Society for Metals, (1974) p. 485-511.

3. W.D. Wilson, CONF-751006-P2, Gatlinburg, TN, Oct. 6-10, 1975.

4. G.J. Thomas, Sandia National Laboratory Report, SAND 80-8656, Oct. 1980.

5. D.K. Brice and B.L. Doyle, to be published in J. Nucl. Matl.

6. B.L. Doyle and D.K. Brice, Third Topical Meeting on Fusion Reactor Materials, Sept. 19-22, 1983, Albuquerque, NM, to be published in J. Nucl. Matl.

7. D.K. Brice, Third Topical Meeting on Fusion Reactor Materials, Albuquerque, NM, Sept. 19-22, 1983, to be published in J. Nucl. Matl.

8. K.L. Wilson and A.E. Pontau, J. Nucl. Matl. 85&86 (1979) 989-993.

9. K.L. Wilson, A.E. Pontau, L.G. Haggmark, M.I. Baskes, J. Bohdansky and J. Roth, J. Nucl. Matl. 103&1-4 (1981) 493-498.

10. K.L. Wilson and M.I. Baskes, J. Nucl. Matl. 111&112 (1982) 622-627.

11. T. Tanabe, N. Saito, Y. Etoh and S. Imoto, J. Nucl. Matl. 103&104 (1981) 483-488.

12. T. Tanabe, Y. Furuyama and S. Imoto, Third Topical Meeting on Fusion Reactor Materials, Albuquerque, NM, Sept. 19-22, 1983, to be published in J. Nucl. Matl.

13. B.L. Doyle, J. Nucl. Matl. 111&112 (1982) 628-635.

14. J.B. Whitley, Ph.D. Thesis, University of Wisconsin, Madison, Wisconsin, 1978.

15. W.G. Johnston, J.H. Rosolowski and A.M. Turkalo, J. Nucl. Matl. 62 (1976) 167.

16. W.G. Johnston, W.G. Morris and A.M. TUrkalo, Radiation Effects in Breeder Reactor Structural Materials, M.L. Bleiberg and J.W. Bennett (eds.) (The Metallurgical Society of AIME, 1977), p. 421.

17. F.A. Garner and G.L. Guthrie, in: Proc. Int. Conf. on Radiation Effects on Tritium-Technology, CONF-750989 (March 1976), p. I-491.

18. F.A. Garner, J. Nucl. Matl. 117 (1983) 177-197.

19. K. Farrell, N.H. Packan and J.T. Houston, Rad. Effects 62 (1982) 39-52.

20. T.D. Ryan, Ph.D. Thesis, University of Michigan, 1975.

21. J.E. Westmoreland, J.A. Sprague, F.A. Smidt, and P.R. Malmberg, Rad. Effects 26 (1975) 1-16.

22. J.L. Brimhall, L.A. Charlot and E.P. Simonen, J. Nucl. Matl. 103&104 (1981) 1147-1150.

23. G.L. Kulcinski, J.L. Brimhall and H. Kissinger, Int. Conf. on Radiation Induced Voids in Metals, ed. Corbett and Ianniello, Albany, NY, 1971, CONF-710601, p. 449, (1972).

24. K.B. Roarty, J.A. Sprague, R.A. Johnson and F.A. Smidt, Jr., J. Nucl. Matl. 97 (1981) 67-78.

25. D.L. Plumton, to be published.

26. D.B. Bullen, G.L. Kulcinski and R.A. Dodd, Third Topical Meeting on Fusion Reactor Materials, Albuquerque, NM, Sept. 19-22, 1983, to be published in J. Nucl. Matl.

27. J.L. Brimhall and E.P. Simonen, J. Nucl. Matl. 68 (1977) 235.

28. N.H. Packan, K. Farrell and J.O. Stiegler, J. Nucl. Matl. 78 (1978) 143-155.

29. H. Van Swygenhoven and L.M. Stals, Rad. Effects 78 (1983) 157-163.

30. H. Van Swygenhoven, G. Knuyt, J. Vanoppen and L.M. Stals, J. Nucl. Matl. 114 (1983) 157-167.

31. W. Jager, R. Manzke, H. Trinhaus, G. Crecelius, R. Zeller, J. Fink and H.L. Bay, J. Nucl. Matl. 111&112 (1982) 674-680.

32. G. Fenske, S.K. Das, M. Kaminsky and G.H. Miley, J. Nucl. Matl. 85&86 (1979) 707-711.

33. F. Menzinger and F. Sacchetti, J. Nucl. Matl. 57 (1975) 193-197.

34. W.G. Johnston, J.H. Rosolowski and A.M. Turkalo, J. Nucl. Matl. 54 (1974) 24-40.

35. B.N. Singh and A.J.E. Foreman, J. Nucl. Matl. 103&104 (1981) 1469-1474.

36. G. Fenske, S.K. Das and M. Kaminsky, J. Nucl. Matl. 103&104 (1981) 1231-1236.

37. D.K. Brice, SAND-7500622, Sandia Laboratories, Albuquerque, NM, July 1977.

38. G. Fenske, S.K. Das, M. Kaminsky, G. Miley, B. Terreault, G. Able, J.P. Labrie, J. Appl. Phys. 52 (1981) 3618.

39. H. Attaya, Ph.D. Thesis, University of Wisconsin, Madison, Wisconsin, May 1981.

40. W.G. Wolfer, presented at the Third Topical Meeting on Fusion Reactor materials, Albuquerque, NM, Sept. 19-23, 1983, to be published in J. Nucl. Matl.

41. M.F. Wehner, private communication.

CHAPTER VII

CONCLUSIONS

The 700 kV Accelerator Facility at the University of Wisconsin was designed, constructed, tested and utilized to preinject samples of pure nickel with various concentrations of hydrogen or helium prior to irradiation with nickel ions at fluences ranging from 1 x 10^{20} to 1 x 10^{21} ions/m^2 and temperatures of 525°C and 625°C. Self-ion irradiations of nickel were also completed at temperatures of 450°C, 425°C and 400°C to study the effect of injected self-interstitials on cavity nucleation. A cross-section technique of sample analysis was used to evaluate the irradiated samples. This method allowed the observation of dose, dose rate and gas effects since all were depth dependent (except for the case of hydrogen gas as noted below). Preinjected nickel samples were also studied to determine the microstructure produced by the introduction of H or He at 25°C and following 1 hour post-preinjection anneals at 525°C.

Specific observations noted in this study are:

1. Preinjected hydrogen was found to increase cavity nucleation throughout the entire damage region produced by the self-ion irradiation. The fact that the effect was spread throughout the Ni ion damage zone could result from the high mobility of the hydrogen which becomes detrapped during high temperature irradiation.

2. Preinjected hydrogen which diffused throughout the entire foil was trapped at grain boundaries and produced brittle fractures in some samples during post-irradiation sample preparation.
3. Preinjection of even the smallest amount of hydrogen (3×10^{18} H_3^+/m^2, 100 appm injected, estimated 1 appm retained) produced a decrease in the mean void diameter and an increase in the observed void number density and swelling at 525°C.
4. Further increases in preinjected hydrogen fluence to 1.5×10^{19} and 3×10^{19} H_3^+/m^2 (500 appm injected, estimated 5 appm retained and 1000 appm injected, estimated 10 appm retained) produced increases in swelling primarily due to increases in void number density.
5. Effects of hydrogen preinjection in self-ion irradiated nickel at 625°C were not noted until a fluence of 3×10^{19} H_3^+/m^2 (1000 appm injected, estimated 10 appm retained) was reached. This is possibly due to hydrogen escape while the sample is heated to the irradiation temperature prior to irradiation.
6. A comparison of self-ion irradiation data for non-saturated swelling from this and other studies, suggests no clear evidence of injected interstitial effects on swelling rate (% per dpa) above a dose rate of 10^{-3} dpa/sec and a temperature of 525°C.
7. A dramatic increase in the swelling was noted for increasing preinjected hydrogen fluence at 10^{-3} dpa/sec. This demonstrates that hydrogen is an important nucleating agent that must be

considered when comparing heavy-ion and neutron irradiation data.

8. A suppression of swelling was noted throughout the entire helium preimplanted region (front surface to 1.25 μm). Subsequent irradiation of these samples with nickel ions to fluences of 1-2.5 x 10^{20} ions/m^2 at 525°C and 625°C revealed a suppression in swelling which was attributed to enhanced nucleation of small cavities.
9. Preinjection with monoenergetic helium produced bands of swelling suppression due to enhanced nucleation of very small cavities. The existence of these cavities proposed in the uniform helium preinjection experiments was verified by heavy-ion irradiation of the preinjected samples to high doses (up to 1 x 10^{21} ions/m^2).
10. Preinjection of nickel with 3 x 10^{19} H_3^+/m^2 (1000 appm, estimated 10 appm retained) at 25°C produced no observable microstructural changes which would indicate trap site formation.
11. Preinjection of nickel with 1000 appm He at 25°C produced dislocation loops with a density of 2 x 10^{20} m^{-3} and an average diameter of 7.5 nm. Post-preinjection annealing at 525°C for 1 hour produced little appreciable change in this microstructure. This is a further indication of the limited mobility of the preinjected helium in nickel at the irradiation temperature.

12. No helium bubble formation in nickel was noted until injected concentrations reach 10000 appm and the sample was annealed at 525°C for 1 hour.
13. Suppression of void nucleation was noted at the peak damage region for nickel irradiated at 450°C. An increase in the width of the suppressed region was noted for samples irradiated at 425°C and 400°C in accordance with current theories on injected interstitial suppression of void nucleation at low temperatures.
14. A saturation of swelling with displacement damage was noted in all nickel samples irradiated above 10 dpa. This saturation occurred at a value of about 3% and corresponded with swelling saturations noted in other heavy-ion irradiations.
15. Displacement damage was noted up to 40% beyond the end-of-range of the irradiating ion. This discrepancy in calculated and observed damage could be due to inaccuracies in stopping power values used in the Brice calculations.

CHAPTER VIII

SUGGESTIONS FOR FUTURE WORK

The results presented in this report suggest a number of possibilities for future work. These include:

1. Self-ion irradiations at lower damage rates to confirm the swelling rate increase with decreasing damage rate as shown in Fig. VI-14.
2. Irradiation of hydrogen preinjected samples to lower damage levels (< 5 dpa) to obtain swelling in the linear regime which would facilitate more quantitative evaluation of hydrogen effects on swelling rate.
3. Irradiation of samples preinjected with higher concentrations of hydrogen to determine if the saturation in swelling with increasing hydrogen content is actually observed.
4. Irradiations of helium preinjected samples with helium concentrations in the range 0.1 to 100 appm to allow more accurate study of the effect of helium of void nucleation.
5. Co-implantation studies in self-ion irradiated nickel utilizing either H or He co-implantation.
6. Continued study of extended range effects to more accurately describe the magnitude of the discrepancy between calculated and observed damage profiles.